

NORTHWESTERN UNIVERSITY

Nanostructuring Plasmonic Materials to Engineer Optical Responses

A DISSERTATION

SUBMITTED TO THE GRADUATE SCHOOL
IN PARTIAL FULFILLMENT OF THE REQUIREMENTS

for the degree

DOCTOR OF PHILOSOPHY

Field of Materials Science and Engineering

By

Michael P. Knudson

EVANSTON, ILLINOIS

March 2018

© Copyright by Michael P. Knudson 2018

All Rights Reserved

ABSTRACT

Nanostructuring Plasmonic Materials to Engineer Optical Responses

Michael P. Knudson

Plasmonic nanostructures are capable of trapping and confining light at the nanoscale, leading to interesting optical phenomena involving enhanced light-matter interactions. These responses arise in two forms: surface plasmon polaritons propagating on the surface of metal films and localized surface plasmons confined to the surface of metal nanoparticles. Plasmonic modes can couple to free space light with a wavelength dependent on the size and shape of the nanostructuring, the metal material properties, and the surrounding dielectric environment. The properties and applications of these optical responses are discussed in Chapter 1, providing an introduction for plasmonics. In the remainder of this thesis I explore methods to tailor the plasmonic responses by controlling the nanostructuring of plasmonic devices.

I explore this topic from the fabrication perspective in Chapter 2. I discuss and demonstrate a complete fabrication process using parallel patterning techniques for sequential feature density doubling of periodic silicon gratings. These silicon substrates were used for template stripping to produce plasmonic films with nanostructuring to support surface plasmon polaritons. The optical responses were characterized to illustrate their ultraviolet plasmonic activity and to examine the importance of developing scalable patterning methods that access shorter periodicities for manipulating surface plasmon polariton wavelengths across the UV spectrum.

Chapter 3 and 4 describe progress toward tailoring optical cavities for enhancing the photoluminescence intensity of single-walled carbon nanotubes and few-layer black phosphorus, respectively. Both of these nanomaterials possess unique optical properties that show promise for applications in optoelectronics and telecommunications technology but suffer from weak fluorescence efficiency. Lattice plasmon modes were tested as optical cavities for enhancing the emission rate of these two nanomaterials. The lattice plasmon modes were engineered by controlling the geometry of nanoparticle arrays through fabrication methods and by selecting optimal materials for the substrates and superstrates.

Chapter 5 investigates low-symmetry nanoparticle arrays as a way to examine the effects of geometry in photonic lasers. I developed a new, scalable fabrication procedure capable of patterning nanoparticle arrays composed of rhombus-shaped nanoparticles arranged in rhombohedral lattices. This low-symmetry platform provided insight regarding how nanoparticle shape can be used to engineer the electromagnetic hot spots of lattice plasmon modes. Examination of lasing behavior revealed that plasmon-exciton energy transfer is polarization dependent, with stronger coupling and faster dynamics observed when the dipolar orientations of plasmonic modes and gain materials are aligned. As a result, two lattice plasmon modes localized to the same nanoscale hot spots were shown to support lasing simultaneously by coupling to different polarizations of excited dye populations.

Acknowledgements

I would first like to express my gratitude toward Professor Teri W. Odom for advising me throughout my time at Northwestern. She has helped me to identify interesting and challenging problem and helped me develop the scientific and technical expertise to pursue the answers. I also want to thank the department administrators, especially Lindsay Haukebo and Jeannine Hall, who have provided endless support and assistance throughout my graduate career. I would also like to acknowledge my thesis committee members Professor Mark Hersam, Professor Lincoln Lauhon, and Professor George Schatz for dedicating their time to reviewing my thesis and defense.

I would like to acknowledge my collaborators Yujin Shin, Alexander Hryn, Ankun Yang, Weijia Wang, Danqing Wang, Jingtian Hu, Ran Li, Joohoon Kang, Mark Huntington, and Professor Richard Schaller on various projects for their hard work and contributions. Some of these colleagues worked with me within the Materials Research Science and Engineering Center, which provided support and fostered our interdisciplinary collaboration. I would also like to thank the many research facilities at Northwestern, including NUFAB, NUACE, EPiC, Keck-Biophysics, and Keck-II that fortuitously come together to enable top-class research. The facility managers have been invaluable resources throughout my time at Northwestern, offering scientific advice and technical expertise.

My friends in the Materials Science Department, accross Northwestern, and beyond the university have been an reliable source of support throughout grad school. In addition to my collaborators, my friends Kayla Culver, Do Soon Kim, Kavita Chandra, Linda Guiney, Jade Balla, Emma Coughlin, Tad Reese, Yi Hua, Will Dearden, Johan Konter, and Nour Alharithi, Paula Acuña, Jason Riddell, Nikhil Byanna, Thomas Butler, and Reed Klaeser remind me to laugh and smile regularly. I especially want to thank Nicholas Adams for his companionship and his ability to always make my days brighter.

Lastly, and most importantly, I want to thank my family for their love and support throughout the past 29 years and on into the future. They taught me to be optimistic about life while staying grounded in my work. My family has always believed in my abilities and constantly pushed me to improve. While not scientists by training, my parents emphasized the importance of a scientific education and demonstrated the value of scientific curiosity. My sisters Karla Knudson, Ph.D., and Christina Knudson, Ph.D., have become my academic mentors and role models, coaching me through the many challenges of higher education in STEM. Finally, my brother Jonathan has been my best friend throughout our lives, and his unwavering encouragement has been invaluable.

List of abbreviations

AFM	atomic force microscopy
Al	aluminum
ALD	atomic layer deposition
Au	gold
BP	black phosphorus
CCD	charge coupled device
Cr	chromium
DMSO	dimethyl sulfoxide
DRIE	deep reactive ion etching
FDTD	finite-difference time-domain
FWHM	full width at half maximum
LDOS	local density of optical states
LSP	localized surface plasmon
PL	photoluminescence
PMMA	polymethyl methacrylate
NIR	near-infrared
NP	nanoparticle
PDMS	polydimethyl siloxane
PSP	Phase-shifting photolithography
PEEL	photolithography, etching, e-beam deposition, and lift-off
SANE	solvent-assisted nanoscale embossing
SEM	scanning electron microscopy

SPP surface plasmon polariton

SWNT single walled (carbon) nanotube

Si silicon

TCSPC time-correlated single-photon counting spectroscopy

TE transverse electric

TM transverse magnetic

UV ultraviolet

Table of Contents

ABSTRACT	3
Acknowledgements	5
List of abbreviations	7
Table of Contents	9
List of Tables	12
List of Figures	13
Chapter 1. Introduction to Plasmonics	23
1.1. Surface Plasmons in Metal Nanostructures	24
1.2. Nanopatterning of Plasmonic Materials	26
1.3. Plasmonic Cavities for Enhancing Fluorescence	29
1.4. Applications of Plasmonics for Lasing	31
1.5. Nanowire-on-film Lasers	32
1.6. Nanoparticle Array Lasers	36
Chapter 2. Sequential Feature-Density Doubling for Ultraviolet Plasmonics	41
2.1. Introduction for Patterning Tools	42
2.2. Fabrication of Si Lines Through Sequential Feature Density Doubling	43
2.3. Transfer of Patterns into Plasmonic Materials	49
2.4. Optical Properties of Al Gratings	50
2.5. Summary	52

	10
2.6. Methods	55
Chapter 3. Plasmonic Enhancement of Carbon Nanotube Photoluminescence	57
3.1. Introduction to Lattice Plasmon Modes	58
3.2. Carbon Nanotube Optical Properties	58
3.3. Designing Optical Cavities to Target Nanotubes.	61
3.4. Fabrication and Testing of Plasmonic Arrays	65
3.5. Summary	69
3.6. Methods	69
Chapter 4. Amplified Light-Matter Interactions in Phosphorene	72
4.1. Introduction to Two-Dimensional Semiconductor Nanomaterials	73
4.2. Targeting Phosphorene Emission with Lattice Plasmons	74
4.3. Near-field Properties of Lattice Modes	76
4.4. Integrating Nanoparticle Arrays with Phosphorene	76
4.5. Materials Selection for Improving Lattice Mode Overlap and Quality	80
4.6. Summary	82
4.7. Methods	82
Chapter 5. Polarization Dependent Lasing Behavior in Low-Symmetry Nanocavity Arrays	84
5.1. Introduction to Symmetry Effects in Photonic Systems	85
5.2. Fabrication of Low-Symmetry Nanoparticle Arrays	86
5.3. Nanoparticle Shape Effects in Lattice Plasmon Systems	90
5.4. Lasing Properties of Co-localized Cavity Modes	91
5.5. Influence of Pump Polarization on Lasing Dynamics	95
5.6. Summary	98
5.7. Methods	99
Chapter 6. Conclusion and Outlook	103

	11
References	106
Appendix A. Near-field Mapping	118
Appendix B. Vita	127

List of Tables

- 5.1 Bragg modes for rhombohedral lattices. Bragg mode wave vectors are given for several diffraction modes using arbitrary lattice angle ψ and periodicity a to calculate the Bragg mode wavelength at normal incident angle. Degenerate modes are shown in the same color, with first-order modes in blue and second-order modes in green or red.

List of Figures

- 1.1 Classes of Surface Plasmons. (a) Surface plasmon polaritons propagate on the surface of continuous metal films. (b) Localized surface plasmons are confined to metal nanoparticles. Figure adapted from Henzie et al.¹ 25
- 1.2 Phase-shifting Photolithography. (a) A monolithic silicon master patterned with posts arrays is fabricated using interference lithography and used to mold a PDMS mask. (b) Phase-shifting photolithography is performed to create resist posts that are then transferred into Au masks. (c) Soft lithography is used to pattern gold hole arrays over cm-scale areas. Figure adapted from Henzie et al.¹ 27
- 1.3 Nanopatterning with SANE. (a) A PDMS stamp is molded from a master template. The stamp is loaded with solvent by soaking and then used for embossing polymer resist. (b) An SEM image of sample photoresist post arrays patterned by SANE. Figure adapted from Lee et al.² 28
- 1.4 Nanowire-on-film spaser designs. (a,b) Spaser designs based upon semiconductor nanowires on plasmonic metal films may incorporate different materials depending upon laser wavelength. (c,d) Nanowire geometry influences surface plasmon polariton hybridization with waveguide modes within insulator gaps. Panels a and c adapted from Oulton et al.³ Panels b and d adapted from Zhang et al.⁴ 33
- 1.5 Multimodal lasing from nanowire-on-film devices. (a) Emission spectra for increasing pump intensities show progression from spontaneous emission (blue), amplified spontaneous emission (red), and multimodal lasing (green and yellow). (b) Plot of

- mode spacing versus inverse nanowire length $1/L$ shows a linear relationship. Figure adapted from Oulton et al.³ 34
- 1.6 Lasing-based sensors for explosives. (a) Scheme for DNT sensing based on a nanowire-on-film laser. (b) Laser intensity shows ppb sensitivity to DNT in the surrounding environment while laser wavelength remains unchanged. Figure adapted from Ma et al.⁵ 36
- 1.7 Lattice plasmons with sharp resonances in periodic metal nanoparticle arrays. (a) Experimental demonstration of sharp lattice plasmon resonances from gold nanorod arrays. (b) Simulated extinction spectra of an 1D chain of silver nanoparticles with varying spacings by coupled dipole method. Inset shows the real and imaginary parts of the normalized dipole sum. Panel a adapted from Auguie et al.⁶ Panel b adapted from Zou et al.⁷ 37
- 1.8 Directional lasing from NP arrays. (a) Scheme of a laser device including gold NP arrays embedded in liquid or solid-state gain media. (b) Calculated optical band structure. (c) Simulated phase profile at lattice plasmon resonances. (d-e) Power dependent lasing emission and input-power output-intensity curves. (f) Far-field beam profile with a highly directional lasing spot. Panel a adapted from Wang et al.⁸ Panel b adapted from Wang et al.⁹ Panels c-e adapted from Zhou et al.¹⁰ Panel f adapted from Yang et al.¹¹ 38
- 1.9 Real-time tunable nanolasing from plasmonic nanoparticle arrays by refreshing liquid dye solutions. (a) Scheme of a lasing device consisting of gold NP arrays sandwiched between liquid dye solutions and a glass coverslip. (b) Statically tuned lasing wavelengths can span the entire emission bandwidth of the dye. (c) Scheme of the dynamic laser with a microfluidic channel. (d) Continuous shifting of lasing emission to longer wavelengths and then back to shorter wavelengths. Figure adapted from Yang et al.¹¹ 39

- 1.10 Multi-modal nanolasing in gold nanoparticle superlattices surrounded by liquid dye solutions. (a) SEM image of gold superlattice arrays with NP spacing $a_0 = 600$ nm, patch side length $l = 18$ nm and patch periodicity $A_0 = 24$ nm. (b) lasing emission profile (in black), dye emission profile (in orange) and linear optical properties (in blue). (c) Measured optical band structure of superlattice arrays. (d) Angle-resolved emission spectra of multi-modal lasing. (e) Switchable lasing between single and multiple lasing peaks from symmetry-broken NP line patches. Figure adapted from Wang et al.⁹ 40
- 2.1 Tunable linewidths. (a) Controlled wet over-etching of ALD-alumina lines for use as DRIE masks. (b)–(i) SEM images of Si lines after DRIE showing decreasing Si linewidths for increasing wet over-etching times. 44
- 2.2 Atomic force microscopy (AFM) data for Si lines. Image and cross section for $t = 130$ s of alumina wet over-etching. Using a DRIE time of 30 s, Si etch depth is 70 nm for these samples. Features appear wider than corresponding SEM image due to AFM tip effects. 45
- 2.3 Trend in linewidths for wet over-etching times. The plot shows a linear trend with a slope of -1 nm/s and a root mean square error of 4 nm. 45
- 2.4 Image processing and edge fitting for computing roughness. (a) SEM image of a Si line pattern with $a'' = 100$ nm periodicity before (left) and after (right) converting to binary black and white coloration. The image includes eight edges, each 2.2 microns long. (b) The black and white regions are used to define a set of points along the line edges with pixel connectivity 8. (c) Each edge is individually fit to a least-squares line, and the mean square error of each linear fit is converted from units of pixels to nm. The mean square error is averaged for eight edges to determine the mean square error line edge roughness in nm for each sample. 46

- 2.5 Trend in roughness with etch time. Each data point represents the average line edge roughness for the corresponding image in **Figure 2.1** using 8 edges per sample, each 2.2 microns long. Line edge roughness is ~ 3 nm for short etch times and increases slightly as wet etch time increases. The linear fit has a slope of 0.01 nm/s and a root mean square error of 0.3 nm. 46
- 2.6 Feature density doubling process. A parent Si pattern with line periodicity $a = 400$ nm was used to generate a daughter Si pattern with periodicity $a' = 200$ nm. A second doubling sequence produced a granddaughter pattern with periodicity $a'' = 100$ nm. 47
- 2.7 Two sequences of feature density doubling. SEM images of periodic Si lines. (a) Generation 1: $a = 400$ nm with a photograph inset to show total patterned area >3 cm². (b) Generation 2: $a' = 200$ nm. (c) Generation 3: $a'' = 100$ nm. 48
- 2.8 Cross sections of etched Si lines. SEM cross sections show Si line patterns with periodicities $a = 400$ nm (a), $a' = 200$ nm (b), and $a'' = 100$ nm (c). Etch depths for these patterns are 70 nm, 50 nm, and 35 nm, respectively, using the same DRIE process for each sample. Differences in etch depth are attributed to aspect ratio dependent etching, a well-known phenomenon in which narrower features are etched to shorter depths in DRIE. 49
- 2.9 SEM cross sections showing etching profiles. Alternating lines of evaporated Cr (wide) and ALD alumina (narrow) were used for masking Si during DRIE etching. The different widths allowed identification of mask materials. Cr masks produced slightly slanted sidewalls ($\sim 84^\circ$) during DRIE processing, while ALD alumina masks produced vertical sidewalls ($\sim 89^\circ$). All sidewalls, however, were sufficiently vertical for the feature-doubling process. Si lines were etched to a depth of 90 nm with evaporated Cr and ALD alumina masks, 7-nm and 5-nm thick, respectively, showing potential for high etch depths with these thin film materials. 50

- 2.10 Template-stripped Al line patterns. (a) Template stripping scheme. (b–d) SEM images of Al line gratings with $a = 400$ nm, $a' = 200$ nm, and $a'' = 100$ nm. Photograph inset shows a patterned area >3 cm² that is identical to the template in **Figure 2.10a**. 51
- 2.11 AFM data for AL lines. Images and cross sections for Al line arrays with periodicities (a) $a = 400$ nm, (b), $a' = 200$ nm, and (c) $a'' = 100$ nm. Heights are 65 nm, 45 nm, and 5 nm, respectively, which are consistent with Si line depths within 5 nm aside from the $a'' = 100$ nm sample. The sharp minima in the $a'' = 100$ nm cross section, however, suggest the AFM tip was too wide to reach the bottom of the trenches between lines. AFM tip effects prevented measuring the full depth, and so the true feature height was likely larger than 5 nm. 52
- 2.12 Plasmonic modes of Al line patterns. Reflectance spectra for periodicities of $a = 400$ nm (a), $a' = 200$ nm (b), and $a'' = 100$ nm (c). Spectra were collected from 5° to 55° in increments of 5° . Devices showed UV and visible modes with dispersive character based on incident angle. 53
- 2.13 Dispersion diagrams for reflectance of Al devices. Spectra for $a = 400$ nm periodicity Al lines from (a) experimental measurement and (b) simulation. Spectra for $a' = 200$ nm periodicity Al lines from (c) measurement and (d) simulation. Spectra for $a'' = 100$ nm periodicity Al lines from (e) measurement and (f) simulation. The lines in the plot show analytical calculations of first order ($i = 1$) SPP modes in blue and second order ($i = 2$) SPP modes in green for the respective structures. Simulations were performed using finite-difference time-domain (FDTD) simulations in Lumerical with a plane wave light source and periodic boundary conditions using a broadband fixed-angle source technique (BFAST). 54
- 3.1 Structure of Carbon Nanotubes. (a) A schematic diagram showing how nanotubes can be visualized as sheets of graphene rolled along different directions. Different classes

of nanotube chiralities are shown, including zig-zag (b), chiral (c), and armchair (d).

Figure adapted from Zhang et al.¹²

59

- 3.2 The density of states in a semiconducting SWNT shows van Hove singularities forming peaks in the valence and conduction bands at positions dependent on chirality. Photon absorption (green arrow) is followed by non-radiative decay within the valence band and within the conduction band (dashed arrows) to the band edges from which emission (red arrow) may occur. Reproduced from Bachilo et al.¹³ 60
- 3.3 Photoluminescence map for carbon nanotubes. Unsorted solutions of carbon nanotubes showed several bright spots in their PL map corresponding to different chiralities of nanotubes. The brightest spot is attributed to (6, 5) chirality that emit near 995 nm with excited at 570 nm. 62
- 3.4 Tuning and optimization of lattice modes. (a) Scheme showing a Au nanodisks array on a glass substrate and embedded within a thin film of carbon nanotubes and gelatin. (b) Simulated transmission spectra for varying nanoparticle diameters to optimize the quality factor and peak intensity for the lattice mode near 1000 nm. 63
- 3.5 Lattice mode near-field properties. Mappings of electromagnetic field intensity (a), phase (b), and charge density distribution (c) for a lattice mode at 1003 nm. The light was incident at normal angle and polarized along the x -axis of the nanoparticle arrays. Nanoparticles are shown in white dotted line outlines. 64
- 3.6 Fabrication of Au nanoparticle arrays. (a) A scheme showing the fabrication process for producing nanoparticle arrays on glass. (b) An SEM image showing the fabricated arrays of Au nanodisks with $a = 650$ nm periodicity and $d = 140$ nm diameter. 65
- 3.7 Optical properties of nanotubes with nanoparticle array. (a) The measured transmission spectrum for a Au NP array is shown with the emission spectrum for (6, 5) sorted carbon nanotubes. The lattice mode and emission peak show spectral

- overlap near 1000 nm. (b) PL spectra for a nanotube film comparing areas on the Au NP array against areas off the array show PL enhancement by a factor of two. 66
- 3.8 Lifetime measurements of nanotube emission. (a) A scheme for lifetime measurements using a streak camera to perform time-correlated single-photon counting spectroscopy. (b) Emission decay plots for nanotube films on nanoparticle arrays on and off nanoparticle arrays. 68
- 4.1 Phosphorene chemical structure. A schematic diagram of the chemical structure of phosphorene showing a layered composed of two dimensional sheets of phosphorus atoms with strong in-plane bonding. The layers have a corrugated structure that creates anisotropic properties. Figure adapted from Bagheri et al.¹⁴ 73
- 4.2 Nanoparticle arrays for phosphorene enhancement. (a) SEM images depicting Au nanoparticle arrays on a quartz substrate. (b) Measured (red) and simulated (blue) spectra for normal angle transmission with a PMMA index-matching layer. (c) A dispersion diagram showing the optical band structure of the nanoparticle arrays under TM polarization with Bragg modes traced in dotted lines. 75
- 4.3 Simulated near-field mappings for Au NP arrays. Plots of electric field intensity (a), phase (b), and charge density distribution (c) for a lattice plasmon mode at 932 nm. The simulation uses light injected at normal angle (z -direction) with polarization along the x -axis. Dotted white lines outline the Au nanoparticle positions. 77
- 4.4 Transfer of phosphorene. Exfoliated few-layer phosphorene was filtered using an amorphous aluminum oxide membrane. The dried film was stamped with PDMS to pick up patches of phosphorene film that are transferred to the Au nanoparticle arrays on a glass or MgF_2 substrate. Index-matching was performed by spin-coating PMMA. Image courtesy of Dr. Yu Jin Shin. 78
- 4.5 Optical properties of few-layer phosphorene. (a) and (b) PL spectra for representative flakes of few-layer phosphorene on and off of a Au NP array showing emission near

- 910 nm. (c) and (d) Raman shift spectra for the same flakes on and off array, showing three vibrational modes: A_1^g (pink), B_{2g} (green), and A_2^g (blue). 79
- 4.6 Normalized photoluminescence spectra. Raman intensity is used as a normalization reference to scale the intensities of the PL spectra for monolayer phosphorene on and off of the nanoparticle array. 79
- 4.7 Lattice Modes in Different Materials Systems. (a) Quartz and (b) MgF_2 substrates were used in combination with PMMA and PMDS superstrates to investigate effects on lattice mode wavelength and linewidth. 81
- 5.1 Low Symmetry Nanoparticle Arrays. (a) Fabrication scheme using a Au hole array as a physical deposition mask. (b) SEM image of a sample Au hole array patterned with a rhombus-shaped nanoholes arranged in a rhombohedral lattice. (c) SEM image of a rhombohedral Al nanoparticle array showing the lattice geometry. (d) The reciprocal space for a rhombohedral lattice with first order modes shown in blue and second order modes in green. (e) Transmission spectra showing two lattice modes. 87
- 5.2 AFM of Al Nanoparticles. AFM image (a) and height profile (b) for the cross section shown in white dashed line. The arrays showed average nanoparticle heights of 100 nm. 89
- 5.3 Transmission of Nanoparticle Arrays. (a-b) Normal incident angle transmission spectra for NP arrays of two lattice angles obtained from both experiment and simulation. (c-d) Dispersion diagrams of off-normal transmission with dashed lines showing analytical Bragg modes of first order (black) and second order (blue). λ_1 and λ_2 are identified using blue and black arrows, respectively. 90
- 5.4 Near-field maps of rhombohedral and circular nanoparticles. (a-b) Phase for λ_1 showing standing waves under 0° polarization for the (1,1) mode for both rhombus-shaped and circular nanoparticles, respectively. (c-d) Phase for λ_2 showing standing

- waves under 56.5° polarization for the (1,0) mode. (e-f) Electric field intensity for λ_1 showing the (1,1) mode. (g-h) Electric field intensity for λ_2 showing the (1,0) mode. 91
- 5.5 Lasing measurements of rhombohedral array. (a) Scheme of experimental setup for lasing measurements pumping and collecting emission at normal incident angle. (b) Lasing spectrum for 67° lattice angle with overlay of dye emission. (c) Light-light curve showing evolution of lasing emission intensity for increasing pump intensity with an inset showing a zoomed-in view of the lasing threshold. 92
- 5.6 Lasing measurements with different lattice angle. (a) Lasing spectrum for 62° lattice angle with overlay of dye emission. (b) Light-light curve showing evolution of lasing emission intensity for increasing pump intensity with an inset showing a zoomed-in view of the lasing threshold. 93
- 5.7 Beam profile measurements. Far-field beam profiles for both laser wavelengths from the 62° lattice (a) and 67° lattice (b) showing directional emission with small divergence angles in all cases. 94
- 5.8 Simulated lasing near-field profiles. (a) Simulated lasing spectra of a 67° array for different in-plane polarization angles ϕ . (b) Associated near-field mappings of lattice plasmon laser emission for different polarizations plotted for the λ_1 mode (top) and λ_2 mode (bottom) showing lasing hot spots at the nanoparticle corners. 94
- 5.9 Polarization dependent lasing dynamics. Spectrally resolved time-correlated single-photon counting images showing lasing output as a function of time and wavelength for different in-plane pump polarizations in the case of a 67° array. 95
- 5.10 Lasing dynamics with different lattice angle. Spectrally resolved time-correlated single-photon counting images for a 62° array. 96
- 5.11 Trends in lasing dynamics. Emission curves showing lasing output as a function of time for a 67° array (a) and a 62° array (b). Curves are normalized and plotted on a

- linear scale. Emission decay lifetimes are included for the exponential decay functions fit to each curve. (Only time points after each peak were included in the fitting.) 97
- 5.12 Intrinsic dye dynamics. C-481 dye emission showed an intrinsic emission decay lifetime of 586 ps without a photonic cavity. 97
- 5.13 Simulated lasing dynamics. Simulated field intensity over time (a) and spectral output (b) for different in-plane pump polarizations. λ_1 lasing appears for polarizations of $0-50^\circ$ with rising times between 1-2 ps. λ_2 lasing appears for polarizations of $40-90^\circ$ with rising times between 2-3 ps. Dynamics were accelerated near ideal polarizations of 0° and 56.5° , respectively. 98

CHAPTER 1

Introduction to Plasmonics

1.1. Surface Plasmons in Metal Nanostructures

Surface plasmons are collective oscillations of conduction band electrons at the interface of a metal and a dielectric that typically show optical activity due to coupling with the electromagnetic waves of light.^{1,15} The field of plasmonics has drawn attention recently as a way to trap and confine light at the nanoscale, increasing field intensities by orders of magnitude. As a result, plasmons are often used as a tool for enhancing light-matter interactions for a broad range of applications including lasers,⁸ biological imaging agents,¹⁶ chemical sensors,⁵ photovoltaics,¹⁷ and optical lenses.¹⁸ Surface plasmons are classified into two broad categories based upon their fundamental behavior, although coupling and hybridization with different types of optical modes have been demonstrated in several systems.

1.1.1. Surface Plasmon Polaritons

Surface plasmon polaritons (SPPs) are traveling waves that propagate with wavevector \mathbf{k}_{spp} along the surface of a continuous metal film (**Figure 1.1a**).¹ The relationship for coupling an SPP mode with free space light of wave vector $\mathbf{k}_0 = \omega/c$ is described by the dispersion relation:¹⁵

$$(1.1) \quad \mathbf{k}_{spp} = k_0 \sqrt{\frac{\epsilon_d \epsilon_m}{\epsilon_d + \epsilon_m}}$$

where ω is the angular frequency of light, c the speed of light, and ϵ_d and ϵ_m the relative permittivities of the dielectric and metal. In most plasmonic systems, the dielectric function of the metal has a large, negative real part $\text{Re}(\epsilon_d) \ll 0$ and a small, positive imaginary part $\text{Im}(\epsilon_d) > 0$. In contrast dielectric materials that are non-absorbing have negligible imaginary components and their dielectric functions are characterized by the refractive index $n = \sqrt{\epsilon_d}$. These permittivities will yield a surface plasmon wave vector larger than that of free space light, which represents a momentum mismatch that prohibits direct coupling of light with surface plasmon polaritons.

To overcome the momentum mismatch, surface plasmon polaritons are often excited by light using either prism coupling or grating coupling. In the former case, evanescent fields from light in a high refractive index dielectric excite SPPs on a metal film in a low index environment that is within close

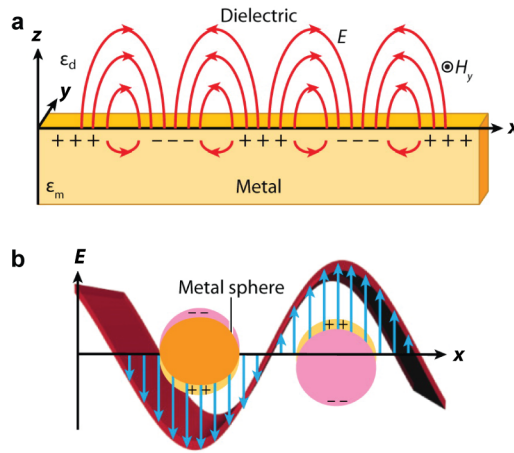


Figure 1.1. Classes of Surface Plasmons. (a) Surface plasmon polaritons propagate on the surface of continuous metal films. (b) Localized surface plasmons are confined to metal nanoparticles. Figure adapted from Henzie et al.¹

proximity (tens of nm). This is frequently performed using the Kretschmann configuration, in which a thin metal film deposited on a prism is illuminated from the back side (through the prism) to excite SPPs on the front of the film in air. In the latter case, the metal film is patterned with a periodic grating structure that contributes an additional grating vector \mathbf{G} to account for the momentum mismatch:^{19,20}

$$(1.2) \quad |\mathbf{k}_{spp}| = |\mathbf{k}_{\parallel} + \mathbf{G}|$$

where $\mathbf{k}_{\parallel} = \mathbf{k}_0 \sin(\theta)$ is the in-plane wavevector of light. The grating vector is inversely proportional to the grating spacing, so tuning of SPP modes relies upon control over the nanostructuring of plasmonic materials as discussed in **Chapter 2**.

1.1.2. Localized Surface Plasmons

Localized surface plasmons (LSPs) are oscillations confined to metal nanoparticles with dimensions smaller than the wavelength of light (**Figure 1.1b**).¹ LSP modes create regions of positive and negative charge on the surface of the nanoparticle, so the modes can be further classified as dipolar or quadrupolar oscillations, for example. This will relate to how the mode couples to light, as well as the electromagnetic fields. The resonant frequency of light for LSPs depends upon the nanoparticle size, shape, material,

and refractive index environment, so controlling these properties through synthesis techniques^{21–23} or fabrication approaches^{1,24} is key to tuning LSP modes.

1.2. Nanopatterning of Plasmonic Materials

Nanopatterning is examined in this thesis as a method for structuring plasmonic materials to engineer their optical responses and their coupling with other materials. Microfabrication was developed using photolithography to generate patterns in photoresist by shining light through a reusable binary mask (typically Cr on glass) to expose selected regions of the photoresist. While fast, scalable, and robust, this method is fundamentally limited in resolution by the wavelength of light (typically hundreds of nanometers). Therefore, the push for nanotechnology has driven developments in fabrication with tools such as electron-beam lithography and phase-shifting photolithography. Most research studies and commercial applications of nanodevices use electron-beam lithography for patterning, in which an electron-beam (e-beam) is focused to nanoscale spot sizes and scanned over a film of e-beam resist to write patterns serially²⁴. Using electrons instead of light improves the resolution to tens of nanometers or even several nanometers, but this serial writing tool scales poorly because writing time depends on pattern area.

1.2.1. Soft Lithography Tools

Phase-shifting photolithography (PSP) has been adopted by major computer chip manufacturers as modification of traditional photolithography that preserves the speed, scalability, and fidelity, with the added benefit of sub-wavelength resolution down to tens of nm. In this system, ultraviolet light is shone through a mask that may be fully transparent, but is structured topographically. The relative phase of light passing through the mask is shifted by the topographical features, creating variations in the near-field intensity that can be transferred into photoresist (**Figure 1.3**). While commercial manufacturing facilities will typically use hard (glass) masks, the same principles can be applied with soft lithography, which uses soft masks made entirely of elastomeric polymer such as polydimethyl siloxane (PDMS, commonly known as silicone) molded from a silicon master pattern.^{1,25,26}

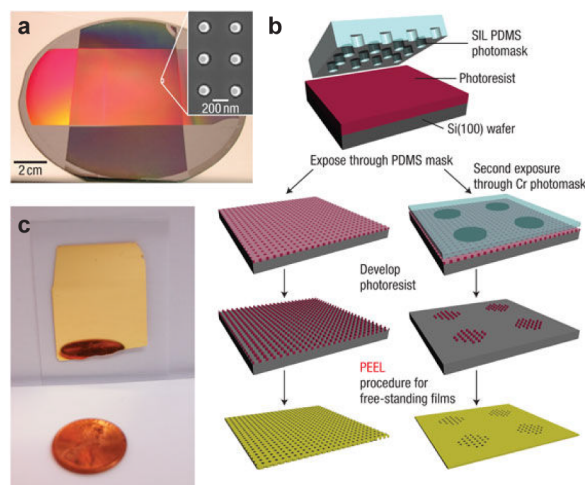


Figure 1.2. Phase-shifting Photolithography. (a) A monolithic silicon master patterned with posts arrays is fabricated using interference lithography and used to mold a PDMS mask. (b) Phase-shifting photolithography is performed to create resist posts that are then transferred into Au masks. (c) Soft lithography is used to pattern gold hole arrays over cm-scale areas. Figure adapted from Henzie et al.¹

Another type of soft lithography using PDMS masks patterned with nanoscale topography is solvent-assisted nanoscale embossing (SANE).² The PDMS mask acts as a stamp that is soaked in a solvent to load solvent into the stamp (**Figure 1.3**). Placing the solvent-loaded stamp into direct contact with a resist-coated wafer, causes the resist to dissolve and conform to the nanoscale topography of the mask. After the solvent has all evaporated, the stamp can be removed to leave the embossed resist features. This lithography technique offers high-fidelity patterning with nanoscale resolution without the use of special equipment, making it a highly versatile research tool. PSP and SANE are implemented throughout the research projects discussed in this thesis.

1.2.2. Fabrication of Nanoparticle Arrays

Following lithography, several processing steps are required to transfer the resist patterns into other materials, such as metal nanostructures. One fabrication process called PEEL was incorporated in **Chapters 3–5** for the production of nanoparticle arrays.²⁷ PEEL is an acronym for combining photolithography, etching, e-beam deposition, and lift-off to produce free-standing Au films perforated with arrays of

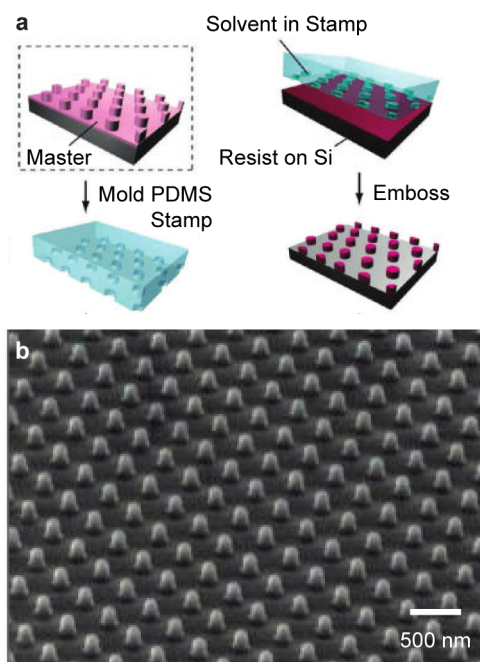


Figure 1.3. Nanopatterning with SANE. (a) A PDMS stamp is molded from a master template. The stamp is loaded with solvent by soaking and then used for embossing polymer resist. (b) An SEM image of sample photoresist post arrays patterned by SANE. Figure adapted from Lee et al.²

nanoholes. These hole arrays are useful as physical deposition masks for deposition of nanoparticles with the same shape and array structure as the nanoholes.

1.2.3. Replication Through Template Stripping

Plasmonic grating structures can be generated using template stripping, in which a metal film is deposited directly onto a patterned surface (a template) to define the film morphology. The film is then removed (stripped) from the template using an adhesive backing layer.^{28,29} Template stripping is capable of producing several identical samples with high fidelity by reusing the template pattern. Furthermore, SPP applications benefit from this fabrication method because it reduces surface roughness, which is a critical cause of energy loss in SPP systems.^{30,31} Template stripping relies upon low adhesion between the template and metal film, which creates material constraints. To resolve this issue, methods have been developed for reducing surface adhesion by incorporating an intermediate coating or release layer such

as gold³² or fluoropolymer.³³ Template stripping was incorporated in **Chapter 2** for the generation of plasmonic grating structures used in SPP studies.

1.3. Plasmonic Cavities for Enhancing Fluorescence

Metal nanostructures supporting plasmonic resonances have been used as optical resonators to couple with active materials for enhanced light matter interactions. Examples include enhanced emission from fluorescent materials^{34–39} and lasing in a variety of gain media.^{8,40,41} In former case, the nanoparticles serve as cavities with a high local density of optical states (LDOS) for trapping and confining light. Emission is therefore increased within an optical cavity according to Fermi’s golden rule that states that the radiative decay rate of an emitter is proportional to the LDOS, which is a function of wavelength, position, and dipole orientation. The increased LDOS for an optical cavity can be approximated Using the Purcell factor F :⁴²

$$(1.3) \quad F = \frac{3}{4\pi^2} \left(\frac{Q}{V_{mode}} \right) \left(\frac{\lambda}{2n} \right)^3$$

where Q is the mode quality factor, V_{mode} is the effective mode volume, λ is the resonant wavelength, and n is the refractive index of the surrounding medium. This equation helps us to identify parameters we can manipulate through proper cavity mode engineering to increase the Purcell factor F and take advantage of a high LDOS for emission enhancement. Namely, optical cavities will show the highest Purcell factor for high quality factor and small mode volumes. The following subsections will examine how this applies in the case of plasmonic nanocavity arrays.

1.3.1. Mode Volume

Plasmonic modes in general localize electromagnetic fields to hotspots with nanoscale volumes. This characteristic offers intuitively small mode volumes in comparison to photonic cavities, which cannot be confined below the diffraction limit:

$$(1.4) \quad V_{mode} > \left(\frac{\lambda}{2n} \right)^3$$

Plasmonic modes bypass the diffraction limit, allowing for smaller mode volumes that contribute to high Purcell factors. Therefore, plasmonic cavities are promising candidates enhancing fluorescent emission.

The effective mode volume V_{mode} for a cavity mode resonant at frequency ω is typically defined by^{43–45}

$$(1.5) \quad V_{mode} = \frac{\int Re \left[\frac{d(\omega\epsilon(\vec{r}))}{d\omega} \right] |\vec{E}(\vec{r})|^2 d\vec{r}}{\max \left(Re \left[\frac{d(\omega\epsilon(\vec{r}))}{d\omega} \right] |\vec{E}(\vec{r})|^2 \right)}$$

where $\epsilon(\vec{r})$ and $\vec{E}(\vec{r})$ are the dielectric constant and electric field vector respectively at position vector \vec{r} .

This simplifies to

$$(1.6) \quad V_{mode} = \frac{\int Re \left[\omega \frac{d(\epsilon(\vec{r}))}{d\omega} + \epsilon(\vec{r}) \right] |\vec{E}(\vec{r})|^2 d\vec{r}}{\max \left(Re \left[\omega \frac{d(\epsilon(\vec{r}))}{d\omega} + \epsilon(\vec{r}) \right] |\vec{E}(\vec{r})|^2 \right)}$$

by expanding the derivative. For non-dispersive cavities, the remaining derivative goes to zero in Equation 1.6, further condensing the expression. However, for cavities based upon plasmonic nanoparticles, the dispersive characteristics of the materials must be considered by including all terms in Equation 1.6 in calculations. This definition of mode volume can be conceptualized in terms of normalizing the electric field intensity and then each volume element of the cavity contributes to the mode volume according to its relative field strength.

Although this definition is commonly used to calculate the mode volume of photonic cavities, it presents the challenge of identifying an appropriate volume over which to integrate. This consideration is particularly important for plasmonic cavities that do not confine electric fields within a well-defined space, but instead support modes in open volumes. Therefore, the standard definition in Equation 1.6 diverges with increasing integration volume.^{46–48}

One way to overcome this shortcoming of the standard mode volume definition is to recognize that the mode volume diverges linearly for significantly large enough integration volumes. This is because dipole field intensity decays as $1/R^2$ in the far field while integration volume increases as R^3 , creating a linear dependence on R for the mode volume V_{mode} in Equation 1.6 for sufficiently large integration volumes. Though seemingly problematic, one simple correction is to plot the mode volume for increasing

integration distance R and use the intercept of the linear divergence to define a robust mode volume.⁴⁶ While other methods have been proposed to rigorously define mode volume,^{47,48} this particular method largely maintains the familiar definition, making it an attractive choice for mode volume calculations in practice.

1.3.2. Quality Factor

Quality factor represents the losses of light trapped in an optical resonator. In traditional Fabry–Pérot cavities, quality factor Q is defined in terms of cavity energy loss by⁴⁹

$$(1.7) \quad Q = 2\pi \frac{\text{stored energy}}{\text{energy loss per cycle}}$$

Experimentally, this may also be expressed in terms of the resonant frequency ω_0 and the resonance linewidth (full width at half maximum) $\delta\omega$ as^{49,50}

$$(1.8) \quad Q = \frac{\omega_0}{\delta\omega}$$

Conceptually, at a given resonance frequency ω_0 , a narrower linewidth $\delta\omega$ corresponds to higher quality factor Q . Plasmonic modes have notoriously poor quality factors in comparison to photonic cavities because energy is readily lost by radiative scattering and absorption in metals. For this reason, strategies for engineering plasmonic cavity modes to increase the mode volume are important for applications in enhancing fluorescent materials, as discussed in **Chapters 3 and 4**.

1.4. Applications of Plasmonics for Lasing

An important application of optical cavities is their use in laser systems. Fabry–Pérot cavities are standard for a range of lasers with different gain, including solid-state, gas, semiconductor, and dye media.^{51–66} Gain material affects wavelength, tunable range, pumping mechanisms, and timescales of lasing dynamics.^{41,67} The earliest lasers were based on insulators doped with ions: Cr:Al₂O₃ (ruby),⁵¹ Ti:Al₂O₃ (Ti:sapphire),⁵² and Nd:Y₃Al₅O₁₂ (Nd:YAG).^{53,54} Advantages of solid-state lasers include

tunable emission over hundreds of nanometers⁵² and generation of ultrashort pulses for femtosecond measurements.^{55,56}

The development of other types of gain materials produced different lasing signatures. Gas and semiconductor lasers can be electrically pumped, and so they are frequently used to optically pump other laser systems that cannot be driven electrically.^{57–59,61,62} Gas lasers rely on electrical discharge^{57–59} and have pulse durations < 0.1 ps;⁶⁶ excimer lasers are a subcategory and emit at ultraviolet wavelengths.⁶⁰ Semiconductor lasers based on light emitting diodes^{61,62} are advantageous because wavelength can be tuned by adjusting composition; for example, partial substitution of In or Al in GaAs can control the band gap over a broad range of wavelengths.⁶³ In contrast, organic dye molecules dispersed in a liquid or solid medium must be optically pumped; however, they can achieve a similar range of tunability based on broad absorption and emission spectra.^{64,65}

Plasmonic cavities have also found use in a variety of laser systems that incorporate various gain media including organic dye^{9–11,30,45} semiconductors.^{3–5,68–73} Two large classes of plasmon-based lasers are nanowire-on-film lasers and nanoparticle array lasers.

1.5. Nanowire-on-film Lasers

To compensate for large ohmic losses at optical frequencies in metal structures,⁷⁴ calculations predicted that incorporating a dielectric layer between metal and semiconductor materials could reduce losses while maintaining ultra-small mode volumes.⁷⁵ The standard-of-the-art system is composed of a semiconducting nanowire separated from a metal film by a thin dielectric spacer; the semiconductor functions as the gain material and its length defines the lateral cavity dimensions. When the spacer is reduced to nanoscale dimensions (< 10 nm), a hybrid mode is confined in the gap having features of both a waveguide mode from the nanowire and an SPP mode from the metal. Lasing from these confined modes has been observed in a wide range of materials systems^{3,4,71,76,77} (**Figures 1.4a–b**). The first nanowire-on-film plasmon laser had a lasing mode cross-section of $\lambda^2/400$ confined between a circular CdS nanowire and a Ag film.³

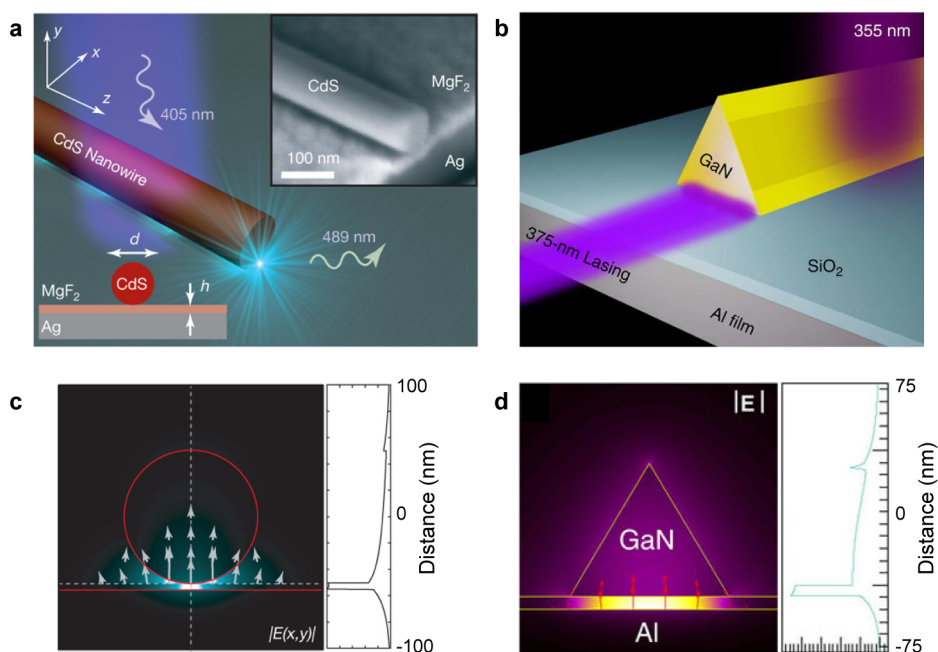


Figure 1.4. Nanowire-on-film spaser designs. (a,b) Spaser designs based upon semiconductor nanowires on plasmonic metal films may incorporate different materials depending upon laser wavelength. (c,d) Nanowire geometry influences surface plasmon polariton hybridization with waveguide modes within insulator gaps. Panels a and c adapted from Oulton et al.³ Panels b and d adapted from Zhang et al.⁴

Nanowire-on-film plasmon lasers can span visible and ultraviolet wavelengths using a variety of nanowire materials, including CdS,^{3,77} InGaN,⁷¹ GaN,⁴ and ZnO.⁷⁶ Nanowire heterostructures, which contain more than one semiconductor material, allow for broad emission spectra of laser modes spanning the entire visible spectrum.^{71,72} Nanowire shape affects the contact area defining dielectric waveguide modes and corresponding hybrid modes for lasing; hexagonal and triangular cross-sections have larger contact areas than circular ones, which can reduce scattering losses and increase plasmon-exciton coupling⁴ (**Figures 1.4c–d**). Nanowire diameter also affects efficiency of output coupling to plasmons versus photons, as revealed in dark emission from spasing.⁷⁸ Surface plasmons amplified within the cavity mode are emitted at the edges of the nanowire as evanescent waves propagating along the metal-dielectric interface, and this signal can be imaged using leakage radiation microscopy. While photon scattering also

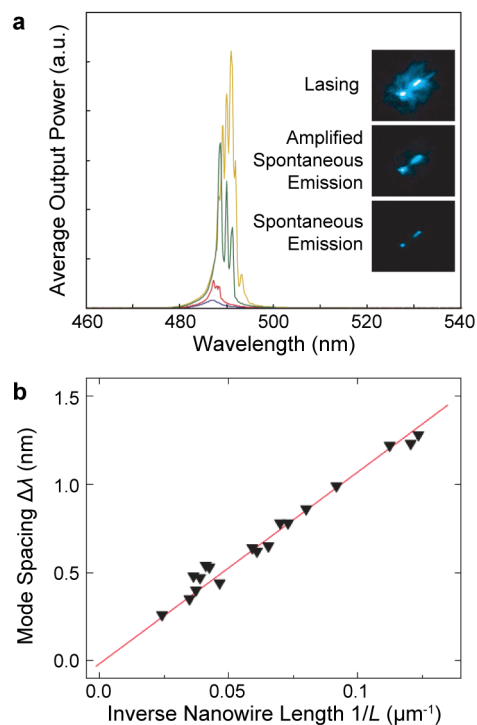


Figure 1.5. Multimodal lasing from nanowire-on-film devices. (a) Emission spectra for increasing pump intensities show progression from spontaneous emission (blue), amplified spontaneous emission (red), and multimodal lasing (green and yellow). (b) Plot of mode spacing versus inverse nanowire length $1/L$ shows a linear relationship. Figure adapted from Oulton et al.³

occurs, plasmon emission dominates the output and reaches nearly 100% efficiency at small (order of 50 nm) nanowire diameters.⁷⁸

Because semiconductor nanowires are typically several microns in length, nanowire-on-film lasers show multi-modal lasing spectra (**Figure 1.5a**) similar to Fabry-Pérot devices.³ Standing waves with an integer number of nodes along the length of the nanowire provided resonant modes for lasing, and longer or shorter nanowires dictated the mode spacing (**Figure 1.5b**). Shortening the nanowire reduced the number of lasing modes within the gain envelope, and single mode lasing emerged at nanowire lengths of roughly 200 nm.⁷² Single-mode lasing has also been achieved with semiconductor nano-square patches on plasmonic films using the total internal reflection of SPP modes for feedback.^{70,79} The number of

supported modes depended on the geometry of the patch, with micron-sized square patches exhibiting multiple modes and breaking the symmetry resulting in single-mode emission.⁷⁰

One attractive feature of nanowire-on-film plasmon lasers is the fast decay dynamics compared to nanowire photonic lasers without metal films.⁷⁶ The spontaneous carrier recombination rate can be several times faster for plasmon modes compared to photonic modes. As a result of these short lifetimes, plasmonic systems can achieve lasing pulse widths < 800 fs, around ten times shorter than their photonic counterparts.⁷⁶ Because lasers based upon SPPs tend to exhibit high ohmic losses from the metal, early work required cryogenic temperatures.^{3,71} Improvements in design and fabrication, however, have since lowered the lasing thresholds and allowed operation at room temperature.^{4,76,77} Another limitation for nanowire-on-film lasers is their lack of directional emission in the far-field since the light is scattered from the end-facets of the nanowire;³ however, these devices can be integrated with waveguides to direct emission. For example, semiconductor nanobelt waveguides can direct the output light from lasing cavities formed by the intersection of the nanobelt and a plasmonic metal strip.⁶⁸ Such architectures enable wavelength multiplexing and potential electrical modulation for on-chip applications.

Nanowire-on-film lasers can be used for lasing-enhanced sensing, where analytes are detected based on changes in lasing output.^{5,69,79} Most plasmon-based sensors monitor local changes of refractive index in plasmon wavelength, where a common figure of merit is wavelength shift per refractive index unit divided by peak width.^{79–81} Hence, sensors based on broad plasmon resonance linewidths (10–100 nm) have limited sensitivity.⁷⁹ In contrast, lasing signals are very narrow (order of 1 nm) and allow for easily-resolved shifts in peak wavelength or amplitude for small changes in index.^{69,79} Nanowire-on-film lasing sensors are also sensitive to fluctuations in lasing intensity.⁵ For example, explosives (2,4-dinitrotoluene; ammonium nitrate; and nitrobenzene) were detected at few-ppb or even sub-ppb concentrations in air with almost no measurable interference from common air species (**Figure 1.6**). The low detection limits were possible due to surface chemistry effects on the gain. Adsorption of analyte on semiconductor nanowires reduced non-radiative exciton decay channels, which caused longer exciton lifetimes and increased lasing intensity without changing peak wavelength.⁵ These effects were reversible and changes in analyte concentration could be monitored in real time.

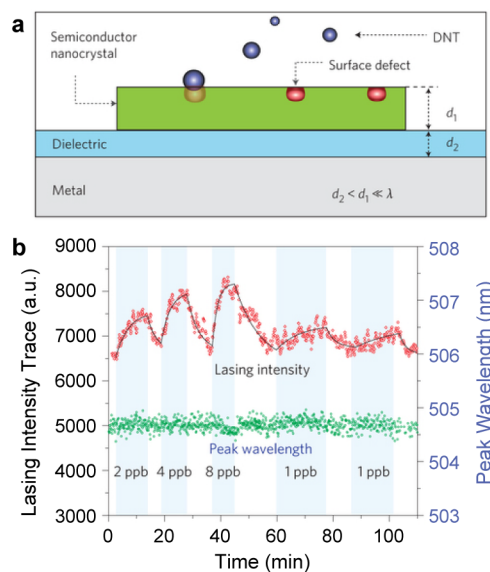


Figure 1.6. Lasing-based sensors for explosives. (a) Scheme for DNT sensing based on a nanowire-on-film laser. (b) Laser intensity shows ppb sensitivity to DNT in the surrounding environment while laser wavelength remains unchanged. Figure adapted from Ma et al.⁵

1.6. Nanoparticle Array Lasers

LSP modes of individual nanoparticles generally show broad spectral lineshapes corresponding to high loss and poor quality factor Q . For this reason, using individual nanoparticles as optical resonators for lasing is challenging. A large contribution to loss in LSP modes is radiative dipolar oscillation by the nanoparticles, so strategies for mitigating this loss mechanism could contribute to improved quality factors. One such strategy is to arrange the nanoparticles in a periodic lattice. Under proper material and geometry conditions, this lattice configuration allows the nanoparticles to oscillate in phase with one another, canceling out the radiative dipole loss.⁷ This interaction of the particles in a lattice is observed both experimentally and theoretically as sharp peaks in the the extinction spectra (**Figure 1.7**). The sharp spectral features are called lattice plasmon modes or surface lattice resonances, which arise from the hybridization of individual nanoparticle LSP with Bragg diffraction modes. Bragg modes occur for periodic lattices in a uniform refractive index environment, and they depend on both lattice spacing and refractive index.⁸² Interference between the discrete state of the Bragg mode with the continuum of states

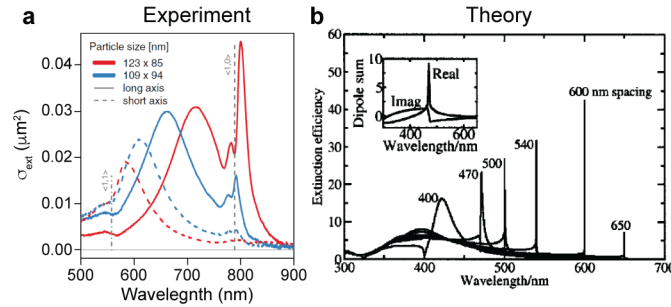


Figure 1.7. Lattice plasmons with sharp resonances in periodic metal nanoparticle arrays. (a) Experimental demonstration of sharp lattice plasmon resonances from gold nanorod arrays. (b) Simulated extinction spectra of a 1D chain of silver nanoparticles with varying spacings by coupled dipole method. Inset shows the real and imaginary parts of the normalized dipole sum. Panel a adapted from Auguie et al.⁶ Panel b adapted from Zou et al.⁷

of the LSP creates a Fano-type lineshape in the transmission spectrum. This sharp spectral peak can be optimized to create a high quality lattice plasmon mode by tuning the LSP based on nanoparticle size (**Figure 1.7a**) or the Bragg mode based on lattice spacing (**Figure 1.7b**).

Nanoparticle arrays supporting lattice plasmon modes are ideal candidates for nanoscale laser devices and have been demonstrated in a number of configurations.^{9–11,83} The typical setup for these devices is to fabricate plasmonic nanoparticle arrays on a glassy substrate, and incorporate a gain material in the form of a superstrate coating (**Figure 1.8a**). An example would be an organic laser dye, such as IR-140 with NIR emission, dispersed in either a polymer matrix (polyurethane) or an organic solvent (dimethyl sulfoxide) with a refractive index matching the substrate. The completed devices show lattice plasmon modes with dispersive character following the diffraction mode of the array for different angles of incidence (**Figure 1.8b**). At normal angle of incidence (k_{\parallel}), the lattice mode has zero group velocity ($d\omega/dk_{\parallel} = 0$), which identifies a standing wave with a high local density of optical states (**Figure 1.8b** red circle). The phase mapping for near-field simulations also shows standing wave behavior in the form of bands of constant phase for all of the nanoparticles (**Figure 1.8c**).

Lasing experiments using lattice plasmons coupled to dye excitons shows narrow emission linewidths (< 1.5 nm) above the lasing threshold (**Figure 1.8d**). Lasing threshold can be studied by examining the emission intensity as a function of pump intensity (**Figure 1.8e**). The lasing threshold is observed

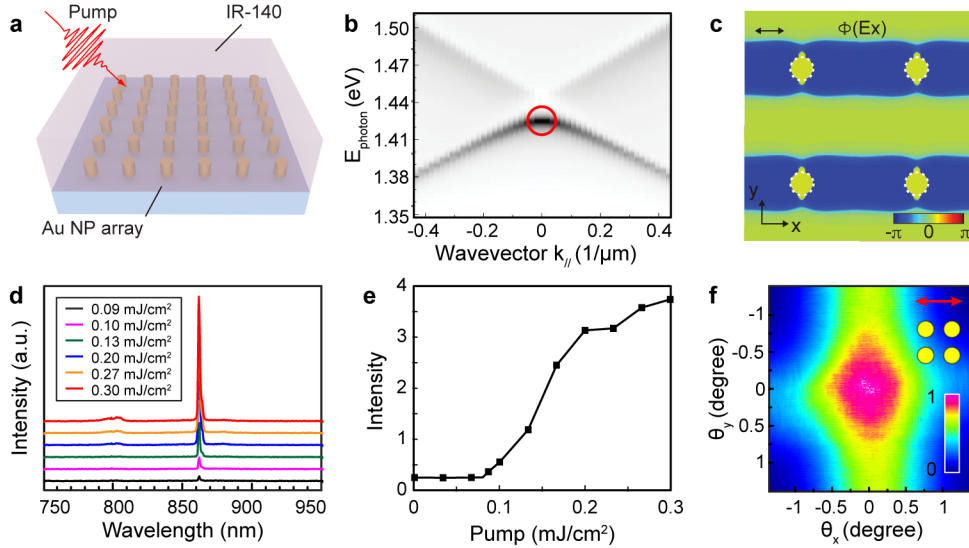


Figure 1.8. Directional lasing from NP arrays. (a) Scheme of a laser device including gold NP arrays embedded in liquid or solid-state gain media. (b) Calculated optical band structure. (c) Simulated phase profile at lattice plasmon resonances. (d-e) Power dependent lasing emission and input-power output-intensity curves. (f) Far-field beam profile with a highly directional lasing spot. Panel a adapted from Wang et al.⁸ Panel b adapted from Wang et al.⁹ Panels c-e adapted from Zhou et al.¹⁰ Panel f adapted from Yang et al.¹¹

as a sudden change in slope for the emission intensity. Unlike nanowire-on-film lasers that shows non-directional scattering of their laser emission, lattice plasmon lasers take advantage of diffractive coupling as an emission channel to provide highly directional laser output (**Figure 1.8f**). In most studies, the far-field beam profile showed laser emission normal to the nanoparticle array and with a beam divergence of less than 1.5° .

Engineering lattice plasmon lasers has allowed for tailoring of their emission with interesting properties. The first example of this is in the form of real-time tunability of laser emission wavelength through changes in the dielectric environment (**Figure 1.9**).¹¹ In this configuration, liquid gain material (dye in organic solvent) is sandwiched between the nanoparticle array and a cover slip for capping (**Figure 1.9a**). The refractive index environment could be changed statically by switching the substrate material, and this shifted the lattice mode lasing wavelength even though the nanoparticle geometry and lattice spacing was fixed (**Figure 1.9b**). Taking this strategy a step further, a microfluidic channel allowed for gain

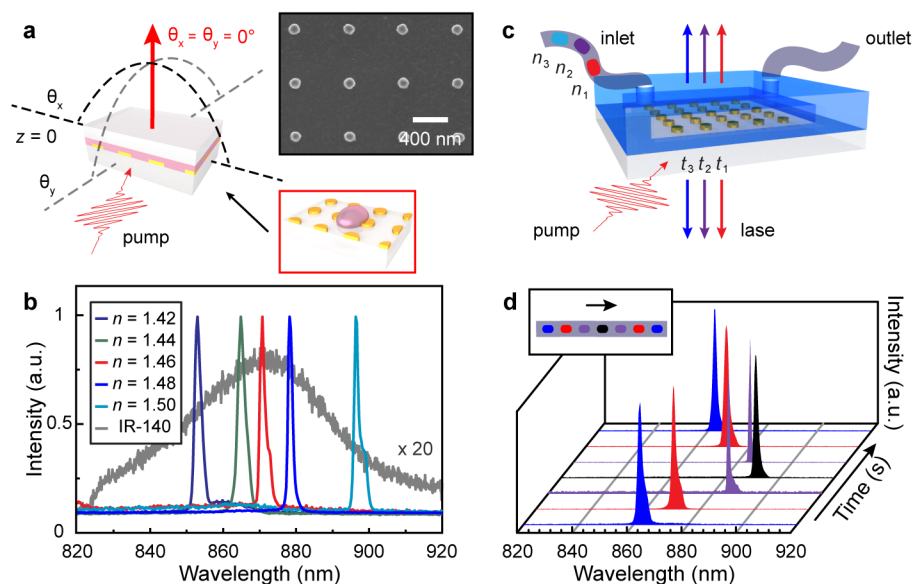


Figure 1.9. Real-time tunable nanolasing from plasmonic nanoparticle arrays by refreshing liquid dye solutions. (a) Scheme of a lasing device consisting of gold NP arrays sandwiched between liquid dye solutions and a glass coverslip. (b) Statically tuned lasing wavelengths can span the entire emission bandwidth of the dye. (c) Scheme of the dynamic laser with a microfluidic channel. (d) Continuous shifting of lasing emission to longer wavelengths and then back to shorter wavelengths. Figure adapted from Yang et al.¹¹

medium to be refreshed by pumping through dye dissolved in solvents of varying refractive index (**Figure 1.9c**). The lasing wavelength was thereby dynamically tuned with a spectral range spanning the emission bandwidth of the dye (**Figure 1.9d**). This device relied upon the tolerance of lattice plasmon modes to slight mismatch in refractive index between the substrate and superstrate materials ($\Delta n < 0.05$). This study demonstrated the utility of refractive index for engineering the plasmonic resonances for novel applications, and this concept will be touched on in the process of selecting device materials in (**Chapters 3 and 4**).

A second example of engineering lattice plasmon lasers is using device structuring to generate multimodal lasing emission.⁹ This study used hierarchical structuring to form superlattices composed of nanoparticle array patches. The nanoparticle arrays had a spacing of 600 nm like in previous studies, and the patches offered an additional periodicity of several microns (**Figure 1.10a**). This multiscale

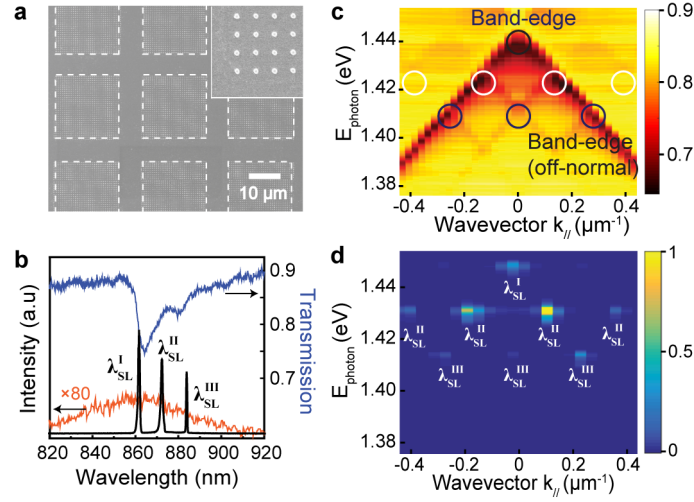


Figure 1.10. Multi-modal nanolasing in gold nanoparticle superlattices surrounded by liquid dye solutions. (a) SEM image of gold superlattice arrays with NP spacing $a_0 = 600$ nm, patch side length $l = 18$ nm and patch periodicity $A_0 = 24$ nm. (b) Lasing emission profile (in black), dye emission profile (in orange) and linear optical properties (in blue). (c) Measured optical band structure of superlattice arrays. (d) Angle-resolved emission spectra of multi-modal lasing. (e) Switchable lasing between single and multiple lasing peaks from symmetry-broken NP line patches. Figure adapted from Wang et al.⁹

patterning created coupling between the lattice plasmons of the finite patches of nanoparticle and the diffraction mode from the patch periodicity. This interaction generated multiple superlattice plasmon modes seen in both the cavity transmission spectrum and lasing spectrum when integrated with dye (**Figure 1.10b**). While infinite arrays of nanoparticles showed a single band edge state with zero group velocity at normal angle ($k_{\parallel} = 0$), the nanoparticle superlattices showed several band edge states at both normal and off-normal angles due to crossing of superlattice diffraction modes (**Figure 1.10c**). The plasmonic lasing followed the array band structure, showing emission from the band edge states (**Figure 1.10d**). This study is a prime example of tailoring the optical responses of plasmonic devices through modifications to the geometrical structure, and additional methods for controlling photonic responses and lasing through device symmetry will be discussed in **Chapter 5**.

CHAPTER 2

Sequential Feature-Density Doubling for Ultraviolet Plasmonics

Referenced work: M. P. Knudson, A. J. Hryn, M. D. Huntington, and T. W. Odom, "Sequential feature-density doubling for ultraviolet plasmonics." *ACS Applied Materials and Interfaces* 9, 33554-33558 (2017).

2.1. Introduction for Patterning Tools

Chemical synthesis^{21,22} and nanofabrication^{1,24} are two complementary methods that can generate plasmonic nanostructures. As a bottom-up approach, synthesis adjusts growth conditions to control particle size and shape for targeted optical responses.^{21,22} Plasmonic resonances in the ultraviolet (UV) range require materials with suitable dielectric functions, such as Al and Ga.⁸⁴ These materials often require difficult procedures to prevent oxidation, show undesired heterogeneity, and form a limited range of nanoparticle geometries compared to conventional plasmonic materials Au and Ag.^{22,24,85,86} In contrast, top-down fabrication approaches provide better uniformity and control over nanostructure organization to realize collective optical interactions.^{1,24} Although procedures are reasonably well-developed for designing plasmonic substrates at visible and infrared wavelengths,¹ UV plasmons require not only materials with low losses in this range but also smaller sizes and spacings.²⁴ The ability to access increasingly smaller periodicities is needed for emerging plasmonic applications in photocatalysis,^{87,88} enhanced fluorescence,³⁶ enhanced Raman spectroscopy,⁸⁹ and lasing.⁴

The production of nanostructures with periodicities on the order of 100 nm over macroscale areas is challenging using common patterning techniques. Serial writing methods, such as electron-beam lithography, are time-consuming for dense features and require writing rates on the order of 10 days/cm² for 100-nm pitch structures using typical electron-beam conditions.^{90,91} Interference lithography can pattern wafer-scale areas in a single step but involves specialized setups to produce periodicities below 200 nm.²⁴ For example, a 157-nm laser interferometer carefully aligned with a vacuum, UV-grade sapphire prism and a high-index immersion liquid can generate resist gratings with 44-nm periodicity.⁹² Molding and printing methods based on patterned molds or stamps, such as nano-imprint lithography^{24,89} and soft lithography,^{1,2,93} are powerful tools for large areas but still rely upon other techniques to create the patterns on the stamps.

One strategy to create smaller periodicities is self-aligned double patterning by sidewall image transfer.⁹⁴ This process is a type of edge lithography where the outlines of lithographically defined features are transferred into the substrate with twice the feature density of the original pattern. Preparation of hard masks involves anisotropic dry-etching of oxide or nitride thin films whose thickness determines the final

linewidth. Since etching through thick masking layers can damage the underlying material, self-aligned double patterning typically uses thin films to target linewidths <25 nm and periodicities <50 nm,^{94,95} although periodicities up to 100 nm have been achieved.⁹⁶

In this chapter we demonstrate a feature-density doubling method that spans periodicities in the 100–200 nm range with an application for UV plasmonics. Our approach incorporates wet-etching to pattern atomic layer deposition (ALD)-deposited alumina on silicon wafers. Using thin (5-nm) alumina films as masks for controlled wet over-etching, we tuned feature sizes down to several nanometers with high uniformity. To demonstrate functionality of the nanopatterns, we transferred silicon line gratings patterned >3 cm² into aluminum gratings with excellent fidelity by template-stripping. These substrates displayed UV plasmon modes that were tunable in the range of 300–400 nm based on sample periodicity and incident angle.

2.2. Fabrication of Si Lines Through Sequential Feature Density Doubling

Figure 2.1a depicts the process for tuning nanostructure features by wet over-etching of alumina. First, polymer resist was patterned by solvent-assisted nanoscale embossing (SANE)² on a 5-nm thin film of ALD-deposited alumina on silicon (Si) wafers. The resist was used as an etch mask to protect the alumina during wet-etching, where the widths of alumina lines depended on etching time. We started with a fixed resist pattern of periodic lines with $a = 450$ nm as well as a 48% duty cycle (linewidth divided by line periodicity) since 50% duty cycles are common and so that we could easily extend this starting pattern to other (smaller) linewidths by wet over-etching. Alumina lines were then used as a mask for deep reactive ion etching (DRIE) to transfer the patterns into Si. We achieved a wide range of duty cycles from 48% to 8% (**Figure 2.1b–i**), which corresponded to 83% reduction in linewidth. For our recipe, Si features were dry-etched to a depth of 70 nm using DRIE process times of 30 s (**Figure 2.2**).

We determined that ALD alumina was a desirable masking material because of a combination of material properties. First, over-etching could be controlled to several nm because the wet-etching rate of alumina depended on temperature. Etching at 50°C produced a linear over-etching rate of 1 nm/s

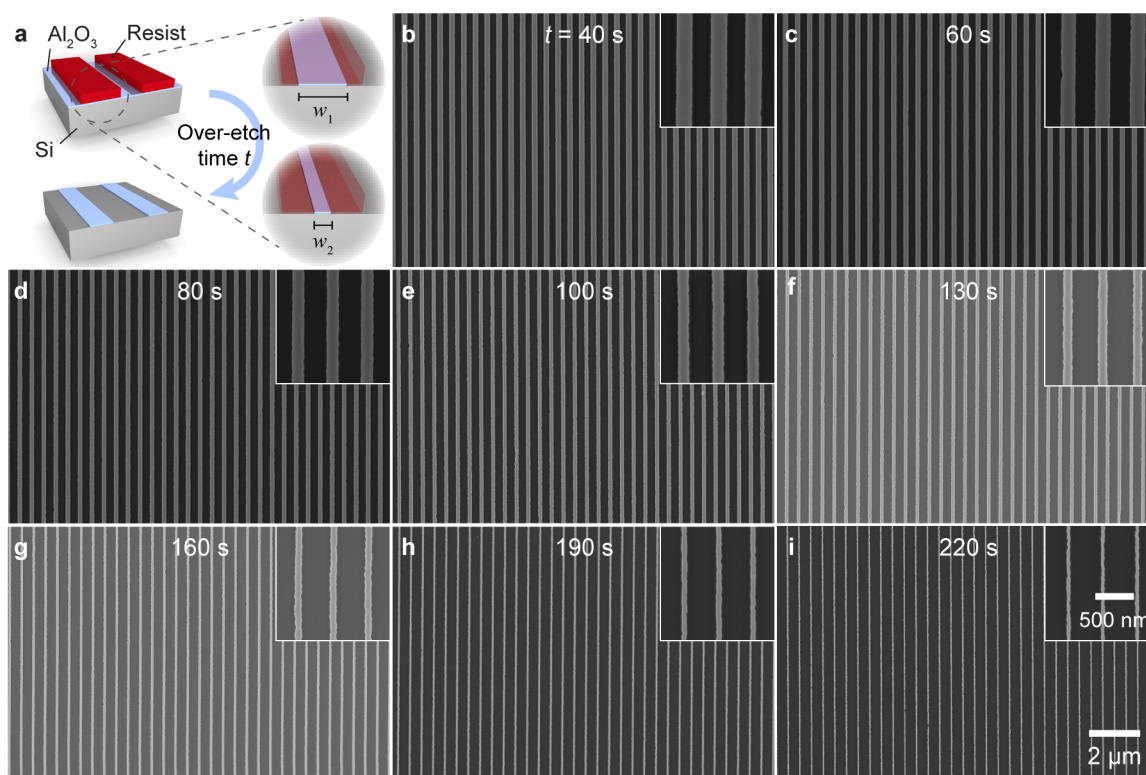


Figure 2.1. Tunable linewidths. (a) Controlled wet over-etching of ALD-alumina lines for use as DRIE masks. (b)–(i) SEM images of Si lines after DRIE showing decreasing Si linewidths for increasing wet over-etching times.

with a root mean square (RMS) error of 4 nm in the linear regression (**Figure 2.3**) that represented the random deviation of observed linewidths from expected values. Second, small feature sizes were possible because the wet-etched ALD patterns showed low line-edge roughness. Linewidths down to 40 nm could be achieved at the longest wet-etching time of $t = 220$ s, while etching beyond this time caused discontinuities in the lines. We characterized the RMS line edge roughness from SEM images (**Figure 2.4**) and found that typical values ranged from 2 nm for short wet-etch times up to 5 nm at the longest times (**Figure 2.5**). In comparison, previous work on wet over-etching using Cr thin films showed a roughness of ca. 25 nm for wet-etching only a few seconds.⁹⁷ Third, we found that a thin 5-nm alumina mask was sufficient to dry-etch Si features >70 nm deep because ALD alumina is resistant to SF₆ plasma etching.^{98,99}

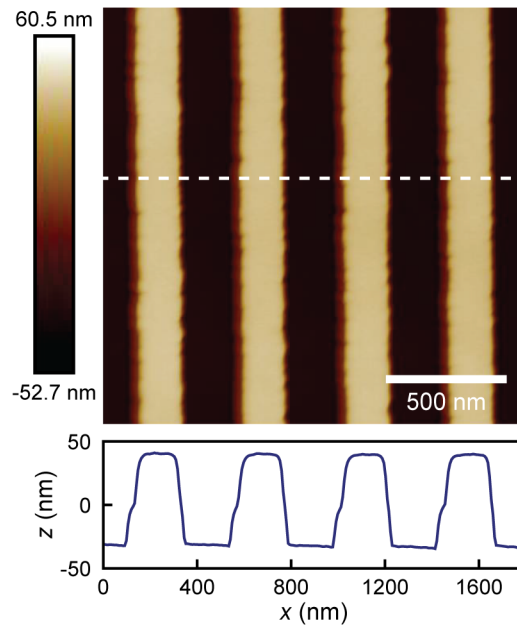


Figure 2.2. Atomic force microscopy (AFM) data for Si lines. Image and cross section for $t = 130$ s of alumina wet over-etching. Using a DRIE time of 30 s, Si etch depth is 70 nm for these samples. Features appear wider than corresponding SEM image due to AFM tip effects.

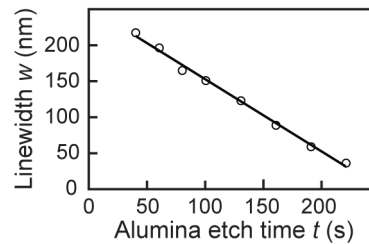


Figure 2.3. Trend in linewidths for wet over-etching times. The plot shows a linear trend with a slope of -1 nm/s and a root mean square error of 4 nm.

Figure 2.6 shows our feature-density doubling scheme using a parent line array with periodicity $a = 400$ nm to generate a daughter array with periodicity $a' = a/2 = 200$ nm. The starting periodicity was chosen to provide round numbers in each generation, and a large duty cycle (75%) was used to meet requirements of our doubling scheme. (i) A parent Si array was used to create a PDMS mold for (ii) patterning polymer resist lines using SANE on an ALD alumina-coated Si wafer. (iii) Resist features served as a wet-etching mask for the alumina layer, which created a set of alumina lines with periodicity

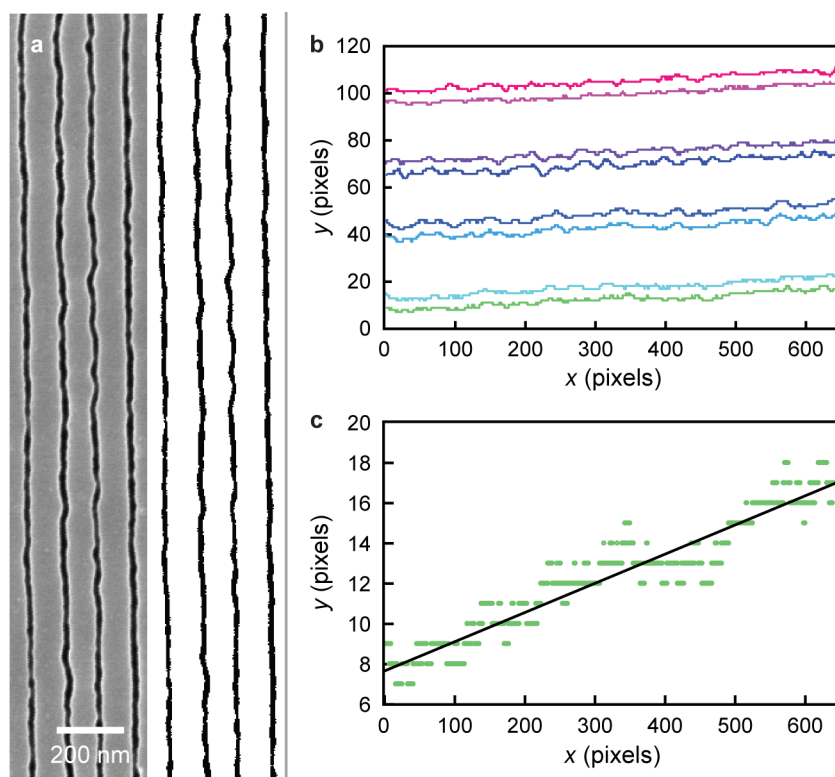


Figure 2.4. Image processing and edge fitting for computing roughness. (a) SEM image of a Si line pattern with $a'' = 100$ nm periodicity before (left) and after (right) converting to binary black and white coloration. The image includes eight edges, each 2.2 microns long. (b) The black and white regions are used to define a set of points along the line edges with pixel connectivity 8. (c) Each edge is individually fit to a least-squares line, and the mean square error of each linear fit is converted from units of pixels to nm. The mean square error is averaged for eight edges to determine the mean square error line edge roughness in nm for each sample.

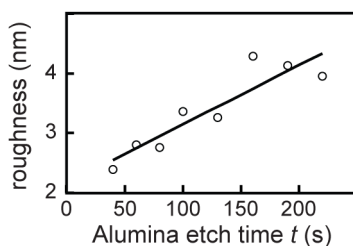


Figure 2.5. Trend in roughness with etch time. Each data point represents the average line edge roughness for the corresponding image in **Figure 2.1** using 8 edges per sample, each 2.2 microns long. Line edge roughness is ~ 3 nm for short etch times and increases slightly as wet etch time increases. The linear fit has a slope of 0.01 nm/s and a root mean square error of 0.3 nm.

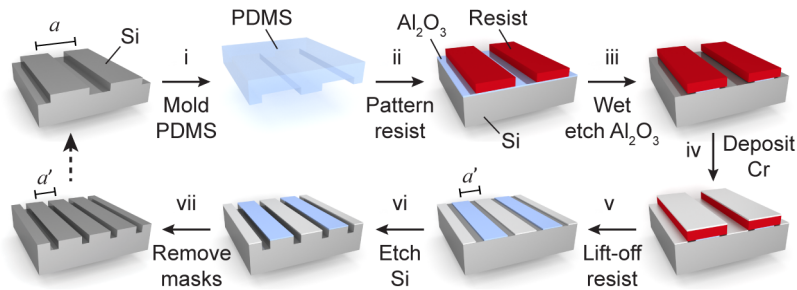


Figure 2.6. Feature density doubling process. A parent Si pattern with line periodicity $a = 400$ nm was used to generate a daughter Si pattern with periodicity $a' = 200$ nm. A second doubling sequence produced a granddaughter pattern with periodicity $a'' = 100$ nm.

$a = 400$ nm. (iv) Cr deposition normal to the surface and (v) resist lift-off produced a set of Cr lines also with periodicity $a = 400$ nm in-between alumina lines. (vi) Together, alumina and Cr lines formed an effective mask with periodicity $a' = 200$ nm for DRIE processing to create a daughter pattern in Si. (vii) Once the Cr and alumina lines were removed, the Si pattern with periodicity $a' = 200$ nm could be used for the next sequence of feature-doubling. For this scheme to produce uniform Si linewidths, we needed to ensure the alumina and Cr masks had equal dimensions. Since the Cr linewidths were fixed based upon the gap size between resist lines, the alumina was precisely matched to the Cr by tuning the wet-etching times (**Figure 2.3**).

We performed two sequences of feature-density doubling to produce Si lines of increasingly smaller periodicities (**Figure 2.7**), starting with a parent Si line array of $a = 400$ nm patterned by interference lithography (>3 cm²) (**Figure 2.7a**, inset). The first doubling process created $a' = 200$ nm, and a PDMS mask from this array was then used for a second cycle of doubling to produce an array of $a'' = 100$ nm. We found that 100 nm was the lower bound for this combination of PDMS masks and materials substrate since narrower features with high aspect-ratios did not transfer well for SANE. Periodicities of $a' = 200$ nm and $a'' = 100$ nm in Si were too small to show diffraction at visible wavelengths, although contrast between patterned and un-patterned areas of the wafer was evident.

Linewidths for the three generations were 299 ± 2 nm, 142 ± 4 nm, and 76 ± 7 nm with a fixed duty cycle of $\sim 75\%$. The same DRIE process was applied to all three generations for transferring the patterns into

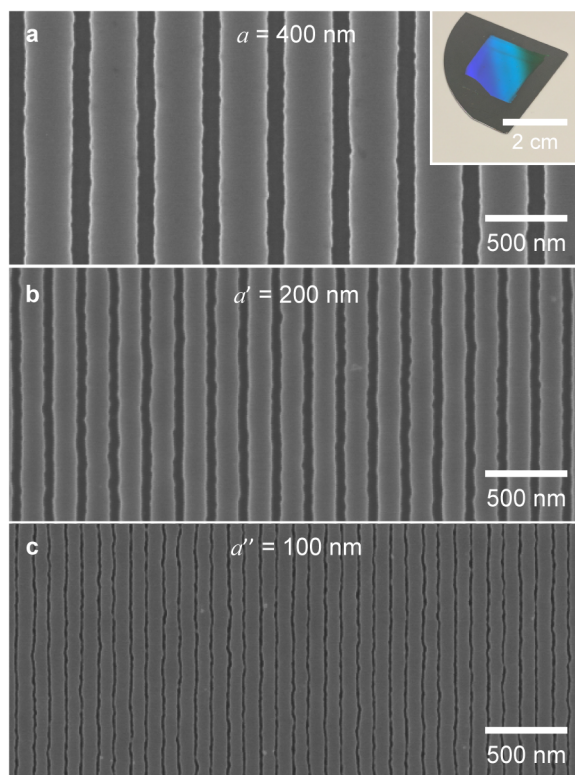


Figure 2.7. Two sequences of feature density doubling. SEM images of periodic Si lines. (a) Generation 1: $a = 400$ nm with a photograph inset to show total patterned area >3 cm². (b) Generation 2: $a' = 200$ nm. (c) Generation 3: $a'' = 100$ nm.

Si and produced feature heights of 70 nm, 50 nm, and 35 nm, depending upon trench width (**Figure 2.8**). Differences in height were likely from aspect-ratio dependent etching, a common phenomenon in which narrower features are dry-etched to shorter depths.¹⁰⁰ Two factors may limit etching of even narrower feature sizes. First, ALD-alumina masks had vertical sidewalls (89°) with our DRIE recipe, but Cr masks produced sidewalls with an 84° slope (**Figure 2.9**). Second, for both mask materials, dry-etched features were slightly rounded at the base with a radius of curvature of 20 nm. Nevertheless, our methods and materials could produce dry-etch depths down to 90 nm (**Figure 2.9**). Wet-etched ALD alumina and evaporated Cr also produced indistinguishable line edge roughness, so the mask materials were further complementary for our doubling scheme. The RMS line edge roughness for each generation was between 3–4 nm, and no trend was observed across generations since wet-etch times were relatively short (<120

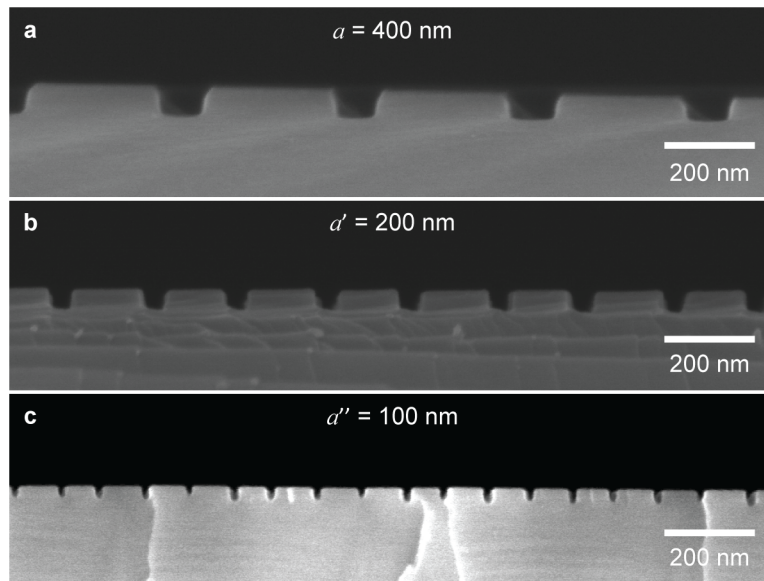


Figure 2.8. Cross sections of etched Si lines. SEM cross sections show Si line patterns with periodicities $a = 400$ nm (a), $a' = 200$ nm (b), and $a'' = 100$ nm (c). Etch depths for these patterns are 70 nm, 50 nm, and 35 nm, respectively, using the same DRIE process for each sample. Differences in etch depth are attributed to aspect ratio dependent etching, a well-known phenomenon in which narrower features are etched to shorter depths in DRIE.

s). Importantly, roughness did not transfer from one generation to the next to a noticeable degree, which we attribute to the smoothing of resist features during SANE.

2.3. Transfer of Patterns into Plasmonic Materials

Our nanopatterned Si substrates were ideal for producing plasmonic gratings using template stripping (**Figure 2.10a**), in which the original pattern directly defines sample topography.^{29,30,32} (i) We briefly treated the Si templates with a C_4F_8 plasma to produce a thin conformal fluoropolymer coating on the Si surface that acted as a release layer to prevent adhesion.³³ (ii) An optically thick film (120 nm) of Al was then deposited onto the Si templates by electron-beam evaporation, and (iii) UV-curing of an optical adhesive (NOA 61, Norland Products Inc.) was used to strip the patterned Al from the Si templates. The final substrates were Al line gratings with periodicities of $a = 400$ nm, $a' = 200$ nm, and $a'' = 100$ nm (**Figures 2.10b–d**) for which the entire patterned Si areas could be transferred into Al (**Figure 2.10b**, inset). These Al patterns could be formed up to 65 nm tall, about the depth of the Si templates; their

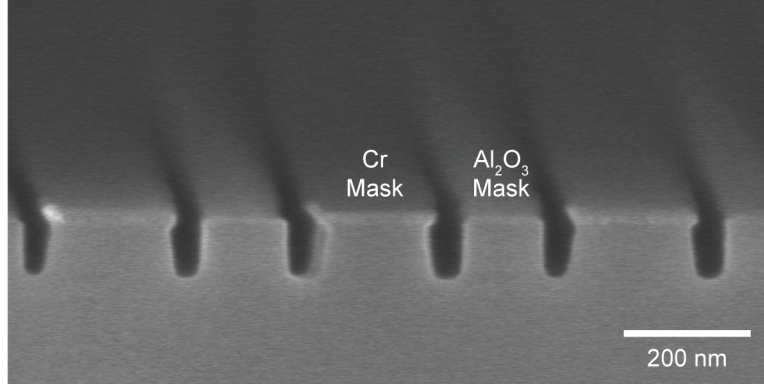


Figure 2.9. SEM cross sections showing etching profiles. Alternating lines of evaporated Cr (wide) and ALD alumina (narrow) were used for masking Si during DRIE etching. The different widths allowed identification of mask materials. Cr masks produced slightly slanted sidewalls ($\sim 84^\circ$) during DRIE processing, while ALD alumina masks produced vertical sidewalls ($\sim 89^\circ$). All sidewalls, however, were sufficiently vertical for the feature-doubling process. Si lines were etched to a depth of 90 nm with evaporated Cr and ALD alumina masks, 7-nm and 5-nm thick, respectively, showing potential for high etch depths with these thin film materials.

linewidths (83 ± 2 nm, 55 ± 3 nm, and 22 ± 2 nm) were slightly narrower than trenches in Si patterns because of the fluoropolymer coating (**Figure 2.11**). These nanoscale dimensions are ideal to excite surface plasmon polaritons (SPPs).⁸⁸

2.4. Optical Properties of Al Gratings

We tested the plasmonic properties of the Al line arrays by analyzing their reflectance spectra. Periodic nano-grating structures support SPP modes described by^{19,20}

$$(2.1) \quad |\mathbf{k}_{spp}| = \frac{\omega}{c} \sqrt{\frac{\epsilon_d \epsilon_m}{\epsilon_d + \epsilon_m}} = |\mathbf{k}_{\parallel} + \mathbf{G}|$$

where ω is the angular frequency of light, c the speed of light, and ϵ_d and ϵ_m the relative permittivities of the dielectric and metal. $\mathbf{k}_{\parallel} = \mathbf{k}_0 \sin \theta$ is the in-plane wavevector of light with momentum \mathbf{k}_0 incident at angle θ . \mathbf{G} is the Bragg vector with components of the form $iG_x = i\frac{2\pi}{a}$ that depend upon periodicity a and mode order i . **Figure 2.12** shows the reflectance properties of Al line gratings measured in air

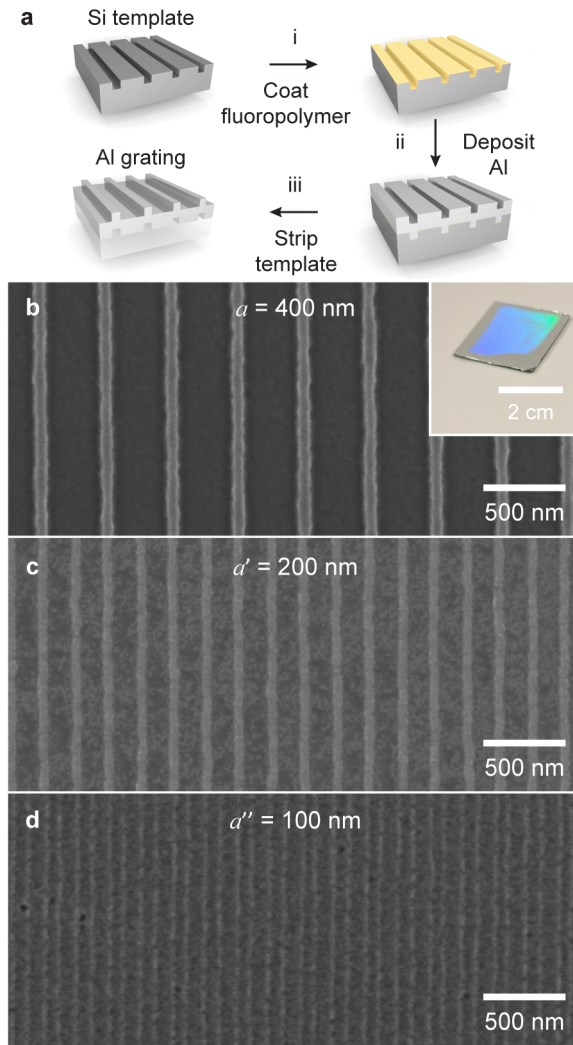


Figure 2.10. Template-stripped Al line patterns. (a) Template stripping scheme. (b–d) SEM images of Al line gratings with $a = 400$ nm, $a' = 200$ nm, and $a'' = 100$ nm. Photograph inset shows a patterned area >3 cm² that is identical to the template in **Figure 2.10a**.

($n = \sqrt{\epsilon_d} = 1.0$) over the wavelength range 200–900 nm with incident angles varying from $\theta = 5^\circ$ to $\theta = 55^\circ$ in increments of 5° . For one-dimensional line patterns, the SPP dispersion relation simplifies to

$$(2.2) \quad \frac{\omega}{c} \sqrt{\frac{\epsilon_d \epsilon_m}{\epsilon_d + \epsilon_m}} = k_0 \sin \theta + i \frac{2\pi}{a}$$

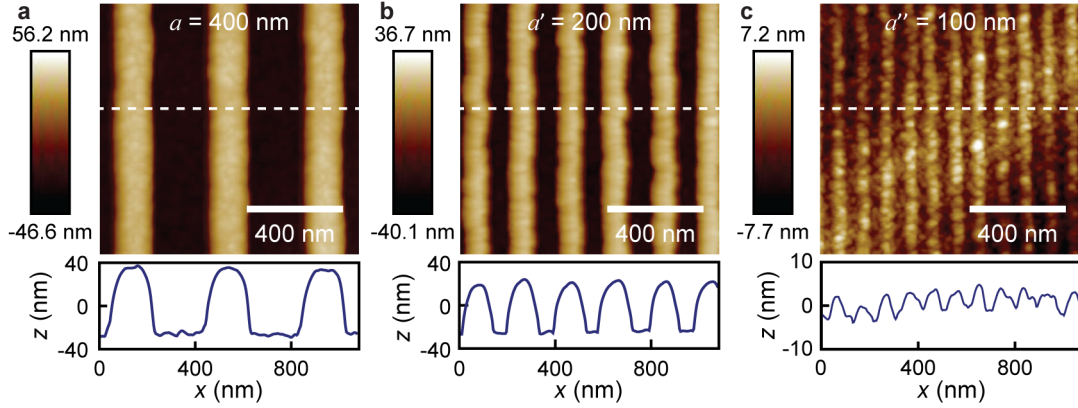


Figure 2.11. AFM data for Al lines. Images and cross sections for Al line arrays with periodicities (a) $a = 400$ nm, (b) $a' = 200$ nm, and (c) $a'' = 100$ nm. Heights are 65 nm, 45 nm, and 5 nm, respectively, which are consistent with Si line depths within 5 nm aside from the $a'' = 100$ nm sample. The sharp minima in the $a'' = 100$ nm cross section, however, suggest the AFM tip was too wide to reach the bottom of the trenches between lines. AFM tip effects prevented measuring the full depth, and so the true feature height was likely larger than 5 nm.

The $a = 400$ nm Al lines showed two distinct SPP modes: one at visible wavelengths corresponding to the first order ($i = 1$) SPP mode and a second at UV wavelengths corresponding to the second order ($i = 2$) SPP mode (**Figure 2.12a**). The $a' = 200$ nm Al lines showed a single SPP mode at UV wavelengths matching a first-order ($i = 1$) SPP dispersion relation and no features at visible wavelengths (**Figure 2.12b**). The $a'' = 100$ nm Al lines showed no optical modes (**Figure 2.12c**) because the expected wavelengths were below the 200-nm cutoff for measurements in air. Large-area patterns enabled incident angles to be swept up to 55° and allowed SPP modes to be tuned over a broad wavelength range because of their dispersive character. SPPs coupled to longer wavelengths of light at higher incident angles for $a = 400$ nm and $a' = 200$ nm, and the measurements agreed with Equation 2 as well as finite-difference time-domain simulations (**Figure 2.13**).

2.5. Summary

In summary, we demonstrated a feature-density doubling method to access periodicities down to 100 nm over cm^2 -scale areas. We expect this advance in nanofabrication will enable UV optical devices for applications in sensing and catalysis. Also, since the patterned Si substrates can function as masters,

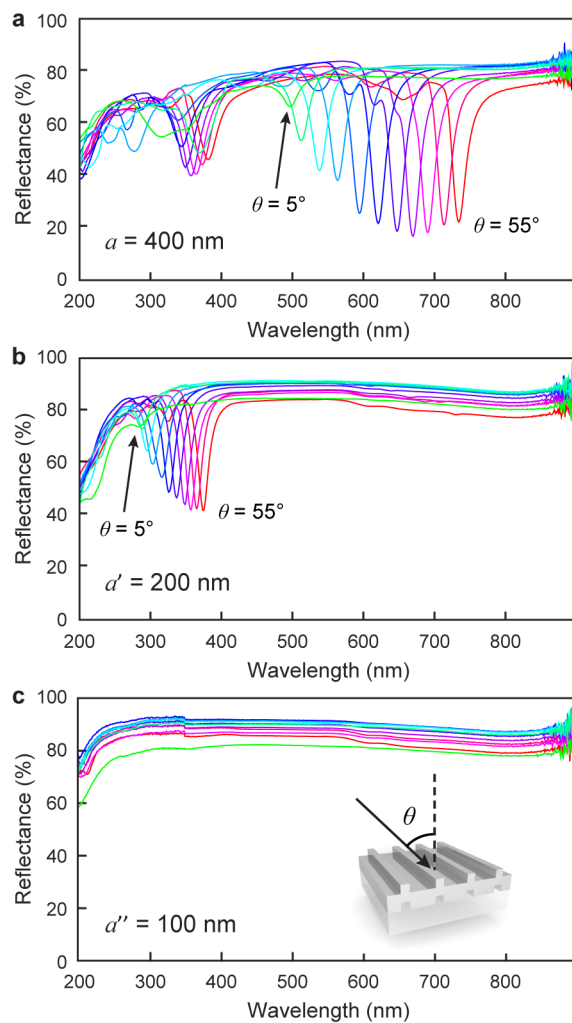


Figure 2.12. Plasmonic modes of Al line patterns. Reflectance spectra for periodicities of $a = 400$ nm (a), $a' = 200$ nm (b), and $a'' = 100$ nm (c). Spectra were collected from 5° to 55° in increments of 5° . Devices showed UV and visible modes with dispersive character based on incident angle.

they can be reused to produce plasmonic substrates by template stripping. Moreover, the Si templates can be used to create hard molds for nano-imprint lithography or PDMS stamps for soft nanolithography. Discrete features, such as posts and holes, can be created by two lithographic patterning steps of one-dimensional molds crossing at arbitrary angles. Therefore, our feature-density doubling approach offers

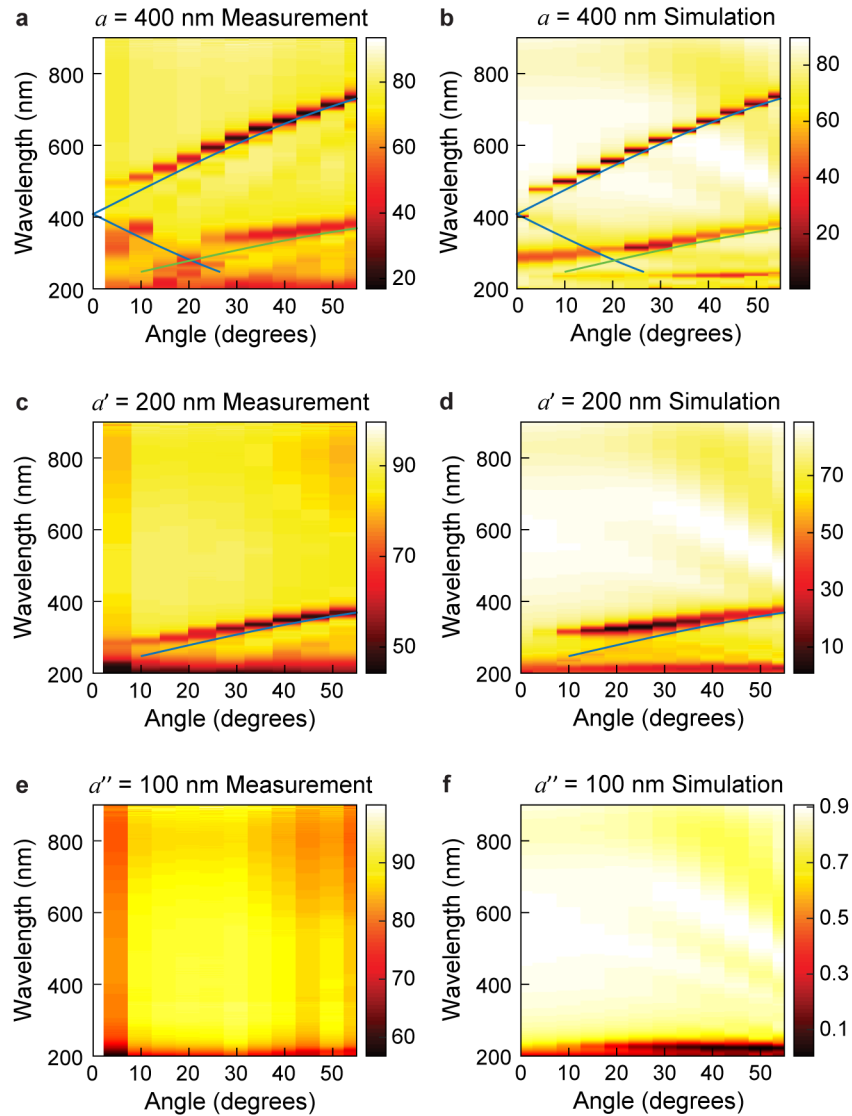


Figure 2.13. Dispersion diagrams for reflectance of Al devices. Spectra for $a = 400$ nm periodicity Al lines from (a) experimental measurement and (b) simulation. Spectra for $a' = 200$ nm periodicity Al lines from (c) measurement and (d) simulation. Spectra for $a'' = 100$ nm periodicity Al lines from (e) measurement and (f) simulation. The lines in the plot show analytical calculations of first order ($i = 1$) SPP modes in blue and second order ($i = 2$) SPP modes in green for the respective structures. Simulations were performed using finite-difference time-domain (FDTD) simulations in Lumerical with a plane wave light source and periodic boundary conditions using a broadband fixed-angle source technique (BFAST).

prospects in nanofabrication techniques beyond template stripping. For example, nanoparticle arrays with small spacings could show high-quality plasmonic modes⁹³ for applications like UV nanolasers.

2.6. Methods

2.6.1. Feature-Density Doubling of Si Lines

Si wafers were first coated with 5 nm of ALD alumina at a process temperature of 200°C using water and trimethylaluminum precursors. Alumina-coated wafers were then treated with MicroChem MCC Primer 80/20. Shipley 1805 photoresist was diluted with propylene glycol monomethyl ether acetate (PGMEA), spun on the wafers to thicknesses of 60–90 nm, and baked at 115°C for 2 minutes. PDMS masks for soft lithography were molded from Si line patterns²⁶ and used to perform solvent-assisted nanoscale embossing (SANE), where PDMS masks were first soaked in dimethylformamide (DMF) and then placed on resist-coated wafers to produce resist patterns inverse to those on the PDMS mask.² Residual resist was removed with a brief oxygen plasma treatment. We used a commercial wet-etchant (Transene Aluminum Etchant Type A) for controlled over-etching of ALD alumina heated to 50°C and stirred at 100 RPM. A thin (7-nm) Cr film was deposited by thermal evaporation, followed by resist liftoff using MicroChem Remover 1165. Si masked by Cr and alumina lines was dry-etched to form trenches by deep reactive ion etching (DRIE) using a co-flow of SF₆ and C₄F₈ process gases.^{98,99} Cr and alumina masks were removed from the Si patterns by wet-etching (Transene Al Etchant and Transene Cr Etchant).

2.6.2. Template Stripping of Al Arrays

Si pattern templates were treated for 5 seconds with a C₄F₈ plasma using a DRIE tool to form a few-nm conformal coating of fluoropolymer.³³ An optically thick layer of Al (120 nm) was deposited onto the coated Si templates by e-beam evaporation. Template stripping was performed using glass microscope slide substrates and optical adhesive (NOA 61, Norland Products Inc.) cured under a UV lamp for ~5 minutes.³⁰

2.6.3. UV-vis Measurements

Reflection measurements were performed using a Cary 5000 UV-vis spectrophotometer with DRA-2500 integrating sphere module and center-mounted sample holder. We used a 3-nm slit band width, 0.5-s integration time, and 1-nm data interval, 200–900 nm spectral range, and a square 1 cm x 1 cm spot size. To limit loss of reflected and scattered light, a circular (5-mm diameter) reflectance aperture was used to reduce the size of the integrating sphere entrance port. The aperture did not affect the spot size because the beam was focused at the sample and not at the aperture. Al line samples were aligned with 0° azimuthal angle (lines vertical), while light was incident in the horizontal plane. Spectra were collected from 5° to 55° incident angle in 5° increments.

CHAPTER 3

**Plasmonic Enhancement of Carbon Nanotube
Photoluminescence**

3.1. Introduction to Lattice Plasmon Modes

Lattice plasmons (also termed surface lattice resonances) are optical modes generated by the interaction of metal nanoparticles in an array structure within a uniform refractive index environment. Each individual nanoparticle supports a localized surface plasmon (LSP) resonance whose wavelength depends upon the nanoparticle's size, shape, material, and refractive index environment. Arranging the nanoparticles in a periodic array produces diffraction modes that are a function of lattice geometry and refractive index. A Fano-type resonance forms due to the interference between the LSP (continuum state) and diffraction mode (discrete state) in which the nanoparticles oscillate in phase with each other and cancel out scattering loss. This hybrid mode exhibits both plasmonic characteristics like high electromagnetic field intensities and nanoscale field confinement, as well as photonic properties like high quality factor. Lattice plasmons have therefore benefited applications for nanoscale lasing and emission enhancement that take advantage of cavities with high local density of optical states (LDOS). Carbon nanotubes display promising properties as nanoscale emitters that would become further valuable through plasmonic enhancement.

3.2. Carbon Nanotube Optical Properties

Conceptually, carbon nanotubes can be thought of as sheets of graphene rolled into cylinders (**Figure 3.1**). The nanotube chirality, identified by a set of (n, m) indices, defines the nanotube diameter and helicity (twist) in terms of graphene lattice vectors.^{101,102} The corresponding band structure, electrical properties, and optical properties of a carbon nanotube are also derived from its chirality, with some species demonstrating either semiconducting or metallic behavior.^{101–103} Critically, carbon nanotubes may form into bundles or even concentric multi-walled nanotubes, but they must be individualized (typically using a surfactant such as sodium dodecyl sulfate) into single-walled carbon nanotubes (SWNTs) in order to maintain their interesting optical properties.¹⁰⁴

Carbon nanotubes show an assortment of near-IR emission wavelengths, support continuous excitation and emission without blinking, and are robust against photo-bleaching.¹⁰³ These properties make carbon nanotubes an attractive emitter in comparison to organic dyes or quantum dots for applications

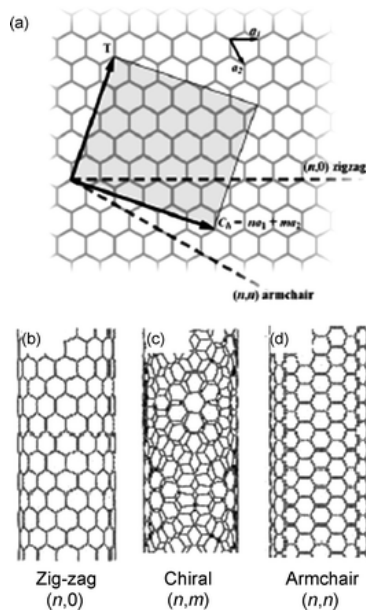


Figure 3.1. Structure of Carbon Nanotubes. (a) A schematic diagram showing how nanotubes can be visualized as sheets of graphene rolled along different directions. Different classes of nanotube chiralities are shown, including zig-zag (b), chiral (c), and armchair (d). Figure adapted from Zhang et al.¹²

such as bio-compatible sensors and telecommunications devices.^{105–107} However, low photoluminescence quantum efficiency $QE < 0.1\%$ has hindered optical applications of carbon nanotubes^{103,106,108,109} in comparison with some organic dyes with $QE > 90\%$.¹⁰⁶

Dimensions for carbon nanotubes range drastically from tens of nanometers to centimeters in length and from several angstroms to a few nanometers in diameter.¹¹⁰ For semiconducting carbon nanotubes, the band gap is inversely proportional to the tube diameter,^{101,102} corresponding to a range from 820 nm to over 1400 nm in emission wavelength.^{103,105,106} Carbon nanotube synthesis typically results in a polydisperse mixture of chiralities, but recent advances in scalable sorting methods allow for the separation of carbon nanotubes based on electronic type and diameter with high purity.^{105,111,112} This breakthrough allows for applications requiring specific electronic character (metallic or semiconducting) or specified emission wavelength.

Semiconducting SWNTs behave as one-dimensional semiconductors, creating sharp peaks in their density of states, called van Hove singularities,^{13,102} as shown in **Figure 3.2**. Excitonic optical transitions

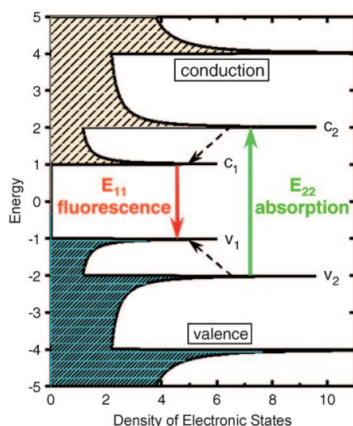


Figure 3.2. The density of states in a semiconducting SWNT shows van Hove singularities forming peaks in the valence and conduction bands at positions dependent on chirality. Photon absorption (green arrow) is followed by non-radiative decay within the valence band and within the conduction band (dashed arrows) to the band edges from which emission (red arrow) may occur. Reproduced from Bachilo et al.¹³

are identified as E_{ii} indicating transitions between the i^{th} valence band and i^{th} conduction band. The photoluminescence pathway in this system starts with photon absorption at the E_{22} transition, followed by non-radiative relaxation to the valence and conduction band edges where E_{11} photon emission may occur.^{13,106}

Fluorescence measurements on individualized SWNTs have shown decay lifetimes of roughly $\tau \approx 10$ ps in combination with low quantum efficiency ($QE \approx 1.7 \times 10^{-4}$).¹⁰⁹ This points to a relatively long radiative lifetime τ_{rad} on the order of 10 to 110 ns in comparison to organic molecule radiative lifetimes on the order of a few ns.^{109,113} Nonetheless, τ_{rad} is not long enough to suggest a weak radiative transition, but instead implies that fast decay of measured fluorescence results from a non-radiative relaxation mechanism with a much shorter lifetime τ_{nr} that rapidly quenches the emission.^{109,113} The origin of this non-radiative relaxation mechanism is unclear, but some point to recombination at defects, such as at the ends of the nanotubes.^{103,106,108,109} Utilizing the Purcell effect within an optical cavity may allow for faster emission, preventing many excitons from ever reaching a defect state, thereby leading to higher overall quantum efficiency.

In this chapter we show that the photoluminescence intensity of semiconducting single-walled carbon nanotubes can be enhanced coupling to lattice plasmons in a Au nanoparticle array. We performed photoluminescence mapping to establish target wavelengths for excitation and cavity-enhanced emission. Based on this information, we designed and fabricated nanoparticle optical resonators that showed high quality factor, high field enhancement, and excellent spectral overlap with the targeted nanotube emission peak. The carbon nanotube emission was enhanced by a factor of two when incorporated into the lattice plasmon cavity. Lifetime measurements showed little effect on the emission decay rate, and a few potential reasons for this are discussed.

3.3. Designing Optical Cavities to Target Nanotubes.

Optical cavities need to be designed based upon their intended applications so that resonant cavity modes match with their target wavelengths. Therefore, we first focused on the absorption and emission properties of the nanotubes. SG65 carbon nanotubes were dispersed in aqueous solution using ionic surfactant. Aggregates of bundled nanotubes were individualized further by sonication and centrifugation to separate the remaining bundles from the individualized nanotubes. The nanotubes were redispersed in ionic surfactant solutions for measuring the photoluminescent properties. We used a spectrofluorometer to create a photoluminescence map (**Figure 3.3**). The PL map shows emission intensity as a function of both excitation wavelength and emission wavelength, and both of these parameters depend upon the nanotube chirality. Because the nanotubes were unsorted, several chiralities of nanotube were present in the aqueous dispersion. We therefore observed several bright spots in our PL map with brighter intensity for more abundant species. The strongest emission arose at an excitation wavelength of 570 nm for an emission peak near 995 nm, and these optical properties matched the (6, 5) nanotube chirality values for E_{22} and E_{11} transitions, respectively. Nanotube sorting methods using density-gradient ultracentrifugation can help to isolate specific species to a large degree, but the more abundant species in the unsorted samples provide the highest yields after sorting. We therefore decided to target the (6,5) chirality for our studies of plasmonic interaction.

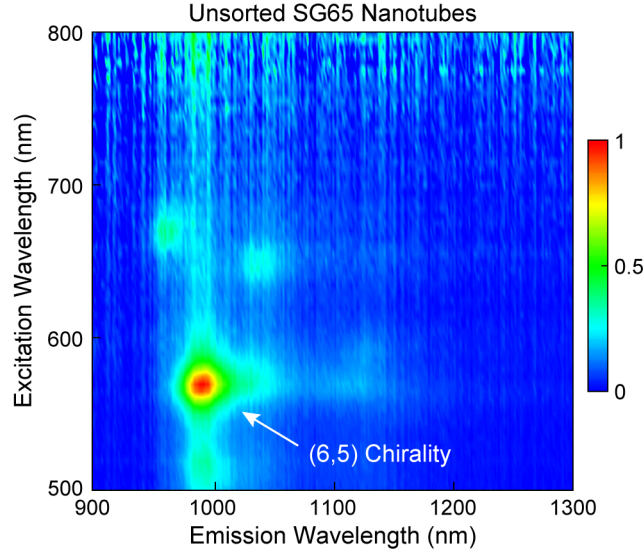


Figure 3.3. Photoluminescence map for carbon nanotubes. Unsorted solutions of carbon nanotubes showed several bright spots in their PL map corresponding to different chiralities of nanotubes. The brightest spot is attributed to (6, 5) chirality that emit near 995 nm with excited at 570 nm.

We designed our cavities to be resonant with the (6, 5) emission wavelength of 995 nm by tuning the lattice plasmon mode based upon refractive index n , array lattice spacing a , nanoparticle material, and nanoparticle diameter d (**Figure 3.4a**). Lattice plasmons always occur spectrally close to a diffraction mode, which in the simple case of square lattices, is determined based upon on array spacing a and refractive index n .

$$(3.1) \quad \lambda = na$$

We chose to use borosilicate glass and nanotubes dispersed in gelatin films as our dielectric materials, which set the refractive index at $n = 1.52$. Therefore, we calculated that a lattice spacing of $a = 650$ nm would produce a diffraction mode and associated lattice plasmon mode near our target of $\lambda = 995$ nm. The LSP mode used for coupling was dependent upon nanoparticle (nanodisk) material and diameter, with little effect from nanodisk height. Au was chosen for the nanoparticles because of it's strong plasmonic response at NIR wavelengths and chemical stability. Simulations were used to optimize the lattice mode

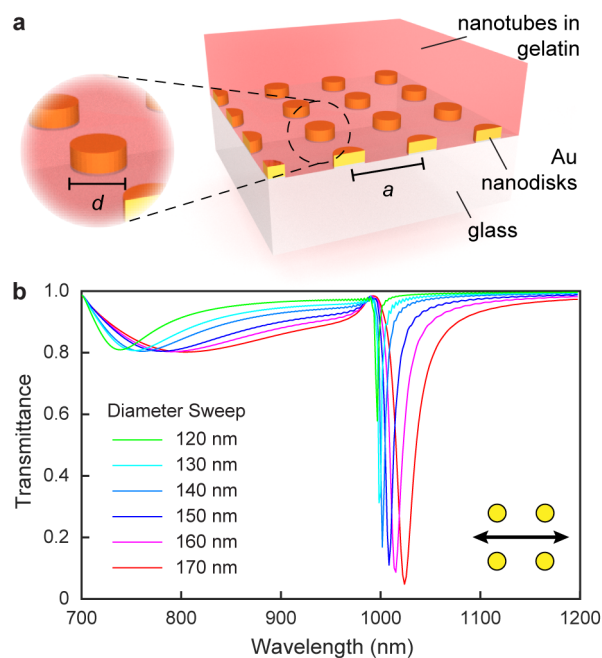


Figure 3.4. Tuning and optimization of lattice modes. (a) Scheme showing a Au nanodisks array on a glass substrate and embedded within a thin film of carbon nanotubes and gelatin. (b) Simulated transmission spectra for varying nanoparticle diameters to optimize the quality factor and peak intensity for the lattice mode near 1000 nm.

quality factor and intensity by sweeping the nanoparticle diameter while keeping the height fixed at $h = 50$ nm (**Figure 3.4b**). The simulated spectra showed broad dips from LSP modes between 700–1000 nm with sharp, narrow lattice plasmon mode dips between 1000–1030 nm. Smaller diameters showed a higher quality factor but a lower peak intensity. We found that diameter $d = 130$ to 140 nm offers a good balance in this tradeoff between quality factor and peak intensity.

The near-field mappings provided additional insight about the nature of these lattice plasmon modes (**Figure 3.5**). The optimized lattice mode ($n = 1.52$, $a = 650$ nm, $d = 140$ nm) showed electric field intensities in the nanoparticle hot spots 600 times higher than the background intensity from the excitation pulse (**Figure 3.5a**). These electromagnetic hot spots enhance light-matter interaction to assist with increased PL from nanotubes near the nanoparticles. A unique property of lattice plasmon modes is the formation of standing waves as seen in the bands of constant phase for all nanoparticles in the array (**Figure 3.5b**). This property arises from the nanoparticles all oscillating in phase with

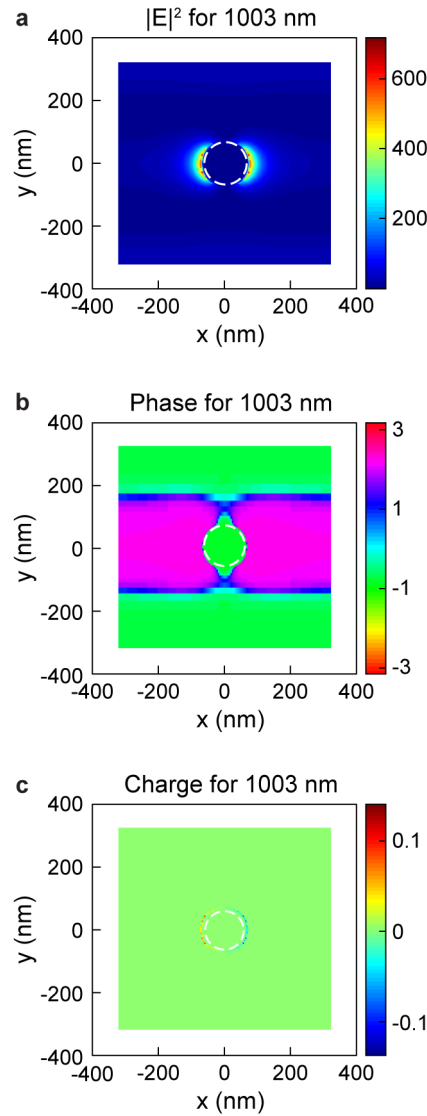


Figure 3.5. Lattice mode near-field properties. Mappings of electromagnetic field intensity (a), phase (b), and charge density distribution (c) for a lattice mode at 1003 nm. The light was incident at normal angle and polarized along the x -axis of the nanoparticle arrays. Nanoparticles are shown in white dotted line outlines.

each other, and occurs only for non-dispersive points (where group velocity $d\omega/dk = 0$) in the band structure diagram. The plasmonic oscillation of electrons sets upon non-uniform charge distributions on the surfaces of the nanoparticles. Mapping charge density shows that the lattice mode is linked to a

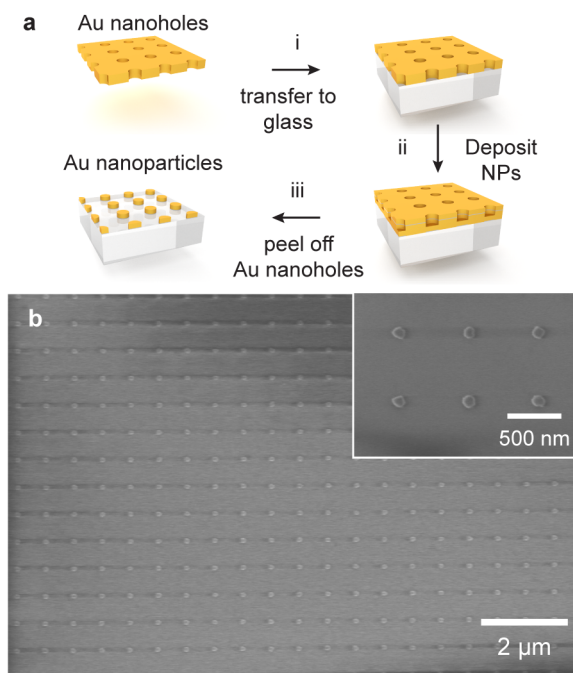


Figure 3.6. Fabrication of Au nanoparticle arrays. (a) A scheme showing the fabrication process for producing nanoparticle arrays on glass. (b) An SEM image showing the fabricated arrays of Au nanodisks with $a = 650$ nm periodicity and $d = 140$ nm diameter.

dipolar oscillation of the nanoparticles based upon the positively-charged and negatively-charged regions (**Figure 3.5c**).

3.4. Fabrication and Testing of Plasmonic Arrays

Au nanoparticle arrays with the optimized structure parameters were fabricated using parallel patterning on glass using the PEEL method²⁷ (**Figure 3.6a**). Briefly, soft lithography was used to produce Au films patterned with nanohole arrays covering 1-cm² areas on silicon. The Au hole array films were transferred onto the chosen substrate by floating on water. The Au holes array was used as a sacrificial physical deposition mask for depositing a thin (2-nm) Cr adhesion layer and Au nanoparticles using thermal evaporation. Finally the sacrificial Au film was lifted off with adhesive tape, leaving Au nanoparticles on glass. The fabricated structures showed round nanoparticles with dimension close to the targeted 140-nm diameter and 650-nm periodicity (**Figure 3.6b**).

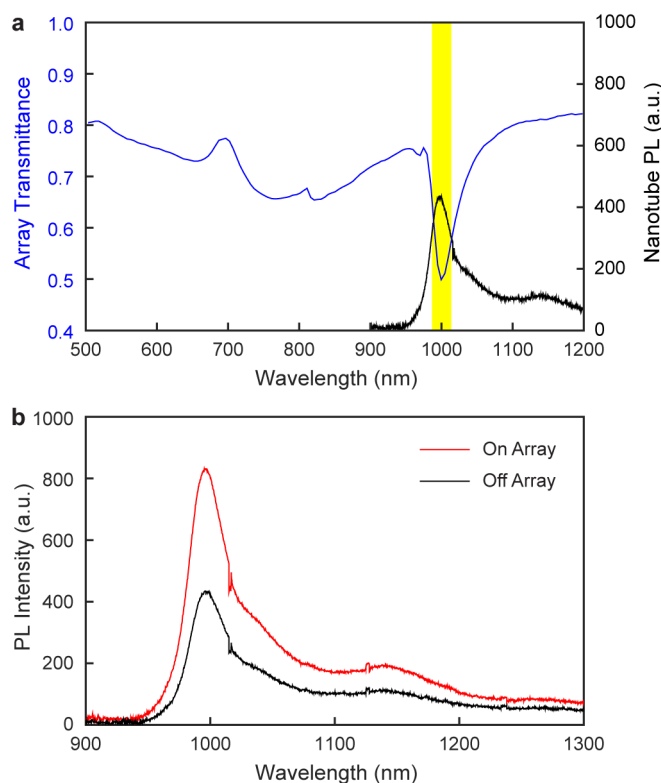


Figure 3.7. Optical properties of nanotubes with nanoparticle array. (a) The measured transmission spectrum for a Au NP array is shown with the emission spectrum for (6, 5) sorted carbon nanotubes. The lattice mode and emission peak show spectral overlap near 1000 nm. (b) PL spectra for a nanotube film comparing areas on the Au NP array against areas off the array show PL enhancement by a factor of two.

The array optical properties were characterized by measuring the transmission when index-matched using immersion oil ($n = 1.52$) and a UV-vis spectrophotometer. The transmission spectrum matched the simulated behavior from (Figure 3.4b) with a broad dip between 700–1000 nm from the individual nanoparticle LSP and a sharp dip near 1000 nm from the lattice plasmon mode (Figure 3.7a, blue curve). A small bump in the spectrum is seen near 800-nm due to the UV-vis detector changeover.

Samples of carbon nanotubes were sorted by density-gradient ultracentrifugation to increase the relative abundance of (6, 5) chirality nanotubes while removing the unwanted chiralities. The sorted nanotubes were pumped at their $E_{22} = 570$ nm transition in a spectrofluorometer to examine their refined emission spectrum (Figure 3.7a, black curve). Emission from the (6, 5) E_{11} transition at 995

nm dominated the PL spectrum, but a broad shoulder near 1150 nm from another nanotube chirality persisted even after the sorting process. Importantly, the measured lattice mode from the array and emission from the nanotubes showed excellent spectral overlap near 1000 nm (highlighted in yellow), which is critical for achieving cavity-enhanced fluorescence.

Gelatin powder was mixed into the sorted nanotube solutions and used to create thin films via blade-coating. The thin films covered large areas, including regions on the nanoparticle arrays and on bare glass substrate with uniform thickness. PL intensity was measured for film regions both on and off the array (**Figure 3.7b**, red and black curves, respectively), with the nanoparticle arrays showing an enhancement factor by a factor of two in comparison to bare glass. Lattice plasmon modes are dispersive such that the resonant wavelength depends on the angle of incident/emitted light. The PL was measured using a wide collection angle, so the enhancement covered a broad range of wavelengths. Since carbon nanotube fluorescence is usually studied in aqueous dispersion or for isolated structures in air, it is also worth noting that the fluorescent properties of nanotubes are preserved even when embedded in a solid gelatin matrix.

Cavity-enhanced emission is often characterized by an increase in the emission decay rate, or equivalently a decrease in the emission lifetime for the nanotubes. In order to test this mechanism, we performed measurements of nanotube emission decay dynamics using time-correlated single-photon counting spectroscopy (**Figure 3.8a**). The nanotubes were excited at their E_{22} transition using an optical parametric amplifier that provided laser pumping tuned to 570 nm, and the emission was monitored by a streak camera that provided both spectrally and temporally resolved information about the decay dynamics. The data was binned by wavelength to select the E_{11} emission band, and the curves were plotted against time. Dynamics data was collected for nanotube films both on and off the plasmonic array (**Figure 3.8b**, red and black curves, respectively), and the curves were each fitted with an exponential decay function to determine lifetime. The on-array measurement showed a lifetime of 5.2 ± 0.1 ps versus 5.3 ± 0.3 ps off the array, so no statistical difference in lifetime was observed.

There are a couple potential reasons we observed no detectable change in lifetime associated with the enhanced PL of the nanotubes coupled to the NP array system. First, the PL signal may be dominated

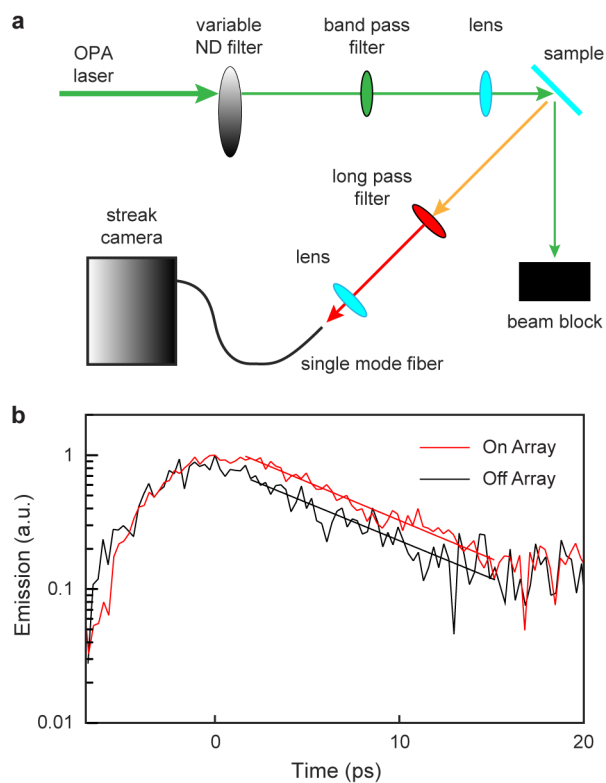


Figure 3.8. Lifetime measurements of nanotube emission. (a) A scheme for lifetime measurements using a streak camera to perform time-correlated single-photon counting spectroscopy. (b) Emission decay plots for nanotube films on nanoparticle arrays on and off nanoparticle arrays.

by nanotubes that are outside the plasmonic hotspots and therefore cannot couple to the plasmonic cavity mode. In this case the large background fluorescence from uncoupled nanotubes may be obscuring the signal of coupled nanotubes. Remedying this problem is tricky. Ideally we would want to localize the nanotubes within tens of nanometers from the nanoparticles, using an extremely thin gelatin and nanotube film to increase the fraction of nanotubes in the plasmonic hot spots. However, this reduces the overall intensity of the PL signal to unusable levels since the total number of nanotubes is reduced and the nanotubes show relatively weak PL due to their low quantum efficiency. Therefore, we would want to try using higher concentrations of nanotubes with lower concentrations of gelatin applied in thinner films to our arrays. Second, the PL enhancement may be partially arising from plasmon-enhanced absorption. Our nanoparticle arrays showed some optical activity near the 570 nm E_{22} absorption band, which could

improve the excitation efficiency for the nanotubes. Increased absorption, would in turn lead to higher PL intensity without necessarily modifying the emission decay dynamics.

3.5. Summary

In summary, we discussed the methodology for designing and structuring Au nanoparticle arrays to support lattice plasmon modes that targeted emission enhancement in carbon nanotubes. We demonstrated good spectral overlap of our optical cavity lattice plasmon mode with the nanotube emission wavelength. These cavities induced a two-fold enhancement of (6, 5) carbon nanotube PL intensity over a broad wavelength range. However, the plasmonic arrays had no effect on the emission decay lifetime, which suggests that the enhancement may be toward stronger nanotube enhancement or a large background of PL from nanotubes outside the plasmonic hotspots. In the following chapter we will discuss strategies for remedying this problem of spatial overlap by studying two dimensional semiconductor nanomaterials.

3.6. Methods

3.6.1. Carbon Nanotube Preparation

The nanotube dispersion and films were prepared by Yu Jin Shin from Prof. Mark Hersam's research group. Commercially available, as-synthesized carbon nanotubes (CoMoCat SG65 carbon nanotubes: Sigma Aldrich 704148) were dispersed in aqueous solutions of 2% w/v sodium deoxycholate (SDC) with an initial nanotube concentration of 1 mg/mL. The negatively-charged SDC surfactant helped to disperse individualized nanotubes within the solution by adsorbing onto the nanotube walls. The nanotubes solutions were then sonicated and centrifuged to separate out bundles of nanotubes and create a more individualized dispersion of nanotubes. After centrifugation, the nanotubes were redispersed in 1% w/v sodium dodecyl sulfate (SDS) before adding gelatin (10% w/v). These nanotube and gelatin solutions were then applied to the nanoparticle array samples using blade-coating to form films of uniform thickness.

3.6.2. Photoluminescence Spectroscopy Measurements

PL measurements were taken using a Horiba Fluorolog-3 spectrofluorometer with integration times of 60 s. Excitation was performed using a broad spectrum lamp with a spectrometer to select a 570-nm pump wavelength. Emission was detected through a front-facing port leading to an InGaAs photodetector cooled with liquid nitrogen. The excitation and detection grating spectrometers both used 10-nm band slit widths.

3.6.3. Band Structure Mapping

The band structures are mapped using a transmission spectrometer setup with the sample mounted on a motor-controlled rotation-axis stage. White light from a lamp is focused to a beam and directed through the sample. The transmitted light is coupled into an optical fiber and directed to a grating spectrometer with a CCD camera. The angle of the samples is rotated in increments of 1° and a transmission spectrum is collected at each angle. The data are then plotted as either individual spectra or compiled into dispersion diagrams showing transmission intensity as a function of wavelength (related to frequency or energy) and angle (related to the in-plane wavevector) to observe the optical band structure.

3.6.4. Time-correlated Single-photon Counting Spectroscopy

Emission decay dynamics were measured using time-correlated single-photon counting spectroscopy (TC-SPC) at Argonne National Laboratory at the Center for Nanoscale Materials in the lab of Prof. Richard Schaller. An optical parametric amplifier provided pulsed laser emission at 570 nm using 35-fs pulses with a 2 kHz pulse repetition rate. Intensity was controlled with a variable neutral density filter, and unwanted laser modes were eliminated using a band-pass filter. The beam was focused with a lens to a spot of 1–2 mm on the sample. Emission at normal angle was sent through a long-pass filter to remove the pump laser signal and collected by a fiber that was coupled into a streak camera. The streak camera generated intensity mappings as a function of time and wavelength. The streak camera was locked to the frequency of the laser rep. rate, so we could integrate over 441k laser pulses to collect a usable signal level. Nanotube PL data was binned by wavelength from 940–1040 nm to plot emission intensity as a

function of time, and the curves were fit with exponential decay functions to determine the decay lifetime. The instrument response time was found to be 3 ps by measuring the instrument decay dynamics with the 35-fs OPA pulses.

3.6.5. Finite-Difference Time-Domain Simulations

Simulations were performed using Lumerical, a commercially available FDTD software. The source was injected along the z-direction (normal to the nanoparticle array) with polarization in the x-direction. A single unit cell was constructed using antisymmetric and symmetric boundary conditions for the x-boundary and y-boundary, respectively. The z-boundary was set to use perfectly match layer (PML conditions). A 4-nm mesh was created for the Au nanodisk (Au material optical constants data from Johnson and Christy¹¹⁴). The background index was set to 1.52 to represent the glass substrate and gelatin superstrate. Near-field monitors were placed in the plane of the nanoparticles, and the transmission monitor was placed opposite the light source.

3.6.6. Fabrication of Au Nanoparticle Arrays

Solvent-assisted nanoscale embossing was used to pattern photoresist posts on silicon.² Cr deposition (thermal evaporation) and photoresist lift-off created Cr hole arrays that served as a hard mask for dry-etching silicon pits using deep-reactive ion etching (SF_6 with C_4F_8 plasma). Au was deposited onto the Cr/Si hole arrays to create a Au hole array mask. Cr wet etching (Transene Cr etchant) released the Au mask which was then transferred onto a borosilicate glass substrate by floating the Au hole array film on water. The Au holes were used as a physical deposition mask for depositing a 2-nm Cr adhesion layer and 50-nm thick Au nanoparticles. Finally, the sacrificial Au hole array mask was removed with adhesive tape, leaving only the Au nanoparticles on glass.

CHAPTER 4

Amplified Light-Matter Interactions in Phosphorene



Figure 4.1. Phosphorene chemical structure. A schematic diagram of the chemical structure of phosphorene showing a layered composed of two dimensional sheets of phosphorus atoms with strong in-plane bonding. The layers have a corrugated structure that creates anisotropic properties. Figure adapted from Bagheri et al.¹⁴

4.1. Introduction to Two-Dimensional Semiconductor Nanomaterials

Two-dimensional nanomaterials are a broad class of atomically-layered substances with strong in-plane bonding and weak inter-layer interactions that allow for exfoliation of single-layer or few-layer sheets. Unique optical and electrical properties arise out of confinement in one dimension, with graphene, transition metal dichalcogenides, and hexagonal boron-nitride exhibiting exhibiting metallic, semiconducting, and insulating behavior, respectively.¹¹⁵ Furthermore, their optical absorption bands span the UV-vis-NIR spectrum, with promising applications in electronics, displays, and telecommunications.¹¹⁵

Black phosphorus (BP) or phosphorene is a layered material composed of atomic sheets of phosphorus with a corrugation (**Figure 4.1**) that generates anisotropic optical, electrical, and thermal properties.^{116–118} This characteristic in combination with near-IR optical activity and high carrier mobility make BP an interesting candidate for optoelectronic devices with polarization-dependent responses. BP has a direct band gap that is tunable from 0.3 eV in bulk form up to 2.0 eV in monolayer form, depending upon how many layers thick the sample is.¹¹⁷ The tunable optical properties of BP then hinge upon finding ways to generate monolayer or few-layer flakes of BP. One powerful method for scalable production of other two-dimensional materials like graphene and transition metal dichalcogenides is liquid-phase exfoliation of bulk crystals to isolate few-layer flakes.¹¹⁹ While these methods commonly include sonication in water and surfactants to disperse the flakes, few-layer BP oxidizes readily, so anhydrous solvents or deoxygenated water must be used to prevent chemical degradation of this material.¹¹⁸ The resulting aqueous

dispersion of nanotubes show characteristic Raman shift peaks and weak PL at 910 nm attributed to monolayer BP.¹¹⁸

In this chapter, we examine the use of lattice plasmon optical cavities for enhancing the optical activity of few-layer BP. We used the choice of cavity materials to change the refractive index environment around consistently structured Au NP arrays in order to tune the lattice mode to the emission wavelength of monolayer BP. The PL intensity and Raman intensity of BP flakes was examined both on and off the nanoparticle arrays to test for plasmonic cavity effects. We found weak enhancement of both the Raman signal and PL intensity for flakes of BP on the array. Using the Raman intensity to account for the amount of BP in a flake, we saw normalized PL intensity increased by a factor of two.

4.2. Targeting Phosphorene Emission with Lattice Plasmons

Au nanoparticle arrays with periodicity $a = 650$ nm, diameter $d = 140$ nm, and height $h = 50$ nm were fabricated on quartz (**Figure 4.2a**) and later coated with polymethyl methacrylate (PMMA). While the array dimensions were identical to the NP arrays in **Figure 3.6b**, the change in substrate and superstrate materials created a lower refractive index environment for quartz/PMMA ($n = 1.41$) than for borosilicate glass/gelatin ($n = 1.52$). This alteration shifted the lattice plasmon mode to 935 nm (**Figure 4.2b**), providing good spectral overlap with the broad emission peak at 910 nm reported for BP. These results were verified using simulations of these Au NP arrays structures with a non-dispersive background index of $n = 1.41$ and obtained a similar transmission spectrum. Slight differences in spectral shape, particularly the wavelength for the second-order diffraction peak near 650 nm, are attributed to disagreements for the dispersive refractive index of the experimental materials (quartz and PMMA) versus the non-dispersive simulated index. Furthermore, rounding of the blue shoulder on the lattice mode, which should be sharp due to the Fano lineshape, is likely due to slight refractive index mismatch for quartz and PMMA that hinders the first-order diffraction mode. Even so, the experimentally measured lattice mode shows high quality factor ($Q = 125$).

Transmission measurements at off-normal angle were collected for these nanoparticle arrays using transverse magnetic (TM) polarization. Dispersion diagrams were plotted as a function of angle and

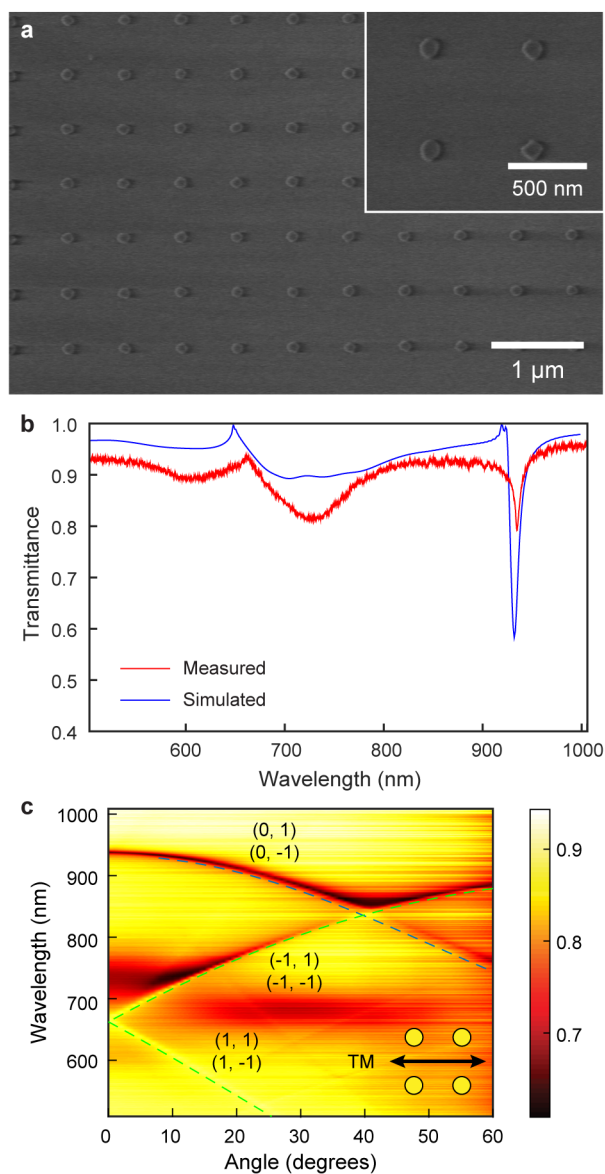


Figure 4.2. Nanoparticle arrays for phosphorene enhancement. (a) SEM images depicting Au nanoparticle arrays on a quartz substrate. (b) Measured (red) and simulated (blue) spectra for normal angle transmission with a PMMA index-matching layer. (c) A dispersion diagram showing the optical band structure of the nanoparticle arrays under TM polarization with Bragg modes traced in dotted lines.

wavelength to examine the optical band structure (**Figure 4.2c**). First-order Bragg modes are plotted in blue dotted lines, and second-order modes in green. The lattice plasmon mode is shown to couple to the

first-order (0, 1) and (0, -1) Bragg modes and therefore have zero group velocity ($d\omega/dk = 0$) at normal incident angle ($\theta = 0$).

4.3. Near-field Properties of Lattice Modes

The FDTD simulations were also used to map the near-field profiles for the Au NP arrays for injection of light at normal angle (**Figure 4.3b**). These plots showed qualitatively similar behavior to the lattice plasmons in (**Figure 3.5**). The electric field intensity showed plasmonic hot spots that concentrated the light by a factor of more than 600 in comparison to the injected light intensity. The phase plot revealed bands of constant phase indicating that the nanoparticles were all oscillating in phase with each other (**Figure 4.3b**). This property was characteristic of standing waves (zero group velocity) and agreed with the zero group velocity (slope = 0) for the lattice mode at normal angle in (**Figure 4.2c**), which is important for achieving a high local density of optical states for cavity-enhanced emission. The charge density mapping again showed dipolar character for the lattice plasmon mode (**Figure 4.3c**) with the charge bound tightly on the surface of the nanoparticles.

4.4. Integrating Nanoparticle Arrays with Phosphorene

The far-field and near-field characterization of these lattice plasmon cavities displayed ideal properties for enhancing the optical properties of monolayer phosphorene with emission near 910 nm, so the two materials were integrated by phosphorene transfer (**Figure 4.4**). Black phosphorus crystals underwent liquid phase exfoliation in deoxygenated water to separate the material into few-layer phosphorene containing monolayer, bi-layer, and tri-layer flakes. The flakes were then vacuum-filtered with an amorphous aluminum oxide membrane to remove the surfactant and water. The dry phosphorene film was stamped with PDMS to pick up patches of few-layer phosphorene and transferred to the Au nanoparticle arrays. Index-matching was performed by spin-coating a layer of PMMA for an average index of $n = 1.41$ around the nanoparticles.

The completed structures were characterized using a Raman microscope to simultaneously collect PL spectra and Raman spectra of individual flakes of phosphorene (**Figure 4.5**). Representative flakes

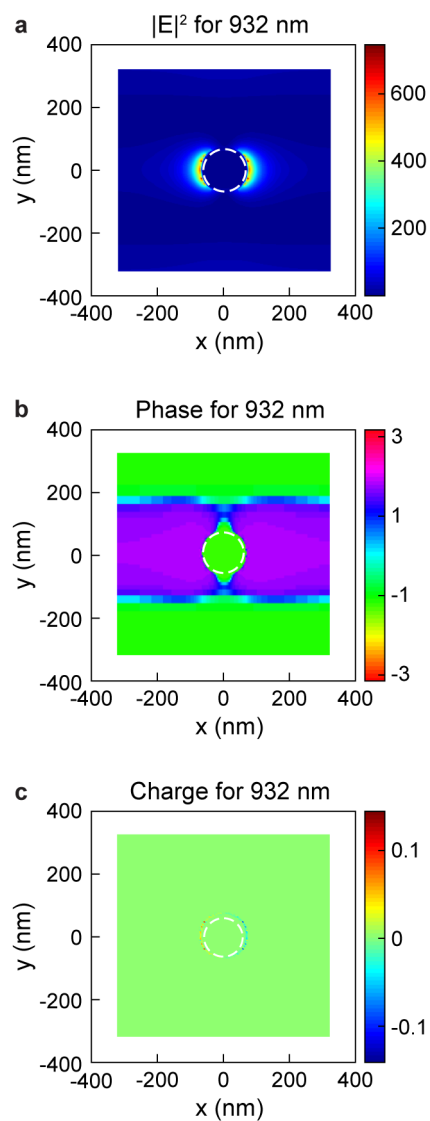


Figure 4.3. Simulated near-field mappings for Au NP arrays. Plots of electric field intensity (a), phase (b), and charge density distribution (c) for a lattice plasmon mode at 932 nm. The simulation uses light injected at normal angle (z -direction) with polarization along the x -axis. Dotted white lines outline the Au nanoparticle positions.

both on and off the array area were chosen for the plots, which used 30 second integration times for the PL measurements and 60 second integration times for the Raman measurements and excitation using a 532-nm continuous wave laser. Spectra were fit with Voigt functions to match the expected spectral line

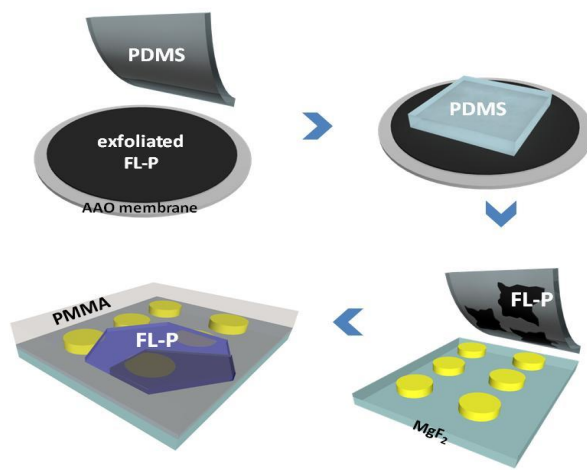


Figure 4.4. Transfer of phosphorene. Exfoliated few-layer phosphorene was filtered using an amorphous aluminum oxide membrane. The dried film was stamped with PDMS to pick up patches of phosphorene film that are transferred to the Au nanoparticle arrays on a glass or MgF_2 substrate. Index-matching was performed by spin-coating PMMA. Image courtesy of Dr. Yu Jin Shin.

shapes and to reduce the noise level. The Flakes on the array generally showed a higher PL intensity than flakes off the array (**Figure 4.5a–b**). Similar trends of higher signal on the nanoparticle arrays were observed for Raman intensity for the three peaks corresponding to the A_1^g (pink), B_{2g} (green), and A_2^g (blue) vibrational modes. Importantly, the ratio of $A_1^g/A_2^g < 0.6$ indicates that the phosphorene has not oxidized in either case.

Because variations in phosphorene flake size can cause changes in the PL intensity independent of cavity effects, the Raman intensity was used to normalize the PL spectra. The A_1^g was chosen for this task because it was the only of the three modes to arise from out of plane vibrations. The normalized PL spectra showed that the nanoparticle array created a two-fold enhancement of the PL (**Figure 4.6**). The actual PL enhancement factor is likely higher than the $\times 2$ value because the plasmonic array likely also amplifies the Raman shifts through a common phenomenon of surface enhanced Raman scattering (SERS). The plasmonic nanoparticles concentrates the incoming lasing light, thereby increasing light-matter interactions like Raman scattering. Therefore, equivalently sized flakes of phosphorene may show

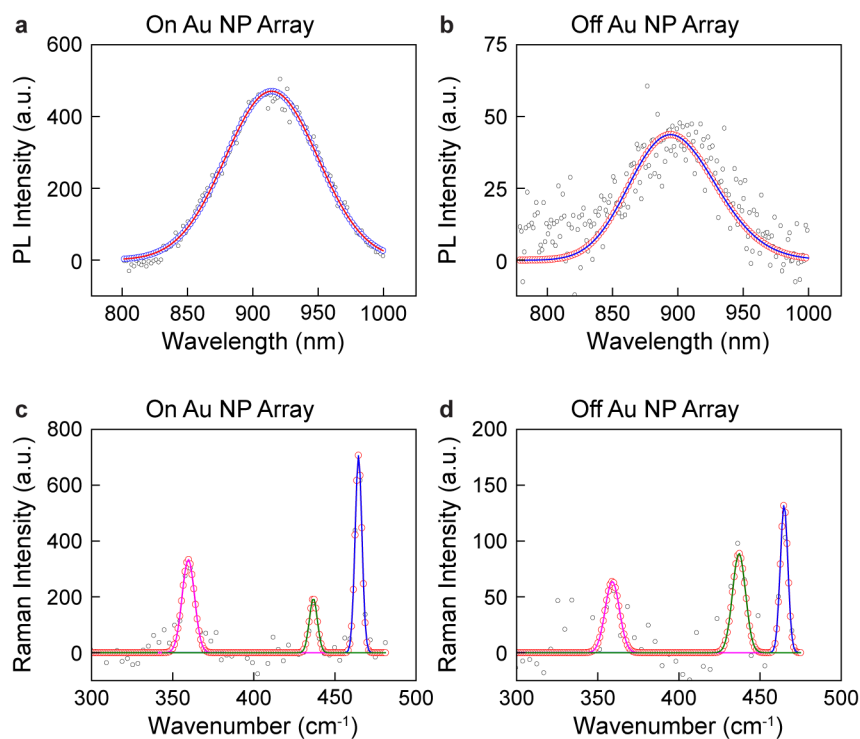


Figure 4.5. Optical properties of few-layer phosphorene. (a) and (b) PL spectra for representative flakes of few-layer phosphorene on and off of a Au NP array showing emission near 910 nm. (c) and (d) Raman shift spectra for the same flakes on and off array, showing three vibrational modes: A_1^g (pink), B_{2g} (green), and A_2^g (blue).

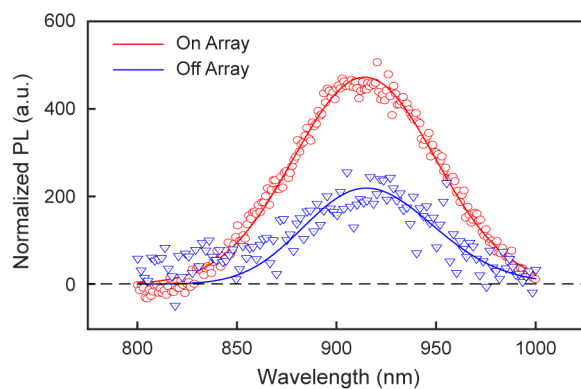


Figure 4.6. Normalized photoluminescence spectra. Raman intensity is used as a normalization reference to scale the intensities of the PL spectra for monolayer phosphorene on and off of the nanoparticle array.

higher Raman signal when placed in a plasmonic cavity. Controlling and quantifying this confounding effect was challenging given our samples and measurement system.

One idea for comparing the PL intensity on and off the array was to normalize the monolayer PL peak using the bilayer PL peak. Since cavity-enhanced emission depends on spectral overlap, the bilayer emission at 1200 nm should be sufficiently separated in wavelength to avoid any cavity effects. However, this wavelength is not within the spectral range of the detector on the available Raman system, necessitating a Raman microscopy setup equipped with both a NIR detector and visible detector with capability to switch back and forth for successive measurements of both emission peaks. Furthermore, the PL signal of the bilayer phosphorene prepared via this method showed an intensity two orders of magnitude lower than the monolayer peak.¹¹⁸ Therefore, integration times of roughly an hour would be required to measure the bilayer emission intensity (based on the 30 s integration time for the monolayer peak).

A second reason the comparison of flakes on and off the array was challenging, is that we had no information regarding the alignment of the phosphorene corrugation relative to the laser orientation and plasmonic lattice. The phosphorene optical properties, including Raman intensity, are highly polarization dependent and the flakes are oriented randomly. Similarly, we have no control over the placement of the flakes, so the flakes likely had varying degrees of spatial overlap with the plasmonic hot spots. Both of these factors add variability to the PL and Raman measurements that is difficult to eliminate when using flake transfer via stamping. To improve upon these limitation, it may be worthwhile to investigate other methods of integrating phosphorene into plasmonic cavities that will provide more uniform coverage and consistent crystal orientation.

4.5. Materials Selection for Improving Lattice Mode Overlap and Quality

Different dielectric materials were also explored for the array substrate and superstrate (**Figure 4.7**). Quartz substrates were examined in combination with PMMA or PDMS applied by spin-coating (**Figure 4.7a**). The two showed similar spectral behavior but the baseline for PDMS was much lower because scattering from the non-smooth PDMS film cause some loss of transmitted light at all wavelengths.

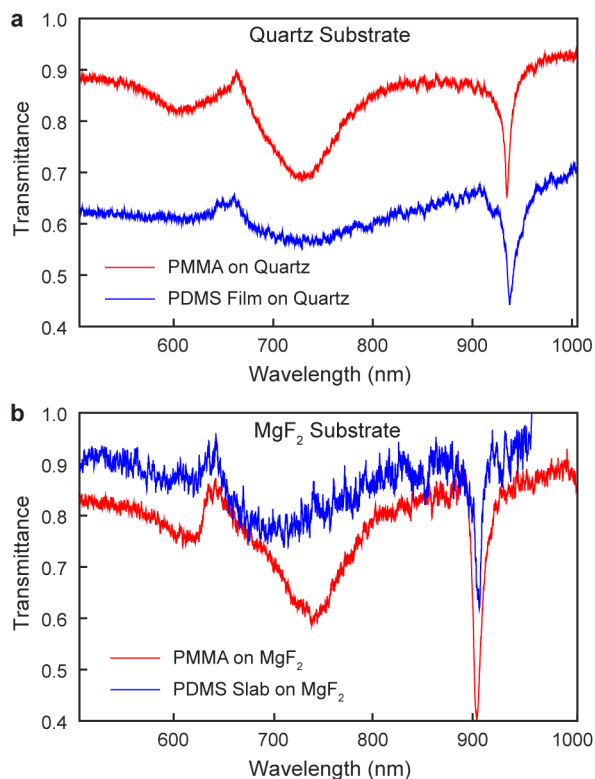


Figure 4.7. Lattice Modes in Different Materials Systems. (a) Quartz and (b) MgF₂ substrates were used in combination with PMMA and PMDS superstrates to investigate effects on lattice mode wavelength and linewidth.

Magnesium fluoride (MgF₂) was explored as a low index substrate ($n = 1.38$) in an attempt to shift the lattice mode to bluer wavelengths for better spectral overlap with the phosphorene emission peak(**Figure 4.7b**). In this case PMMA was applied by spin-coating, but PDMS was applied as a cured solid slab (roughly 2-mm thick) placed in conformal contact with the array. The MgF₂ with PDMS slab provided good index matching and a fairly uniform refractive index environment, which indicated the PDMS conformed to the topography of the array despite the presence of nanoparticles with 50-nm height. Furthermore, the lattice mode had a narrower linewidth with quality factor improved to $Q = 150$ for this combination of materials. This setup therefore shows promise for the application of phosphorene because it both improves the spectral overlap of the lattice plasmon and PL peaks and also allows for simple transfer of the phosphorene. In this case, the PDMS slab used for stamping the phosphorene flakes can

be placed on the array for both transfer and index matching for direct optical characterization. PL and Raman measurements were carried out using the MgF_2 with PDMS platform, but it unfortunately did not improve upon the results obtained with quartz and PMMA dielectric materials.

4.6. Summary

Nanocavity arrays were designed and fabricated for the enhancement of emission from few-layer phosphorene. Flakes of few-layer phosphorene were incorporated into the optical cavities and their optical responses were compared with flakes outside the cavities. We observed on average the plasmonic modes produced enhancement of both photoluminescence and Raman signal. We tested new materials for lattice plasmon systems that provided compatibility with different refractive index environments with similar levels of phosphorene enhancement. Nevertheless, this demonstration of lattice plasmon systems using a range of substrate and superstrate materials for index-matching provides greater versatility in designing optical nanocavities.

4.7. Methods

4.7.1. Preparation of Few-layer Phosphorene

Phosphorene preparation was performed by Jooheon Kang and Yu Jin Shin from the Hersam Group using their previously published procedure.¹¹⁸ Bulk crystals of black phosphorus (Smart Elements) underwent liquid phase exfoliation in a conical plastic tube filled with deoxygenated water with 2% (w/v) of sodium dodecyl sulfate surfactant to help with dispersion and an initial BP concentration of 1 mg/mL. The tube was sealed with parafilm and purged with Ar gas to minimize exposure to oxygen. The sample is tip-sonicated at 70 W for 1 hour in an ice bath and then the dispersion is centrifuged at 7500 rpm for 2 hours to crash out any flakes thicker than a few nm. The supernatant is then collected, centrifuged again at 14000 rpm, and re-dispersed in deoxygenated water. The flakes were then vacuum filtered with an amorphous aluminum oxide membrane (100-nm pore size) to remove the surfactant by rinsing with deoxygenated water. The dry films were stamped with pieces of cured PDMS (Sylgard 184) and then stamped onto the nanoparticle arrays, followed immediately by spin-coating. PMMA (MicroChem 950

PMMA A4) was applied at 500 rpm for 10 s followed by 2000 rpm at 45 s and then heated at 180° C for 30 s.

4.7.2. Raman Microscopy Measurements

Raman spectra and PL spectra were both measured using a Horiba LabRAM HR Evolution system with 532-nm continuous wave laser for excitation. These microscopy measurements used 10% power intensities, 30 s integration times for PL, and 60 s integration times for Raman signal.

4.7.3. Band Structure Mapping

The band structures are mapped using a transmission spectrometer setup with the sample mounted on a motor-controlled rotation-axis stage. White light from a lamp is focused to a beam and directed through the sample. The transmitted light is coupled into an optical fiber and directed to a grating spectrometer with a CCD camera. The angle of the samples is rotations in increments of 1° and a transmission spectrum is collected at each angle. The data are then plotted as either individual spectra or compiled into dispersion diagrams showing transmission intensity as a function of wavelength (related to frequency or energy) and angle (related to the in-plane wavevector) to observe the optical band structure.

CHAPTER 5

Polarization Dependent Lasing Behavior in Low-Symmetry Nanocavity Arrays

Referenced work: M. P. Knudson, R. Li, W. Wang, D. Wang, R. Schaller, and T. W. Odom, "Polarization Dependent Lasing Behavior in Low-Symmetry Nanocavity Arrays." [In Preparation]

5.1. Introduction to Symmetry Effects in Photonic Systems

The spatial symmetry of photonic devices is a key factor in defining optical properties, including band structure, mode degeneracy, localization of enhanced electric fields, and mode polarization. Several types of optical systems offer examples where symmetry has been broken or manipulated to introduce new and interesting optical phenomena. Collections of metal nanoparticles may be arranged into asymmetric clusters to produce chiral interactions with circularly polarized light.^{120,121} Perturbations to resonator unit geometry allows dark modes to couple to bright modes for far-field radiation.^{122,123} Quasicrystals, while lacking translational symmetry, take advantage of high orders of rotational symmetry to exhibit rotationally invariant band structures.^{124–127} Lastly, metal films patterned with rhombohedral lattices produce tunable, broadband plasmonic responses as a result of breaking mode degeneracy.¹²⁸ While several photonic systems benefit from symmetry effects, this concept has not been investigated with lattice plasmons: optical resonances in metal nanoparticle arrays that follow Bragg modes according to lattice geometry.^{7,129,130}

The high quality factors of lattice plasmons combined with their ability to concentrate light fields within nanoscopic hot spots has enabled their application toward a wide range of enhanced fluorescence studies^{38,39,131–133} and lasing applications.^{9–11,134} These previous studies primarily focused on square and hexagonal lattices of circular nanoparticles that allowed for simple fabrication methods.^{8,83,93} Plasmonic arrays of circular nanoparticles have been tested with a couple of more complicated honeycomb and Lieb crystal structures. The unit cells of these patterns contain multiple nanoparticles, but the overall band structures reflected their underlying hexagonal and square lattices, respectively.¹³⁵ Other examples of reduced symmetry in lattice plasmon cavities implement nanoparticle patches with finite dimensions to break the symmetry of infinite arrays for unique lasing behavior. Dark modes bound in infinite nanoparticle arrays are then able to couple to the far-field lasing due to edge effects in the patches.¹³⁴ In a second case, hierarchical arrays of nanoparticle patches produced superlattice plasmons supporting polarization-based switching between multi-mode and single-mode lasing.⁹

Despite these advances, breaking symmetry through changes in nanoparticle shape and lattice angle (defined by the angle between basis vectors) has not been examined and promises to provide insight

regarding fundamental properties of lattice plasmon lasers. Fabrication capabilities represent a major challenge in investigating new symmetries of lattices and nanoparticle shapes. While other array geometries are possible using electron-beam lithography, this writing technique does not scale well to large areas. Therefore, new fabrication procedures are needed to access anisotropic nanoparticle shapes and a broader range of lattice geometries in order to uncover the effects of symmetry in lattice plasmon lasing systems.

Here we show a new fabrication process using scalable lithography methods to produce low-symmetry nanoparticle arrays that provide a unique platform for revealing the interaction between lattice plasmon lasing modes. Our fabrication process produced infinite arrays of rhombus-shaped plasmonic nanoparticles arranged in a rhombohedral lattice. We found that the anisotropic nanoparticles could be used to engineer the electromagnetic near-fields of lattice plasmon modes and laser emission. By examining the lasing dynamics under different pump polarizations, we discovered that energy transfer between excitons and plasmons is faster when their polarizations are aligned, leading to shorter lasing rise time and decay lifetime. Furthermore, aluminum nanoparticles used in our platform allowed for shorter wavelengths of lattice plasmon lasing than previously demonstrated with gold and silver nanoparticles.

5.2. Fabrication of Low-Symmetry Nanoparticle Arrays

Al nanoparticle arrays were fabricated on quartz slides by deposition through sacrificial Au hole array masks followed by liftoff of the Au masks and Al films (**Figure 5.1a**). We designed a new, scalable method to pattern the hole array masks involving solvent assisted nanoscale embossing. Briefly, polymer resist lines were embossed on Si using elastomeric (PDMS) stamps, followed by Cr deposition and resist liftoff to produce an array of Cr lines. The process was repeated with the stamp rotated at a chosen angle ψ to create a second set of intersecting lines, producing a two-dimensional array of Cr holes. The Cr provided a mask for etching pits in the Si substrate through DRIE, followed by Au deposition. Finally, the Au hole array films (**Figure 5.1b**) were transferred to quartz substrates for Al nanoparticle deposition. This fabrication process offers the advantage of rhombus-shaped nanoparticles arranged in rhombohedral arrays of chosen lattice angles to an accuracy of $\pm 3^\circ$ (**Figure 5.1c**).

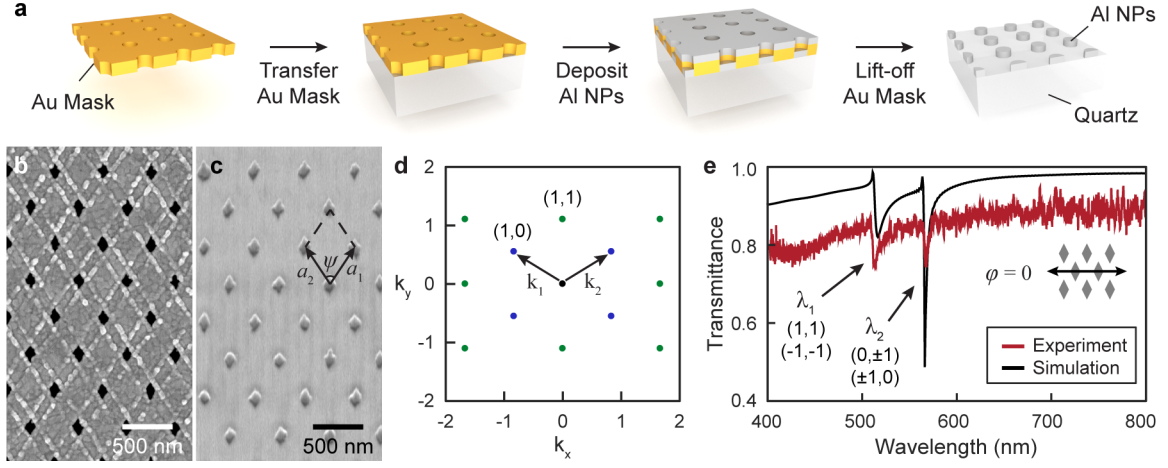


Figure 5.1. Low Symmetry Nanoparticle Arrays. (a) Fabrication scheme using a Au hole array as a physical deposition mask. (b) SEM image of a sample Au hole array patterned with a rhombus-shaped nanoholes arranged in a rhombohedral lattice. (c) SEM image of a rhombohedral Al nanoparticle array showing the lattice geometry. (d) The reciprocal space for a rhombohedral lattice with first order modes shown in blue and second order modes in green. (e) Transmission spectra showing two lattice modes.

The rhombohedral lattices were defined by two real-space basis vectors \mathbf{a}_1 and \mathbf{a}_2 of equal length forming a lattice angle ψ (**Figure 5.1c**, overlay) described by

$$(5.1) \quad \begin{aligned} \mathbf{a}_1 &= a \left\langle \frac{1}{2 \cos(\psi/2)}, \frac{1}{2 \sin(\psi/2)} \right\rangle \\ \mathbf{a}_2 &= a \left\langle \frac{-1}{2 \cos(\psi/2)}, \frac{1}{2 \sin(\psi/2)} \right\rangle \end{aligned}$$

with corresponding reciprocal space basis vectors \mathbf{k}_1 and \mathbf{k}_2

$$(5.2) \quad \begin{aligned} \mathbf{k}_1 &= \left\langle \cos(\psi/2), -\sin(\psi/2) \right\rangle \\ \mathbf{k}_2 &= \left\langle \cos(\psi/2), \sin(\psi/2) \right\rangle \end{aligned}$$

The reciprocal space lattices were indexed using (i, j) to represent a combination of reciprocal space basis vectors $\mathbf{k}_{ij} = i\mathbf{k}_1 + j\mathbf{k}_2$ (**Figure 5.1d**). Each point in reciprocal space represented a wave vector contribution for a Bragg diffraction mode in the array described by^{10,82}

$$(5.3) \quad \frac{\omega}{c} \sqrt{\epsilon_d} = |\mathbf{k}_{\parallel} + \mathbf{G}|$$

(i, j)	\mathbf{k}	$ \mathbf{k} $	$\lambda = \frac{na}{ \mathbf{k} }$
(1, 0) (0, 1)	$\langle \sin(\frac{\psi}{2}), \mp \cos(\frac{\psi}{2}) \rangle$	1	na
(-1, 0) (0, -1)	$\langle -\sin(\frac{\psi}{2}), \pm \cos(\frac{\psi}{2}) \rangle$	1	na
(1, 1) (-1, -1)	$\langle \pm 2 \sin(\frac{\psi}{2}), 0 \rangle$	$2 \sin \frac{\psi}{2}$	$\frac{na}{2 \sin \frac{\psi}{2}}$
(1, -1) (-1, 1)	$\langle 0, \mp 2 \cos(\frac{\psi}{2}) \rangle$	$2 \cos \frac{\psi}{2}$	$\frac{na}{2 \cos \frac{\psi}{2}}$

Table 5.1. Bragg modes for rhombohedral lattices. Bragg mode wave vectors are given for several diffraction modes using arbitrary lattice angle ψ and periodicity a to calculate the Bragg mode wavelength at normal incident angle. Degenerate modes are shown in the same color, with first-order modes in blue and second-order modes in green or red.

where ω is the angular frequency of light, c is the speed of light, and ϵ_d is the relative permittivity of the dielectric. $\mathbf{k}_{\parallel} = \mathbf{k}_0 \sin \theta$ is the in-plane wavevector of light with momentum \mathbf{k}_0 incident at angle θ . \mathbf{G} is the Bragg grating vector that depends upon periodicity a according to¹²⁴

$$(5.4) \quad \mathbf{G}_{ij} = \frac{2\pi}{a} \mathbf{k}_{ij}$$

Because we were interested in cavity modes that support lasing with emission normal to the array plane ($\theta = 0$) and wavelength $\lambda = 2\pi c/\omega$ may be substituted for frequency, **Equation 5.3** simplified to

$$(5.5) \quad \lambda_{ij} = \frac{na}{|\mathbf{k}_{ij}|}$$

where $n = \sqrt{\epsilon_d}$ is the refractive index of the dielectric environment. The wavelength for different diffraction modes (i, j) could then be calculated based upon the magnitude of its wave vector \mathbf{k}_{ij} . The reciprocal space vector from **Equation 5.2** was plugged into the Bragg grating vector in **Equation 5.4** to calculate expressions for the Bragg mode wavelengths at normal angle for specific diffraction modes using **Equation 5.5**. The values for the first-order modes (blue text) and second order modes (green or red text) were calculated in **Table 5.1** with degenerate modes shown in the same color text. These Bragg modes could be coupled to the nanoparticle LSP modes with proper spectral overlap to produce lattice plasmon

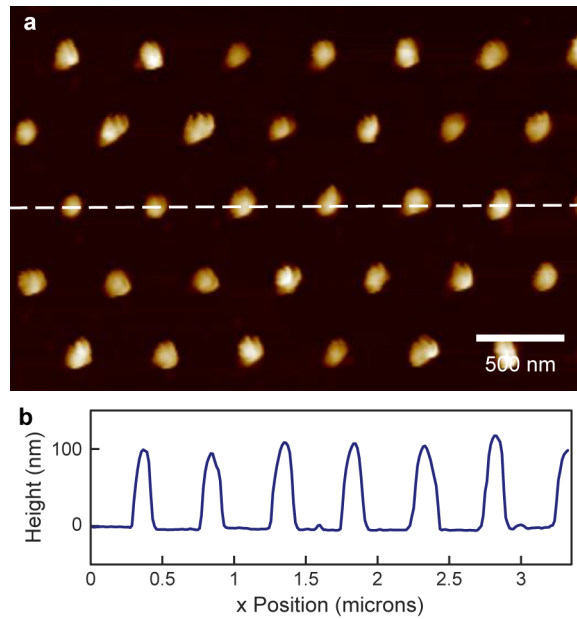


Figure 5.2. AFM of Al Nanoparticles. AFM image (a) and height profile (b) for the cross section shown in white dashed line. The arrays showed average nanoparticle heights of 100 nm.

resonances. Our samples used an $a = 400$ -nm periodic line mask and crossing angles between 60° - 70° to optimize the position of Bragg modes relative to the short-axis LSP of the 80×140 nm nanoparticles. AFM identified the nanoparticle height to be 100 nm (**Figure 5.2**).

The nanoparticle arrays were covered with dimethyl sulfoxide (DMSO) solvent to match the index of the quartz substrate. The normal angle transmission spectrum for an array of 67° lattice angle showed two lattice modes at $\lambda_1 = 513$ nm and $\lambda_2 = 570$ nm using in-plane polarization along the nanoparticle short axis ($\phi = 0^\circ$) (**Figure 5.1e**). The choice of Al as the nanoparticle material allowed for plasmonic resonances at shorter wavelengths than Au or Ag supported in previous studies. Comparison with a second array of 67° lattice angle showed similar behavior for $\lambda_2 = 570$ nm but a longer wavelength $\lambda_1 = 553$ nm (**Figure 5.3a-b**). To clarify the origin of these lattice plasmon modes, transmission spectra measured at off-normal incidence were collected to form dispersion diagrams (**Figure 5.3c-d**). The lattice modes closely followed the dispersion of Bragg modes from analytical calculations and formed two non-dispersive band edge states at normal incident angle. The band edge at λ_1 was found to couple with

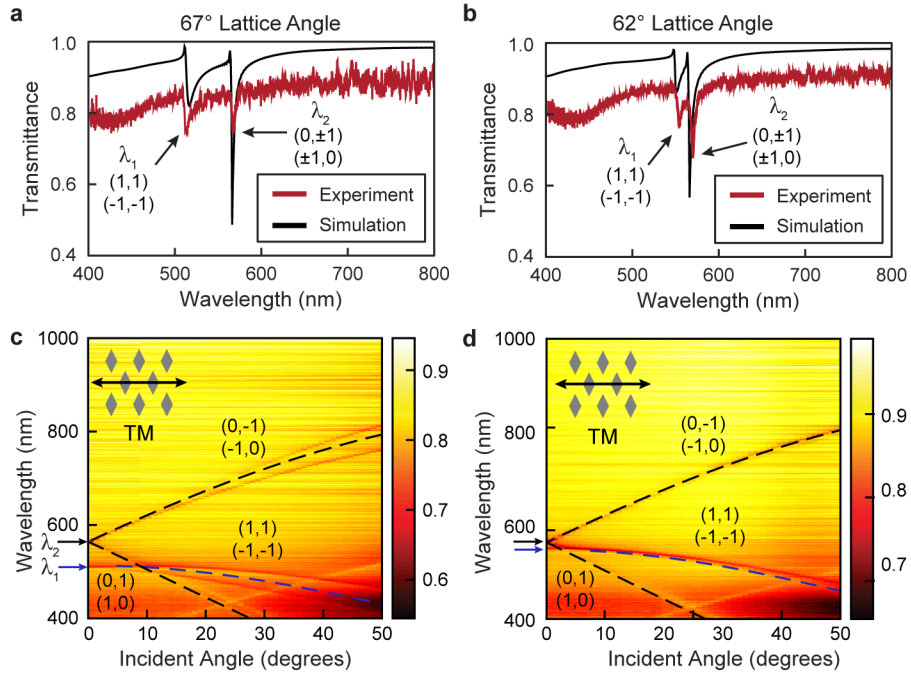


Figure 5.3. Transmission of Nanoparticle Arrays. (a-b) Normal incident angle transmission spectra for NP arrays of two lattice angles obtained from both experiment and simulation. (c-d) Dispersion diagrams of off-normal transmission with dashed lines showing analytical Bragg modes of first order (black) and second order (blue). λ_1 and λ_2 are identified using blue and black arrows, respectively.

the degenerate (1,1) and (-1,-1) modes, while the band edge at λ_2 formed at the crossing of the (0,1) and (1,0) modes with the (0,-1) and (-1,0) modes.

5.3. Nanoparticle Shape Effects in Lattice Plasmon Systems

The Al nanoparticle arrays were simulated using finite-difference time-domain methods and $n=1.41$ refractive index to represent the quartz/DMSO environment. Simulated transmission spectra showed lattice mode peaks matching the measured data (**Figure 5.1e** and **Figure 5.3a-b**), which demonstrated the FDTD model fit the samples well. Previous lattice plasmon studies considered primarily circular nanoparticles, so we used the FDTD simulations to analyze how anisotropic nanoparticle shape affected lattice mode coupling for a fixed lattice geometry. Plots of lattice plasmon phase showed standing wave behavior with preferred polarizations of $\phi_1 = 0^\circ$ for the λ_1 mode and $\phi_2 = 56.5^\circ$ for the λ_2 mode (**Figure**

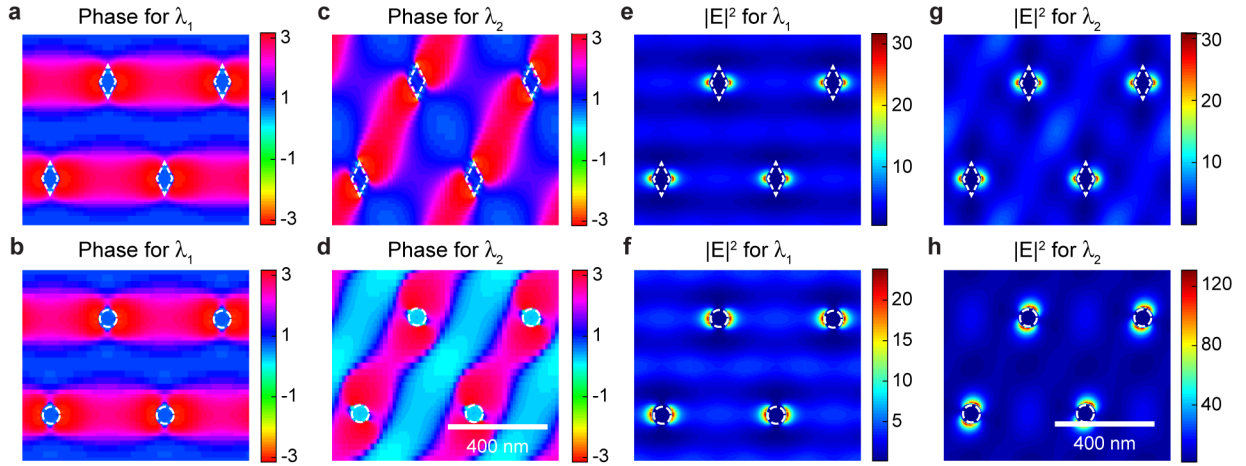


Figure 5.4. Near-field maps of rhombohedral and circular nanoparticles. (a-b) Phase for λ_1 showing standing waves under 0° polarization for the (1,1) mode for both rhombus-shaped and circular nanoparticles, respectively. (c-d) Phase for λ_2 showing standing waves under 56.5° polarization for the (1,0) mode. (e-f) Electric field intensity for λ_1 showing the (1,1) mode. (g-h) Electric field intensity for λ_2 showing the (1,0) mode.

5.4a-d). These polarizations were dictated by the (1,1) and (1,0) Bragg modes of the rhombohedral lattice geometry.

For the λ_1 mode with $\phi_1 = 0^\circ$ polarization, both circular and rhombus-shaped nanoparticles showed hot spots of high electromagnetic field intensity concentrated at the nanoparticle edges along the horizontal axis (**Figure 5.4e-f**). In the case of the λ_2 mode with $\phi_2 = 56.5^\circ$ polarization, hot spots appeared on the same horizontal axis of the rhombus-shaped nanoparticles, but shifted to the diagonal axis of the circular nanoparticles (**Figure 5.4g-h**). Nanoparticle symmetry was responsible for this difference in near-field behavior because isotropic (circular) nanoparticles support dipolar resonances along any axis, while anisotropic (rhombus-shaped) nanoparticles have preferred dipolar directions along their short and long axes. Therefore, our array geometry was an ideal example of using nanoparticle shape to control locations of hot spots and furthermore co-localize photonic modes of different polarizations.

5.4. Lasing Properties of Co-localized Cavity Modes

In lasing systems, spatially overlapping modes frequently compete for energy from gain material. To test how co-localized lattice plasmon modes would interact, we coupled our arrays to a laser dye

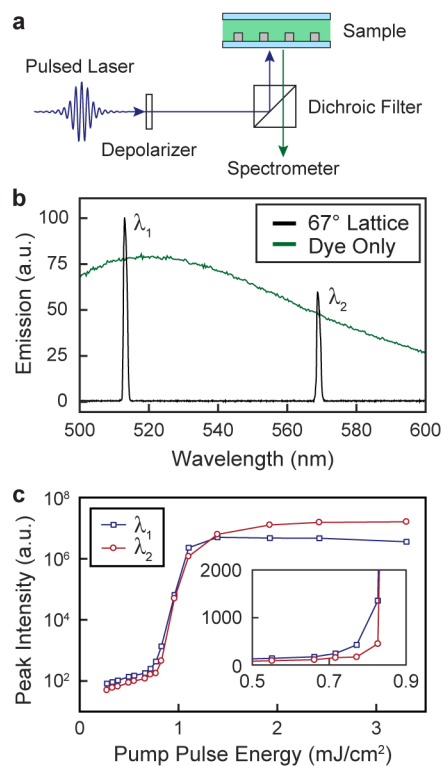


Figure 5.5. Lasing measurements of rhombohedral array. (a) Scheme of experimental setup for lasing measurements pumping and collecting emission at normal incident angle. (b) Lasing spectrum for 67° lattice angle with overlay of dye emission. (c) Light-light curve showing evolution of lasing emission intensity for increasing pump intensity with an inset showing a zoomed-in view of the lasing threshold.

(C-481) emitting at green wavelengths with good spectral overlap with the lattice modes. Samples were excited with an unpolarized pump beam, and emission spectra were collected at normal angle (**Figure 5.5a**). Spectrally narrow lasing peaks (FWHM < 1.5 nm) appeared at both λ_1 and λ_2 lattice plasmon wavelengths (**Figure 5.5b**). Emission intensity at peak wavelengths showed threshold behavior between 0.7-0.8 mJ/cm² for both lasing modes (**Figure 5.5c**). Lasing intensities rose sharply above threshold. The slope was steeper than in previous studies due to the higher concentration of dye molecules (20 mMol) which provided increased gain. Above 1.5 mJ/cm² pump intensity, lasing emission plateaued and remained stable up to maximum pump intensity of 3.3 mJ/cm². Lasing from a 67° array showed similar characteristics, but with slightly lower thresholds (0.6-0.7 mJ/cm²) likely due to minor differences in

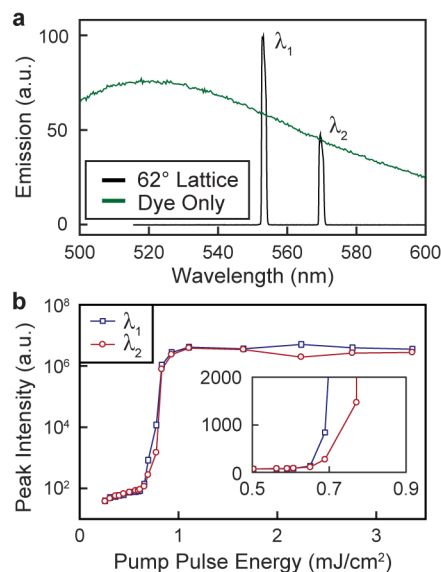


Figure 5.6. Lasing measurements with different lattice angle. (a) Lasing spectrum for 62° lattice angle with overlay of dye emission. (b) Light-light curve showing evolution of lasing emission intensity for increasing pump intensity with an inset showing a zoomed-in view of the lasing threshold.

nanoparticle size (**Figure 5.6**). Far-field emission profiles were measured to assess the directionality of laser output. In all cases, beams showed well-confined emission with divergence angles of $1.5^\circ \times 0.5^\circ$ or less (**Figure 5.7**). Beam profiles were elongated due to amplified spontaneous emission at slightly non-zero emission angles.

To better understand how our rhombohedral nanoparticle arrays supported two lasing modes despite spatial overlap in their near-field distributions, we performed FDTD simulations of Al nanoparticles embedded in a 4-level gain medium modeled after the dye. The system was pumped with a 400-nm light pulse, and changing in-plane pump polarization caused switching between lasing modes (**Figure 5.8a**). λ_1 lasing preferred pumping near $\phi_1 = 0^\circ$ while λ_2 lasing preferred pumping near $\phi_2 = 56.5^\circ$, and both modes were supported at intermediate polarizations. Rather than monitoring population inversion, which offers no information about emission wavelengths, we studied the near-field intensities at the specific lasing wavelengths (with more than 100 nm of spectral separation from the pump source). Mapping emission in the near field for both wavelengths showed the two modes were co-localized on the same corners of the

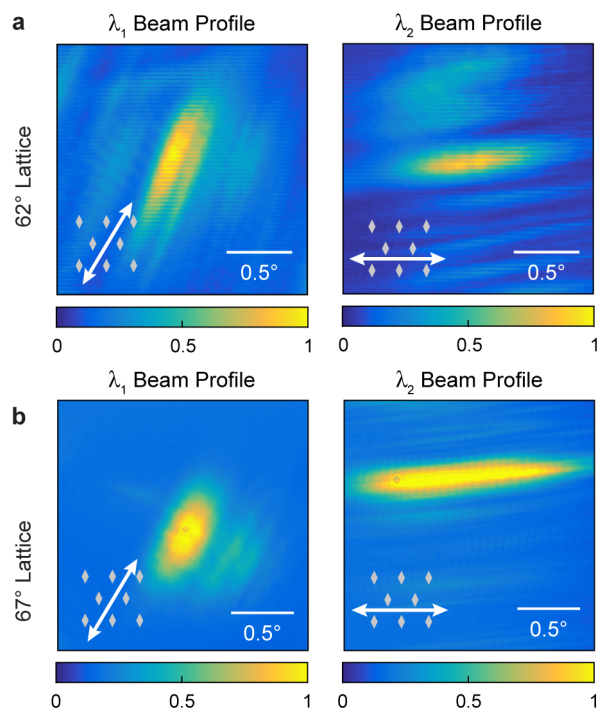


Figure 5.7. Beam profile measurements. Far-field beam profiles for both laser wavelengths from the 62° lattice (a) and 67° lattice (b) showing directional emission with small divergence angles in all cases.

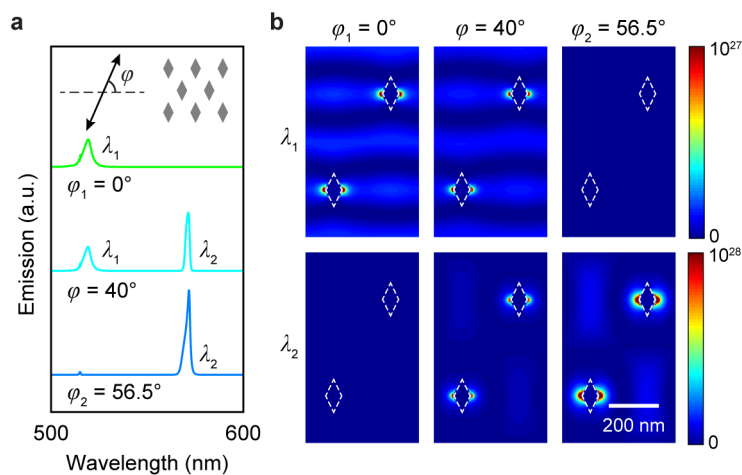


Figure 5.8. Simulated lasing near-field profiles. (a) Simulated lasing spectra of a 67° array for different in-plane polarization angles ϕ . (b) Associated near-field mappings of lattice plasmon laser emission for different polarizations plotted for the λ_1 mode (top) and λ_2 mode (bottom) showing lasing hot spots at the nanoparticle corners.

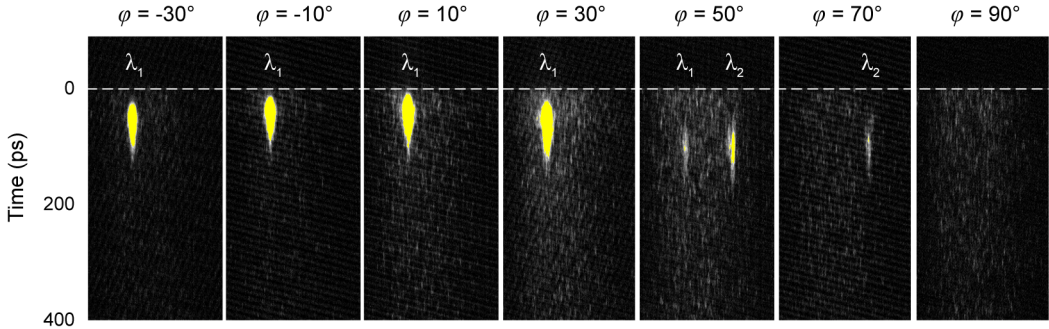


Figure 5.9. Polarization dependent lasing dynamics. Spectrally resolved time-correlated single-photon counting images showing lasing output as a function of time and wavelength for different in-plane pump polarizations in the case of a 67° array.

nanoparticles (**Figure 5.8b**). The hot spots showed no λ_1 emission for $\phi_2 = 56.5^\circ$, and no λ_2 emission for $\phi_1 = 0^\circ$. In these two cases, the difference in polarization between the lattice plasmon modes and gain dipoles was too great to allow for efficient plasmon-exciton coupling and energy transfer. This polarization dependence provided insight regarding our experimental lasing system. Although the two lattice plasmon modes occupied the same hot spots, they coupled to different populations of dye molecules within that nanoscopic volume according to dipole orientations. Therefore, simultaneous lasing from the two modes benefits from the random dipole orientations of dye molecules dispersed in solution. The implications of such effects must be kept in mind when considering integration of gain materials with polarization-dependent emission responses, such as many low-dimensional materials.

5.5. Influence of Pump Polarization on Lasing Dynamics

We found that pump polarization influenced plasmon-exciton coupling efficiency, which can affect not only the spectral output but also the lasing dynamics. We studied this property using spectrally resolved time-correlated single-photon counting (TCSPC), which mapped emission intensity as a function of time and wavelength (**Figure 5.9**). Lasing signal appeared for λ_1 and λ_2 near their preferred polarizations of $\phi_1 = 0^\circ$ and $\phi_2 = 56.5^\circ$, respectively. The λ_1 mode emitted brighter and for more polarization angles than the λ_2 mode because measurements were conducted just above threshold to discern changes in dynamics without saturating gain. Rising time provides one metric of emission dynamics and is characterized by

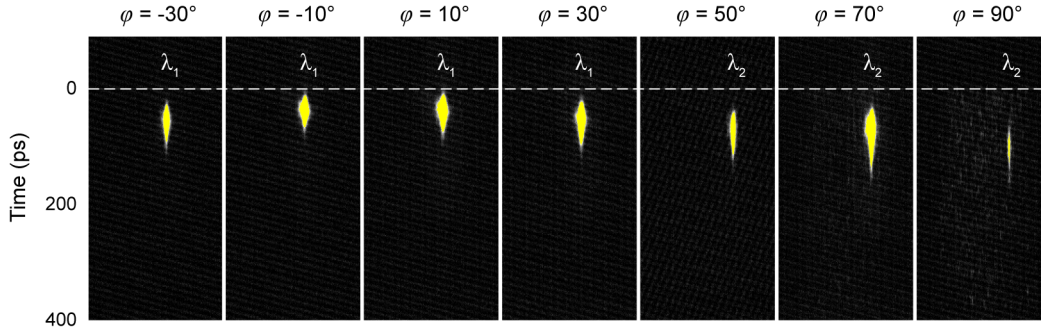


Figure 5.10. Lasing dynamics with different lattice angle. Spectrally resolved time-correlated single-photon counting images for a 62° array.

the delay between the pump pulse ($t = 0$) and the onset of lasing. We observed shorter λ_1 rising times for polarizations close to $\phi_1 = 0^\circ$ for both the 67° array (**Figure 5.9**) and the 62° array (**Figure 5.10**).

Another important metric of dynamics is the emission decay lifetime, which is found by fitting an exponential decay function to the emission intensity. We binned the emission data according to wavelength to examine the time component (**Figure 5.11**). The section of each curve following peak intensity was fit using a single exponential decay function to extract the lifetimes. From this analysis, we discovered that λ_1 decay lifetime was shorter for polarizations close to the ideal case of $\phi_1 = 0^\circ$ for both lattice angles tested. Although λ_2 lasing occurred for fewer polarizations, the lifetimes and rising times were also shortest near the preferred polarization of $\phi_2 = 56.5^\circ$ (or 59°). Furthermore, these lasing lifetimes of 7-30 ps were an order of magnitude shorter than the 586 ps emission decay lifetime measured for the dye solution (**Figure 5.12**). The observation of accelerated dynamics at preferred polarizations could be explained by plasmon-exciton coupling conditions. Dipoles in the dye were excited with orientations aligned with the pump beam polarization. Plasmon-exciton energy transfer was faster for dye excitons and lattice plasmon modes that were aligned, leading to faster lasing dynamics for both the onset of lasing (rising time) and the depletion of excited gain populations (decay lifetime).

Changes in lasing dynamics due to pump polarization were further examined using FDTD simulations of nanoparticle arrays embedded in gain media. The overall lasing emission field intensity and spectral

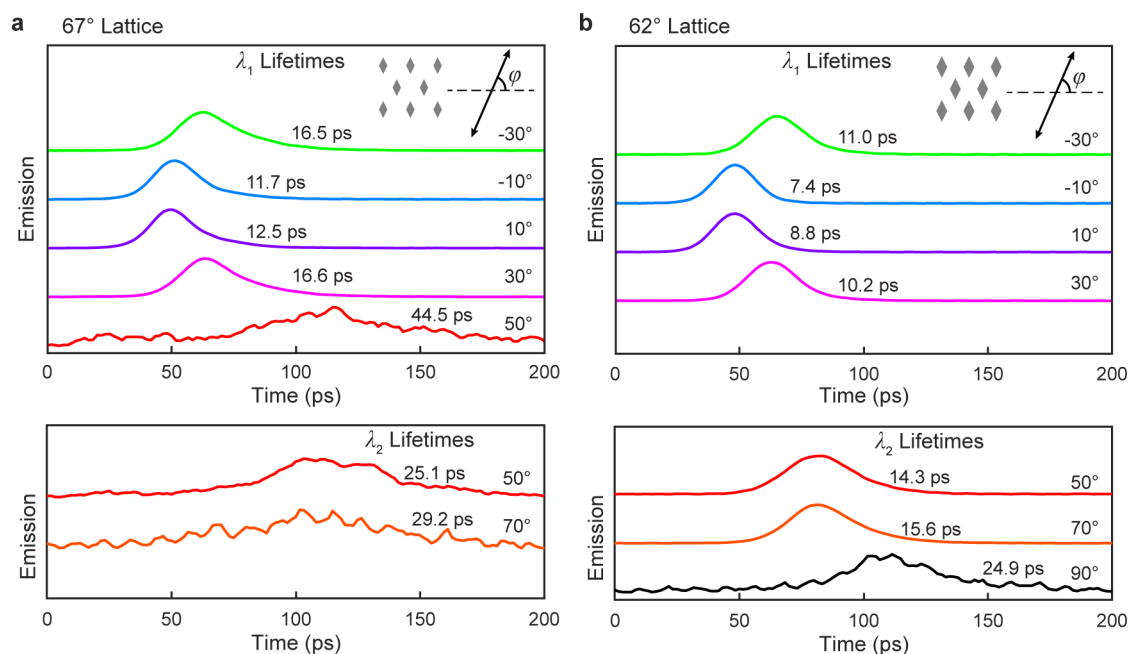


Figure 5.11. Trends in lasing dynamics. Emission curves showing lasing output as a function of time for a 67° array (a) and a 62° array (b). Curves are normalized and plotted on a linear scale. Emission decay lifetimes are included for the exponential decay functions fit to each curve. (Only time points after each peak were included in the fitting.)

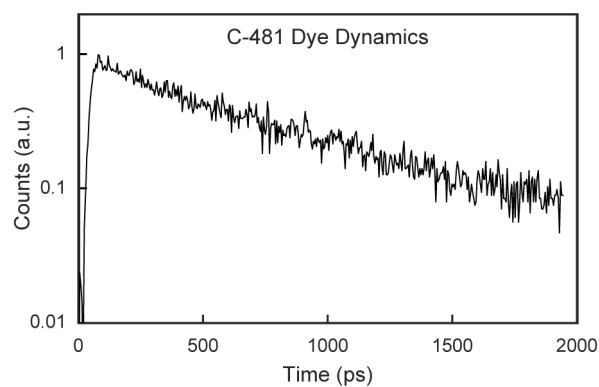


Figure 5.12. Intrinsic dye dynamics. C-481 dye emission showed an intrinsic emission decay lifetime of 586 ps without a photonic cavity.

output varied with pump polarization (**Figure 5.13**). While the simulated dynamics occurred on faster timescales than the experimental measurements, the qualitative behavior was the same. The field intensity

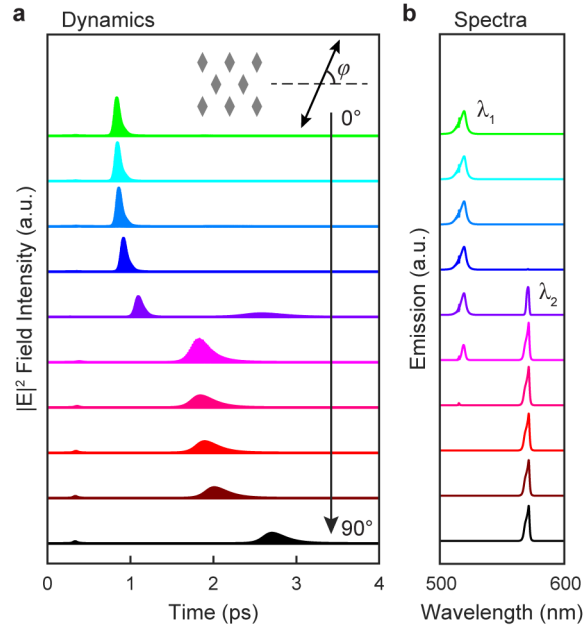


Figure 5.13. Simulated lasing dynamics. Simulated field intensity over time (a) and spectral output (b) for different in-plane pump polarizations. λ_1 lasing appears for polarizations of $0\text{-}50^\circ$ with rising times between 1-2 ps. λ_2 lasing appears for polarizations of $40\text{-}90^\circ$ with rising times between 2-3 ps. Dynamics were accelerated near ideal polarizations of 0° and 56.5° , respectively.

dynamics showed two sets of emission peaks (**Figure 5.13a**). The earlier set of field intensity peaks from 1-2 ps corresponded to λ_1 lasing while the second set of peaks from 2-3 ps arose from λ_2 lasing, and these assignments were confirmed using the emission spectra (**Figure 5.13b**). At 50 polarization (bright pink curve), the two modes lased simultaneously, so the single wave packet was a convolution of the two lasing frequencies. As in the experimental dynamics measurements, λ_1 lasing preferred polarizations close to $\phi_1 = 0^\circ$, while λ_2 lasing preferred polarizations near $\phi_2 = 56.5^\circ$. Therefore, the fastest dynamics in terms of both rising times and decay lifetimes were observed at these pump polarizations, which supported our proposed mechanism.

5.6. Summary

In summary, we developed a new fabrication process for patterning low-symmetry plasmonic arrays composed of rhombus-shaped nanoparticles arranged in rhombohedral lattices. This platform allowed us

to uncover symmetry effects in lattice plasmon lasing, including the roles of anisotropic nanoparticles and pump polarization. We found that nanoparticle shape is the dominant factor in defining lattice plasmon hot spots, while lattice geometry determines lattice mode polarization direction. Therefore, lasing modes were spatially co-localized while still coupling to different populations of excited gain according to their polarizations. Furthermore, lasing dynamics were accelerated using pump polarizations aligned with the lattice plasmon modes due to improved plasmon-exciton energy transfer. This study provides design rules for lasing systems more broadly, suggesting polarizations must be considered in coupling photonic cavities to emitters with anisotropic optical properties such as many low-dimensional semiconductors.

5.7. Methods

5.7.1. Fabrication of Au Hole Array Masks

Si wafers were treated with MicroChem MCC Primer 80/20. Shipley 1805 photoresist was diluted with propylene glycol monomethyl ether acetate (PGMEA), spun on the wafers to thicknesses of 60-90 nm, and baked at 115 C for λ_2 minutes. PDMS stamps patterned with 400-nm periodic lines were used to perform solvent-assisted nanoscale embossing (SANE) with dimethylformamide (DMF) as the solvent.²⁶ Residual resist was removed with a brief oxygen plasma treatment. A thin (7-nm) Cr film was deposited by thermal evaporation, followed by resist liftoff using MicroChem Remover 1165. The previous steps were repeated a second time to with the lines rotated at the chosen lattice angle to form a Cr hole array. Si masked by Cr was etched to form pits by deep reactive ion etching (DRIE) using a co-flow of SF₆ and C₄F₈ process gases.^{98,99} A thick (120-nm) layer of Au was deposited by thermal evaporation, producing a gold hole array. Wet etching the Cr adhesion layer (Transene Cr Etchant) released the Au hole array from the silicon, so it could float on water for transfer to a quartz substrate. Al nanoparticles 100-nm tall were deposited by e-beam evaporation using the Au hole array as a physical deposition mask, after which the mask was removed using adhesive tape.

5.7.2. Band Structure Mapping

The band structures are mapped using a transmission spectrometer setup with the sample mounted on a motor-controlled rotation-axis stage. White light from a lamp is focused to a beam and directed through the sample. The transmitted light is coupled into an optical fiber and directed to a grating spectrometer with a CCD camera. The angle of the samples is rotations in increments of 1° and a transmission spectrum is collected at each angle. The data are then plotted as either individual spectra or compiled into dispersion diagrams showing transmission intensity as a function of wavelength (related to frequency or energy) and angle (related to the in-plane wave vector) to observe the optical band structure.

5.7.3. Finite-Difference Time-Domain Simulations

Simulations were performed using commercial software (Lumerical). Simulations used a background index of $n = 1.41$, and a 4-nm mesh was applied to the rhombohedral Al nanoparticles (Palik). The rhombohedral lattice geometry was defined using 2 or 4 nanoparticles per simulation area and applying periodic (non-symmetric) x- and y-boundary conditions. Perfectly matched layers were applied at the z-boundary conditions. Transmission simulations used a broadband light source, while lasing simulations were pumped using a 400-nm wavelength. For lasing simulations, nanoparticles were embedded in a layer of gain material modeled after the 4-level laser dye with an absorption peak near 400 nm, broad emission centered at 520 nm, and concentration equivalent to 20 mMol.

The near-field plots in **Figure 5.8** were created by exporting the electric field monitor data from Lumerical into Matlab data files (Appendix A). A Matlab script was then used to calculate the phase at polarization angles selected to match the mode polarization angle, as this functionality is not built in to Lumerical. This phase calculation is based upon the complex field components $E_x(x, y, z)$ and $E_y(x, y, z)$

since the polarization ϕ is in the x - y plane:

$$\begin{aligned}
 \text{Re}(E) &= \cos(\phi) \text{Re}(E_x) + \sin(\phi) \text{Re}(E_y) \\
 \text{Im}(E) &= \cos(\phi) \text{Im}(E_x) + \sin(\phi) \text{Im}(E_y) \\
 \text{phase} &= \arctan\left(\frac{\text{Im}(E)}{\text{Re}(E)}\right)
 \end{aligned}
 \tag{5.6}$$

5.7.4. Lasing Measurements

A drop of 20 mMol solution of C-481 dye dissolved in DMSO was placed on each nanoparticle array and capped with a cover slip. The completed samples were pumped at normal incidence using 400-nm light with a pulse frequency of 1 kHz, beam diameter of 152 microns, and pulse energies between 0-3.3 mJ/cm² using a variable neutral density filter. The polarized pump beam was either passed through a depolarizer to produce unpolarized light or through a half-wave plate to rotate the in-plane polarization angle. Pulsed laser emission was collected at normal angle with pump signal removed using a dichroic filter and long-pass filters. Far-field emission with a free space distance of at least several cm was measured using either a spectrometer, beam profiler, or streak camera.

5.7.5. Beam Profile Measurements

A two-dimensional charge coupled device (CCD) array was positioned directly behind the nanolaser to collect the normal angle emission. A combination of two long-pass filters (560 nm and 570 nm) was used to isolate the redder mode at 570 nm, and they were replaced with a band pass filter (550 ± 10 nm) to isolate the bluer mode at 553 nm. The effectiveness of these filters was verified based on the laser spectral profiles before implementing the filters with the beam profiler. The intensity distribution above lasing threshold was mapped spatially for the beam profile cross-section in the x - y plane. The distance z from the nanolaser to the beam profiler CCD was measured and used to convert from pixels to divergence angle:

$$\text{divergence angle} = \arctan\left(\frac{\# \text{ of pixels}}{z} \times \frac{1 \text{ mm}}{375 \text{ pixels}}\right)
 \tag{5.7}$$

5.7.6. Time-Correlated Single-Photon Counting Measurements

Emission was coupled into a streak camera that was locked to the 1 kHz repetition rate of the pump laser so repeating nanolaser pulses were synchronized on the camera. Integration times of 0.5 seconds allowed averaging over several nanolaser pulses for better signal to noise ratios. Streak camera data was binned by wavelength with an 8-nm bin width around each laser mode. Each emission curve was fit to a single exponential decay using only the time points after its peak emission intensity.

CHAPTER 6

Conclusion and Outlook

This dissertation discussed a variety of methods for manipulating the plasmonic responses of metallic nanostructures to target specified properties. Chapter 1 discussed the fundamental properties of plasmonic resonances and the parameters that are relevant for tuning their optical responses. We used this information to identify potential methods for controlling the geometrical nanostructuring of plasmonic optical resonators for applications in ultraviolet plasmonics, fluorescence enhancement, and lasing.

Chapter 2 developed a nanopatterning process for sequential feature density of line arrays, which was used for generating plasmonic substrate showing SPP modes at UV wavelengths. This patterning process shows potential for a wide assortment of applications in industry and research where fast, parallel, and scalable patterning methods are needed for studying large area samples. This is critical for nanostructures that show angle-dependent properties, which are difficult to observe for small pattern areas. And it is further useful for applications like photocatalysis, with large area substrates providing suitably large areas for interfacing with reactive species. This fabrication method holds greater potential when expanded from 1D arrays to 2D arrays, enabling potential studies of large-area samples of nanoparticles with 100–200 nm spacings for ultraviolet lattice plasmon modes.

Chapters 3 and 4 examined the concept of enhancing fluorescence of semiconducting carbon nanotubes and few-layer black phosphorus, respectively, by integrating them with resonant optical cavities. These chapters demonstrated strategies for tuning lattice plasmon modes based upon the emission profiles and constraints of different emitters. Lattice plasmon modes were manipulated through independent control over the LSP modes and diffraction modes through informed choices and optimizations for the lattice spacing, nanoparticle dimensions, and dielectric materials. Using these techniques, high spectral overlap was achieved in both systems.

In both cases we observed an enhancement factor of 2 in the PL intensity when compared to SWNTs or phosphorene without the nanoparticle arrays. Improving this enhancement factor could be approached from a number of directions. In particular, the nanotubes likely showed poor spatial overlap with the nanoparticle lattice modes. This could be remedied by decreasing the thickness of the nanotube films, to reduce the number of nanotubes contributing un-enhanced PL outside the plasmonic hot spots. In the case of phosphorene, a major limitation was the overall low PL signal due to the sparse coverage of the

phosphorene flakes. Techniques for large area deposition of phosphorene may provide higher PL signals and with more consistent intensities that will allow for more robust measurements without the need for PL normalization by Raman intensity. This would also allow for identifying the crystal orientation for individual flakes, so that a consistent polarization of light could be used in each case.

Chapter 6 developed a new fabrication method for created low-symmetry plasmonic arrays that were used to examine the effects of nanoparticle shape and lattice angle in photonic systems. Anisotropic nanoparticles were found to localize electromagnetic hot spots along their short and long axes, regardless of the direction of diffractive coupling between nanoparticles. In this way, lattice plasmon modes could be spatially co-localized to the same electromagnetic hot spots, which generated unusual and insightful lasing properties. Lattice plasmon lasing occurred for both modes simultaneously, with changes in both spectral output and emission dynamics depending on in-plane pump polarization. These characteristics revealed that energy transfer rates for plasmon-exciton coupling are tied to relative orientations of these dipolar excitations, with good alignment producing stronger coupling and faster energy transfer dynamics. Therefore, lasing modes are able to emit from the same nanoscopic hot spots by drawing energy from different populations of dye molecules based on dipole orientation. In a broader context, this uncovers mode polarization and gain dipole orientations as important considerations for the coupling of photonic cavities with gain media showing anisotropic optical properties.

Aside from understanding the fundamental physics of these lattice plasmon laser systems, our work also lays the foundation for applications in multi-color lasers. Photonic lasers based on Fabry-Pérot cavities generally support several optical modes with small wavelength separation, depending upon cavity length.⁸ This property makes it challenging to design photonic lasers that have a few specifically selected lasing wavelengths. Here we have shown that lattice plasmons, which previously supported a single lasing mode, can be engineered based on lattice angle to produce two lasing modes. Crossing lines of different periodicities would break the degeneracy of the $(0, 1)$ and $(1, 0)$ modes and produce three-color lasers with modes that can be tuned independently based upon periodicity one, periodicity two, and lattice angle. This advance would open new possibilities for RGB lasers and white-light sources.

References

- [1] Henzie, J.; Lee, J.; Lee, M. H.; Hasan, W.; Odom, T. W., Nanofabrication of plasmonic structures. *Annual review of physical chemistry* **2009**, *60*, 147–165.
- [2] Lee, M. H.; Huntington, M. D.; Zhou, W.; Yang, J.-c.; Odom, T. W., Programmable Soft Lithography : Solvent-Assisted Nanoscale Embossing. *Nano Letters* **2011**, *11*, 311–315.
- [3] Oulton, R. F.; Sorger, V. J.; Zentgraf, T.; Ma, R.-M.; Gladden, C.; Dai, L.; Bartal, G.; Zhang, X., Plasmon lasers at deep subwavelength scale. *Nature* **2009**, *461* (7264), 629–632.
- [4] Zhang, Q.; Li, G.; Liu, X.; Qian, F.; Li, Y.; Sum, T. C.; Lieber, C. M.; Xiong, Q., A room temperature low-threshold ultraviolet plasmonic nanolaser. *Nature Communications* **2014**, *5*, 4953.
- [5] Ma, R.-M.; Ota, S.; Li, Y.; Yang, S.; Zhang, X., Explosives detection in a lasing plasmon nanocavity. *Nat Nano* **2014**, *9* (8), 600–604.
- [6] Augu e, B.; Barnes, W., Collective Resonances in Gold Nanoparticle Arrays. *Physical Review Letters* **2008**, *101* (14), 143902.
- [7] Zou, S.; Janel, N.; Schatz, G. C., Silver nanoparticle array structures that produce remarkably narrow plasmon lineshapes. *The Journal of chemical physics* **2004**, *120* (23), 10871–5.
- [8] Wang, D.; Wang, W.; Knudson, M. P.; Schatz, G. C.; Odom, T. W., Structural Engineering in Plasmon Nanolasers. *Chemical Reviews* **2017**.
- [9] Wang, D.; Yang, A.; Wang, W.; Hua, Y.; Schaller, R. D.; Schatz, G. C.; Odom, T. W., Band-edge engineering for controlled multi-modal nanolasing in plasmonic superlattices. *Nature Nanotechnology* **2017**, *12* (9), 889–894.
- [10] Zhou, W.; Dridi, M.; Suh, J. Y.; Kim, C. H.; Co, D. T.; Wasielewski, M. R.; Schatz, G. C.; Odom, T. W., Lasing action in strongly coupled plasmonic nanocavity arrays. *Nature nanotechnology* **2013**, *8* (7), 506–11.

- [11] Yang, A.; Hoang, T. B.; Dridi, M.; Deeb, C.; Mikkelsen, M. H.; Schatz, G. C.; Odom, T. W., Real-time tunable lasing from plasmonic nanocavity arrays. *Nature Communications* **2015**, *6*, 6939.
- [12] Zhang, L. L.; Zhao, X. S., Carbon-based materials as supercapacitor electrodes. *Chemical Society Reviews* **2009**, *38* (9), 2520–2531.
- [13] Bachilo, S. M.; Strano, M. S.; Kittrell, C.; Hauge, R. H.; Smalley, R. E.; Weisman, R. B., Structure-Assigned Optical Spectra of Single-Walled Carbon Nanotubes. *Science* **2002**, *298*, 2361–2366.
- [14] Bagheri, S.; Mansouri, N.; Aghaie, E., Phosphorene: A new competitor for graphene. *International Journal of Hydrogen Energy* **2016**, *41* (7), 4085–4095.
- [15] Maier, S. A., *Plasmonics: Fundamentals and Applications* Springer Science **2007**.
- [16] Culver, K. S. B.; Shin, Y. J.; Rotz, M. W.; Meade, T. J.; Hersam, M. C.; Odom, T. W., Shape-Dependent Relaxivity of Nanoparticle-Based T1 Magnetic Resonance Imaging Contrast Agents. *The Journal of Physical Chemistry C* **2016**, *120* (38), 22103–22109.
- [17] Atwater, H. A.; Polman, A., Plasmonics for improved photovoltaic devices. *Nature Materials* **2010**, *9*, 205.
- [18] Hu, J.; Liu, C.-H.; Ren, X.; Lauhon, L. J.; Odom, T. W., Plasmonic Lattice Lenses for Multiwavelength Achromatic Focusing. *ACS Nano* **2016**, *10* (11), 10275–10282.
- [19] Gao, H.; Henzie, J.; Lee, M. H.; Odom, T. W., Screening plasmonic materials using pyramidal gratings. *Proceedings of the National Academy of Sciences of the United States of America* **2008**, *105* (51), 20146–20151.
- [20] Barnes, W. L.; Murray, W. A.; Dintinger, J.; Devaux, E.; Ebbesen, T. W., Surface Plasmon Polaritons and Their Role in the Enhanced Transmission of Light Through Periodic Arrays of Subwavelength Holes in a Metal Film. *Physical Review Letters* **2004**, *92* (10), 107401.
- [21] Grzelczak, M.; Pérez-Juste, J.; Mulvaney, P.; Liz-Marzán, L. M., Shape control in gold nanoparticle synthesis. *Chemical Society Reviews* **2008**, *37* (9), 1783.
- [22] Manikam, V. R.; Cheong, K. Y.; Razak, K. A., Chemical reduction methods for synthesizing Ag and Al nanoparticles and their respective nanoalloys. *Materials Science and Engineering: B* **2011**, *176* (3), 187–203.

- [23] Chandra, K.; Culver, K. S. B.; Werner, S. E.; Lee, R. C.; Odom, T. W., Manipulating the Anisotropic Structure of Gold Nanostars using Good's Buffers. *Chemistry of Materials* **2016**, *28* (18), 6763–6769.
- [24] Martin, J.; Plain, J., Fabrication of aluminium nanostructures for plasmonics. *Journal of Physics D: Applied Physics* **2015**, *48* (18), 184002.
- [25] Lipomi, D. J.; Martinez, R. V.; Cademartiri, L.; Whitesides, G. M., Soft Lithographic Approaches to Nanofabrication, volume 7 Elsevier B.V. **2012**.
- [26] Odom, T. W.; Love, J. C.; Wolfe, D. B.; Paul, K. E.; Whitesides, G. M., Improved Pattern Transfer in Soft Lithography Using Composite Stamps. *Langmuir* **2002**, *18*, 5314–5320.
- [27] Henzie, J.; Lee, M. H.; Odom, T. W., Multiscale patterning of plasmonic metamaterials. *Nature Nanotechnology* **2007**, *2* (9), 549–554.
- [28] Vogel, N.; Zieleniecki, J.; Koper, I., As flat as it gets: ultrasmooth surfaces from template-stripping procedures. *Nanoscale* **2012**, *4* (13), 3820–3832.
- [29] Nagpal, P.; Lindquist, N. C.; Oh, S.-H.; Norris, D. J., Ultrasmooth Patterned Metals for Plasmonics and Metamaterials. *Science* **2009**, *325* (5940), 594–597.
- [30] Yang, A.; Li, Z.; Knudson, M. P.; Hyrn, A. J.; Wang, W.; Aydin, K.; Odom, T. W., Unidirectional Lasing from Template-Stripped Two-Dimensional Plasmonic Crystals. *ACS nano* **2015**, *9* (12), 11582–11588.
- [31] Kolomenski, A.; Kolomenskii, A.; Noel, J.; Peng, S.; Schuessler, H., Propagation length of surface plasmons in a metal film with roughness. *Applied optics* **2009**, *48* (30), 5683–5691.
- [32] Park, J. H.; Nagpal, P.; McPeak, K. M.; Lindquist, N. C.; Oh, S.-H.; Norris, D. J., Fabrication of Smooth Patterned Structures of Refractory Metals, Semiconductors, and Oxides via Template Stripping. *ACS Applied Materials & Interfaces* **2013**, *5* (19), 9701–9708.
- [33] Yeo, L. P.; Yan, Y. H.; Lam, Y. C.; Chan-Park, M. B., Design of Experiment for Optimization of Plasma-Polymerized Octafluorocyclobutane Coating on Very High Aspect Ratio Silicon Molds. *Langmuir* **2006**, *22* (24), 10196–10203.

- [34] Li, X.; Zhu, J.; Wei, B., Hybrid nanostructures of metal/two-dimensional nanomaterials for plasmon-enhanced applications. *Chemical Society Reviews* **2016**, *45* (11), 3145–3187.
- [35] Ono, A.; Kikawada, M.; Akimoto, R.; Inami, W.; Kawata, Y., Fluorescence enhancement with deep-ultraviolet surface plasmon excitation. *Optics Express* **2013**, *21* (15), 17447–17453.
- [36] Jiao, X.; Blair, S., Optical antenna design for fluorescence enhancement in the ultraviolet. *Optics Express* **2012**, *20* (28), 29909–29922.
- [37] Ray, K.; Chowdhury, M. H.; Lakowicz, J. R., Aluminum nanostructured films as substrates for enhanced fluorescence in the ultraviolet-blue spectral region. *Analytical Chemistry* **2007**, *79* (17), 6480–6487.
- [38] Lozano, G.; Louwers, D. J.; Rodríguez, S. R.; Murai, S.; Jansen, O. T.; Verschuuren, M. a.; Gómez Rivas, J., Plasmonics for solid-state lighting: enhanced excitation and directional emission of highly efficient light sources. *Light: Science & Applications* **2013**, *2* (5), e66.
- [39] Zakharko, Y.; Graf, A.; Schießl, S. P.; Hähnlein, B.; Pezoldt, J.; Gather, M. C.; Zaumseil, J., Broadband Tunable, Polarization-Selective and Directional Emission of (6,5) Carbon Nanotubes Coupled to Plasmonic Crystals. *Nano Letters* **2016**, *16* (5), 3278–3284.
- [40] Ma, R.-M.; Oulton, R. F.; Sorger, V. J.; Zhang, X., Plasmon lasers: coherent light source at molecular scales. *Laser & Photonics Reviews* **2013**, *7* (1), 1–21.
- [41] Yang, A.; Wang, D.; Wang, W.; Odom, T. W., Coherent Light Sources at the Nanoscale. *Annual Review of Physical Chemistry* **2017**, *68* (1), 83–99.
- [42] Purcell, E., Spontaneous emission probabilities at radio frequencies. *Physical Review* **1946**, *69*, 681.
- [43] Iwase, H.; Englund, D.; Vu, J., Analysis of the Purcell effect in photonic and plasmonic crystals with losses. *Optics Express* **2010**, *18* (16), 16546–16560.
- [44] Zhang, S.; Park, Y.-S.; Liu, Y.; Zentgraf, T.; Zhang, X., Far-field measurement of ultra-small plasmonic mode volume. *Optics express* **2010**, *18* (6), 6048–55.
- [45] Suh, J. Y.; Kim, C. H.; Zhou, W.; Huntington, M. D.; Co, D. T.; Wasielewski, M. R.; Odom, T. W., Plasmonic bowtie nanolaser arrays. *Nano Letters* **2012**, *12* (11), 5769–5774.

- [46] Koenderink, A. F., On the use of Purcell factors for plasmon antennas. *Optics letters* **2010**, *35* (24), 4208–10.
- [47] Kristensen, P. T.; Van Vlack, C.; Hughes, S., Generalized effective mode volume for leaky optical cavities. *Optics letters* **2012**, *37* (10), 1649–51.
- [48] Kristensen, P. T.; Hughes, S., Modes and Mode Volumes of Leaky Optical Cavities and Plasmonic Nanoresonators. *ACS Photonics* **2014**, *1* (1), 2–10.
- [49] Saleh, B. E. A.; Teich, M. C., *Fundamentals of Photonics* Wiley, Hoboken, New Jersey **2007**, second edition.
- [50] Kasap, S. O., *Optoelectronics and Photonics: Principles and Practices* Pearson, Boston **2013**, second edition.
- [51] Maiman, T. H., Stimulated Optical Radiation in Ruby. *Nature* **1960**, *187* (4736), 493–494.
- [52] Moulton, P. F., Spectroscopic and laser characteristics of Ti:Al₂O₃. *Journal of the Optical Society of America B* **1986**, *3* (1), 125–133.
- [53] Geusic, J. E.; Marcos, H. M.; Van Uitert, L. G., Laser oscillations in Nd-Doped Yttrium Aluminum, Yttrium Gallium and Gadolinium Garnets. *Applied Physics Letters* **1964**, *4* (10), 182–184.
- [54] Ikesue, A.; Kinoshita, T.; Kamata, K.; Yoshida, K., Fabrication and Optical Properties of High-Performance Polycrystalline Nd:YAG Ceramics for Solid-State Lasers. *Journal of the American Ceramic Society* **1995**, *78* (4), 1033–1040.
- [55] Morgner, U.; Kärtner, F. X.; Cho, S. H.; Chen, Y.; Haus, H. A.; Fujimoto, J. G.; Ippen, E. P.; Scheuer, V.; Angelow, G.; Tschudi, T., Sub-two-cycle pulses from a Kerr-lens mode-locked Ti:sapphire laser. *Optics Letters* **1999**, *24* (6), 411–413.
- [56] Sutter, D. H.; Steinmeyer, G.; Gallmann, L.; Matuschek, N.; Morier-Genoud, F.; Keller, U.; Scheuer, V.; Angelow, G.; Tschudi, T., Semiconductor saturable-absorber mirror-assisted Kerr-lens mode-locked Ti:sapphire laser producing pulses in the two-cycle regime. *Optics Letters* **1999**, *24* (9), 631–633.
- [57] Bridges, W. B., Laser Oscillation in Singly Ionized Argon in the Visible Spectrum. *Applied Physics Letters* **1964**, *4* (7), 128–130.

- [58] Javan, A.; Bennett, W. R.; Herriott, D. R., Population Inversion and Continuous Optical Maser Oscillation in a Gas Discharge Containing a He-Ne Mixture. *Physical Review Letters* **1961**, *6* (3), 106–110.
- [59] Patel, C. K. N., Continuous-Wave Laser Action on Vibrational-Rotational Transitions of CO₂. *Physical Review* **1964**, *136* (5A), A1187–A1193.
- [60] Ewing, J. J.; Brau, C. A., Laser action on the $2\Sigma+1/22\Sigma+1/2$ bands of KrF and XeCl. *Applied Physics Letters* **1975**, *27* (6), 350–352.
- [61] Hall, R. N.; Fenner, G. E.; Kingsley, J. D.; Soltys, T. J.; Carlson, R. O., Coherent Light Emission From GaAs Junctions. *Physical Review Letters* **1962**, *9* (9), 366–368.
- [62] Holonyak, N.; Bevacqua, S. F., Coherent (Visible) Light Emission from Ga(As_{1-x}P_x) Junctions. *Applied Physics Letters* **1962**, *1* (4), 82–83.
- [63] Wang, C. A.; Groves, S. H., New materials for diode laser pumping of solid-state lasers. *IEEE Journal of Quantum Electronics* **1992**, *28* (4), 942–951.
- [64] Schäfer, F. P.; Schmidt, W.; Volze, J., Organic Dye Solution Laser. *Applied Physics Letters* **1966**, *9* (8), 306–309.
- [65] Soffer, B. H.; McFarland, B. B., Continuously Tunable, Narrow-Band Organic Dye Lasers. *Applied Physics Letters* **1967**, *10* (10), 266–267.
- [66] Fork, R. L.; Greene, B. I.; Shank, C. V., Generation of optical pulses shorter than 0.1 psec by colliding pulse mode locking. *Applied Physics Letters* **1981**, *38* (9), 671–672.
- [67] Hill, M. T.; Gather, M. C., Advances in small lasers. *Nature Photonics* **2014**, *8*, 908.
- [68] Ma, R.-M.; Yin, X.; Oulton, R. F.; Sorger, V. J.; Zhang, X., Multiplexed and Electrically Modulated Plasmon Laser Circuit. *Nano Letters* **2012**, *12* (10), 5396–5402.
- [69] Wang, S.; Li, B.; Wang, X.-Y.; Chen, H.-Z.; Wang, Y.-L.; Zhang, X.-W.; Dai, L.; Ma, R.-M., High-Yield Plasmonic Nanolasers with Superior Stability for Sensing in Aqueous Solution. *ACS Photonics* **2017**, *4* (6), 1355–1360.
- [70] Ma, R.-M.; Oulton, R. F.; Sorger, V. J.; Bartal, G.; Zhang, X., Room-temperature sub-diffraction-limited plasmon laser by total internal reflection. *Nat Mater* **2011**, *10* (2), 110–113.

- [71] Lu, Y.-J.; Kim, J.; Chen, H.-Y.; Wu, C.; Dabidian, N.; Sanders, C. E.; Wang, C.-Y.; Lu, M.-Y.; Li, B.-H.; Qiu, X.; Chang, W.-H.; Chen, L.-J.; Shvets, G.; Shih, C.-K.; Gwo, S., Plasmonic Nanolaser Using Epitaxially Grown Silver Film. *Science* **2012**, *337* (6093), 450 – 453.
- [72] Lu, Y.-J.; Wang, C.-Y.; Kim, J.; Chen, H.-Y.; Lu, M.-Y.; Chen, Y.-C.; Chang, W.-H.; Chen, L.-J.; Stockman, M. I.; Shih, C.-K.; Gwo, S., All-Color Plasmonic Nanolasers with Ultralow Thresholds: Autotuning Mechanism for Single-Mode Lasing. *Nano Letters* **2014**, *14* (8), 4381–4388.
- [73] van Beijnum, F.; van Veldhoven, P. J.; Geluk, E. J.; de Dood, M. J. a.; 't Hooft, G. W.; van Exter, M. P., Surface Plasmon Lasing Observed in Metal Hole Arrays. *Physical Review Letters* **2013**, *110* (20), 206802.
- [74] Agio, M.; Alu, A., Optical Antenna. *Cambridge University Press* **2013**.
- [75] Oulton, R. F.; Sorger, V. J.; Genov, D. A.; Pile, D. F. P.; Zhang, X., A hybrid plasmonic waveguide for subwavelength confinement and long-range propagation. *Nature Photonics* **2008**, *2*, 496.
- [76] Sidiropoulos, T. P. H.; Roder, R.; Geburt, S.; Hess, O.; Maier, S. A.; Ronning, C.; Oulton, R. F., Ultrafast plasmonic nanowire lasers near the surface plasmon frequency. *Nat Phys* **2014**, *10* (11), 870–876.
- [77] Manjavacas, A.; de Abajo, F. J. G.; Nordlander, P., Quantum Plexcitonics: Strongly Interacting Plasmons and Excitons. *Nano Letters* **2011**, *11* (6), 2318–2323.
- [78] Chen, H.-Z.; Hu, J.-Q.; Wang, S.; Li, B.; Wang, X.-Y.; Wang, Y.-L.; Dai, L.; Ma, R.-M., Imaging the dark emission of spasers. *Science Advances* **2017**, *3* (4).
- [79] Wang, X.-Y.; Wang, Y.-L.; Wang, S.; Li, B.; Zhang, X.-W.; Dai, L.; Ma, R.-M., Lasing Enhanced Surface Plasmon Resonance Sensing. *Nanophotonics* **2017**, *6* (2), 472–478.
- [80] Anker, J. N.; Hall, W. P.; Lyandres, O.; Shah, N. C.; Zhao, J.; Van Duyne, R. P., Biosensing with plasmonic nanosensors. *Nat Mater* **2008**, *7* (6), 442–453.
- [81] Guo, L.; Jackman, J. A.; Yang, H.-H.; Chen, P.; Cho, N.-J.; Kim, D.-H., Strategies for enhancing the sensitivity of plasmonic nanosensors. *Nano Today* **2015**, *10* (2), 213–239.
- [82] Hessel, A.; Oliner, A. A., A New Theory of Wood's Anomalies on Optical Gratings. *Applied Optics* **1965**, *4* (10), 1275–1297.

- [83] Wang, W.; Ramezani, M.; Väkeväinen, A. I.; Törmä, P.; Rivas, J. G.; Odom, T. W., The rich photonic world of plasmonic nanoparticle arrays. *Materials Today* **2017**.
- [84] McMahon, J. M.; Schatz, G. C.; Gray, S. K., Plasmonics in the ultraviolet with the poor metals Al, Ga, In, Sn, Tl, Pb, and Bi. *Physical Chemistry Chemical Physics* **2013**, *15* (15), 5415–5423.
- [85] Yarema, M.; Wörle, M.; Rossell, M. D.; Erni, R.; Caputo, R.; Protesescu, L.; Kravchyk, K. V.; Dirin, D. N.; Lienau, K.; von Rohr, F.; Schilling, A.; Nachttegaal, M.; Kovalenko, M. V., Monodisperse Colloidal Gallium Nanoparticles: Synthesis, Low Temperature Crystallization, Surface Plasmon Resonance and Li-Ion Storage. *Journal of the American Chemical Society* **2014**, *136* (35), 12422–12430.
- [86] Zettsu, N.; McLellan, J. M.; Wiley, B.; Yin, Y.; Li, Z.-Y.; Xia, Y., Synthesis, Stability, and Surface Plasmonic Properties of Rhodium Multipods, and Their Use as Substrates for Surface-Enhanced Raman Scattering. *Angewandte Chemie International Edition* **2006**, *45* (8), 1288–1292.
- [87] Honda, M.; Kumamoto, Y.; Taguchi, A.; Saito, Y.; Kawata, S., Plasmon-enhanced UV photocatalysis. *Applied Physics Letters* **2014**, *104* (6), 061108.
- [88] Peng, S.; Sheldon, M. T.; Liu, W.-g.; Jaramillo-botero, A.; Andrew, W.; Iii, G.; Atwater, H. A., Ultraviolet surface plasmon-mediated low temperature hydrazine decomposition. *Applied Physics Letters* **2015**, *106* (023102).
- [89] Ding, T.; Sigle, D. O.; Herrmann, L. O.; Wolverson, D.; Baumberg, J. J., Nanoimprint Lithography of Al Nanovoids for Deep-UV SERS. *ACS Applied Materials & Interfaces* **2014**, *6* (20), 17358–17363.
- [90] Myers, B. D.; Dravid, V. P., Variable Pressure Electron Beam Lithography (VP-eBL): A New Tool for Direct Patterning of Nanometer-Scale Features on Substrates with Low Electrical Conductivity. *Nano Letters* **2006**, *6* (5), 963–968.
- [91] Okada, M.; Matsui, S., High-resolution line and space pattern fabrication by electron beam lithography using NEB-22 resist. *Japanese Journal of Applied Physics* **2015**, *54* (11), 118004.
- [92] Bloomstein, T. M.; Marchant, M. F.; Deneault, S.; Hardy, D. E.; Rothschild, M., 22-nm immersion interference lithography. *Optics Express* **2006**, *14* (14), 6434–6443.

- [93] Yang, A.; Hryn, A. J.; Bourgeois, M. R.; Lee, W.-K.; Hu, J.; Schatz, G. C.; Odom, T. W., Programmable and reversible plasmon mode engineering. *Proceedings of the National Academy of Sciences* **2016**, *113* (50), 14201–14206.
- [94] Bencher, C.; Chen, Y.; Dai, H.; Montgomery, W.; Huli, L., 22nm half-pitch patterning by CVD spacer self alignment double patterning (SADP). *Proceedings of SPIE* **2008**, *6924*, 69244E.
- [95] Raley, A.; Thibaut, S.; Mohanty, N.; Subhadeep, K.; Nakamura, S.; Ko, A.; O'Meara, D.; Tapily, K.; Consiglio, S.; Biolsi, P., Self-aligned quadruple patterning integration using spacer on spacer pitch splitting at the resist level for sub-32nm pitch applications. *Proceedings of SPIE* **2016**, *9782*, 97820F.
- [96] Yu, Z.; Wu, W.; Chen, L.; Chou, S. Y., Fabrication of large area 100 nm pitch grating by spatial frequency doubling and nanoimprint lithography for subwavelength optical applications. *Journal of Vacuum Science & Technology B: Microelectronics and Nanometer Structures Processing, Measurement, and Phenomena* **2001**, *19* (6), 2816–2819.
- [97] Love, J. C.; Paul, K. E.; Whitesides, G. M., Fabrication of nanometer-scale features by controlled isotropic wet chemical etching. *Advanced Materials* **2001**, *13* (8), 604–608.
- [98] Henry, M. D.; Walavalkar, S.; Homyk, A.; Scherer, A., Alumina etch masks for fabrication of high-aspect-ratio silicon micropillars and nanopillars. *Nanotechnology* **2009**, *20*, 255305.
- [99] Grigoras, K.; Sainiemi, L.; Tiilikainen, J.; Säynätjoki, A.; Airaksinen, V.-M.; Franssila, S., Application of ultra-thin aluminum oxide etch mask made by atomic layer deposition technique. *Journal of Physics: Conference Series* **2007**, *61*, 369–373.
- [100] Wu, B.; Kumar, A.; Pamarthy, S., High aspect ratio silicon etch: A review. *Journal of Applied Physics* **2010**, *108* (5), 51101.
- [101] Odom, T.; Huang, J.; Kim, P.; Lieber, C., Atomic structure and electronic properties of single-walled carbon nanotubes. *Nature* **1998**, *391*, 62–64.
- [102] Wildoer, J. W. G.; Venema, L. C.; Rinzler, A. G.; Smalley, R. E.; Dekker, C., Electronic structure of atomically resolved carbon nanotubes. *Nature* **1998**, *391* (6662), 59–62.

- [103] Hartschuh, A.; Pedrosa, H. N.; Peterson, J.; Huang, L.; Anger, P.; Qian, H.; Meixner, A. J.; Steiner, M.; Novotny, L.; Krauss, T. D., Single carbon nanotube optical spectroscopy. *Chemphyschem* **2005**, *6* (4), 577–82.
- [104] O’Connell, M. J.; Bachilo, S. M.; Huffman, C. B.; Rialon, K. L.; Boul, P. J.; Noon, W. H., Band Gap Fluorescence from Individual Single-Walled Carbon Nanotubes. *Science* **2002**, *297*, 593–597.
- [105] Green, A. A.; Hersam, M. C., Nearly single-chirality single-walled carbon nanotubes produced via orthogonal iterative density gradient ultracentrifugation. *Advanced materials* **2011**, *23* (19), 2185–90.
- [106] Boghossian, A. A.; Zhang, J.; Barone, P. W.; Reuel, N. F.; Kim, J.-H.; Heller, D. A.; Ahn, J.-H.; Hilmer, A. J.; Rwei, A.; Arkalgud, J. R.; Zhang, C. T.; Strano, M. S., Near-infrared fluorescent sensors based on single-walled carbon nanotubes for life sciences applications. *ChemSusChem* **2011**, *4* (7), 848–63.
- [107] Barone, P. W.; Baik, S.; Heller, D. a.; Strano, M. S., Near-infrared optical sensors based on single-walled carbon nanotubes. *Nature materials* **2005**, *4* (1), 86–92.
- [108] Karaiskaj, D.; Mascarenhas, A.; Choi, J.; Graff, R.; Strano, M., Temperature behavior of the photoluminescence decay of semiconducting carbon nanotubes: The effective lifetime. *Physical Review B* **2007**, *75* (11), 113409.
- [109] Wang, F.; Dukovic, G.; Brus, L.; Heinz, T., Time-Resolved Fluorescence of Carbon Nanotubes and Its Implication for Radiative Lifetimes. *Physical Review Letters* **2004**, *92* (17), 177401.
- [110] Hersam, M. C., Progress towards monodisperse single-walled carbon nanotubes. *Nature nanotechnology* **2008**, *3* (7), 387–94.
- [111] Arnold, M. S.; Stupp, S. I.; Hersam, M. C., Enrichment of single-walled carbon nanotubes by diameter in density gradients. *Nano letters* **2005**, *5* (4), 713–8.
- [112] Arnold, M. S.; Green, A. a.; Hulvat, J. F.; Stupp, S. I.; Hersam, M. C., Sorting carbon nanotubes by electronic structure using density differentiation. *Nature nanotechnology* **2006**, *1* (1), 60–5.
- [113] Spataru, C.; Ismail-Beigi, S.; Capaz, R.; Louie, S., Theory and Ab Initio Calculation of Radiative Lifetime of Excitons in Semiconducting Carbon Nanotubes. *Physical Review Letters* **2005**, *95* (24),

247402.

- [114] Johnson, P. B.; Christy, R. W., Optical Constants of the Noble Metals. *Physical Review B* **1972**, *6* (12), 4370–4379.
- [115] Xia, F.; Wang, H.; Xiao, D.; Dubey, M.; Ramasubramaniam, A., Two-dimensional material nanophotonics. *Nature Photonics* **2014**, *8*, 899.
- [116] Xia, F.; Wang, H.; Jia, Y., Rediscovering black phosphorus as an anisotropic layered material for optoelectronics and electronics. *Nature Communications* **2014**, *5*, 4458.
- [117] Ling, X.; Wang, H.; Huang, S.; Xia, F.; Dresselhaus, M. S., The renaissance of black phosphorus. *Proceedings of the National Academy of Sciences* **2015**, *112* (15), 4523–4530.
- [118] Kang, J.; Wells, S. A.; Wood, J. D.; Lee, J.-H.; Liu, X.; Ryder, C. R.; Zhu, J.; Guest, J. R.; Husko, C. A.; Hersam, M. C., Stable aqueous dispersions of optically and electronically active phosphorene. *Proceedings of the National Academy of Sciences* **2016**, *113* (42), 11688–11693.
- [119] Lotya, M.; Hernandez, Y.; King, P. J.; Smith, R. J.; Nicolosi, V.; Karlsson, L. S.; Blighe, F. M.; De, S.; Wang, Z.; McGovern, I. T.; Duesberg, G. S.; Coleman, J. N., Liquid Phase Production of Graphene by Exfoliation of Graphite in Surfactant/Water Solutions. *Journal of the American Chemical Society* **2009**, *131* (10), 3611–3620.
- [120] Ferry, V. E.; Smith, J. M.; Alivisatos, A. P., Symmetry Breaking in Tetrahedral Chiral Plasmonic Nanoparticle Assemblies. *ACS Photonics* **2014**, *1* (11), 1189–1196.
- [121] Wang, L.-Y.; Smith, K. W.; Dominguez-Medina, S.; Moody, N.; Olson, J. M.; Zhang, H.; Chang, W.-S.; Kotov, N.; Link, S., Circular Differential Scattering of Single Chiral Self-Assembled Gold Nanorod Dimers. *ACS Photonics* **2015**, *2* (11), 1602–1610.
- [122] Panaro, S.; Nazir, A.; Liberale, C.; Das, G.; Wang, H.; De Angelis, F.; Proietti Zaccaria, R.; Di Fabrizio, E.; Toma, A., Dark to Bright Mode Conversion on Dipolar Nanoantennas: A Symmetry-Breaking Approach. *ACS Photonics* **2014**, *1* (4), 310–314.
- [123] Campione, S.; Liu, S.; Basilio, L. I.; Warne, L. K.; Langston, W. L.; Luk, T. S.; Wendt, J. R.; Reno, J. L.; Keeler, G. A.; Brener, I.; Sinclair, M. B., Broken Symmetry Dielectric Resonators for High Quality Factor Fano Metasurfaces. *ACS Photonics* **2016**, *3* (12), 2362–2367.

- [124] Lubin, S. M.; Hryn, A. J.; Huntington, M. D.; Engel, C. J.; Odom, T. W., Quasiperiodic Moiré Plasmonic Crystals. *ACS Nano* **2013**, *7* (12), 11035–11042.
- [125] Vardeny, Z. V.; Nahata, A.; Agrawal, A., Optics of photonic quasicrystals. *Nature Photonics* **2013**, *7*, 177.
- [126] Ledermann, A.; Cademartiri, L.; Hermatschweiler, M.; Toninelli, C.; Ozin, G. A.; Wiersma, D. S.; Wegener, M.; von Freymann, G., Three-dimensional silicon inverse photonic quasicrystals for infrared wavelengths. *Nature Materials* **2006**, *5*, 942.
- [127] Chan, C. T., Quasicrystals enter third dimension. *Nature Photonics* **2007**, *1*, 91.
- [128] Zhou, W.; Gao, H.; Odom, T. W., Toward Broadband Plasmonics: Tuning Dispersion in Rhombic Plasmonic Crystals. *ACS Nano* **2010**, *4* (2), 1241–1247.
- [129] Zou, S.; Schatz, G. C., Theoretical studies of plasmon resonances in one-dimensional nanoparticle chains: narrow lineshapes with tunable widths. *Nanotechnology* **2006**, *17* (11), 2813.
- [130] Chu, Y.; Schonbrun, E.; Yang, T.; Crozier, K. B., Experimental observation of narrow surface plasmon resonances in gold nanoparticle arrays. *Applied Physics Letters* **2008**, *93* (18), 181108.
- [131] Lozano, G.; Grzela, G.; Verschuuren, M. A.; Ramezani, M.; Rivas, J. G., Tailor-made directional emission in nanoimprinted plasmonic-based light-emitting devices. *Nanoscale* **2014**, *6*, 9223–9229.
- [132] Zakharko, Y.; Graf, A.; Zaumseil, J., Plasmonic Crystals for Strong LightMatter Coupling in Carbon Nanotubes. *Nano Letters* **2016**, *16* (10), 6504–6510.
- [133] Tran, T. T.; Wang, D.; Xu, Z.-Q.; Yang, A.; Toth, M.; Odom, T. W.; Aharonovich, I., Deterministic Coupling of Quantum Emitters in 2D Materials to Plasmonic Nanocavity Arrays. *Nano Letters* **2017**, *17* (4), 2634–2639.
- [134] Hakala, T. K.; Rekola, H. T.; Väkeväinen, A. I.; Martikainen, J.-P.; Nečada, M.; Moilanen, A. J.; Törmä, P., Lasing in dark and bright modes of a finite-sized plasmonic lattice. *Nature Communications* **2017**, *8*, 13687.
- [135] Guo, R.; Hakala, T. K.; Törmä, P., Geometry dependence of surface lattice resonances in plasmonic nanoparticle arrays. *Physical Review B* **2017**, *95* (15), 155423.

APPENDIX A

Near-field Mapping

Lumerical has useful but limited capabilities for plotting near-field properties. This appendix provides suitable code for exporting the field monitor data from Lumerical into a Matlab data file and an additional script for making calculations and plots in Matlab. This is particularly useful for mapping the phase for modes that are not polarized along one of the major axes, as Lumerical has functionality for plotting only the x-phase, y-phase, or z-phase.

Listing A.1. Lumerical script for exporting electric field intensity and electric field phase from Lumerical monitors into a Matlab data file.

```

1 %Make the following character substitutions to convert this to a
   Lumerical script:
2 %Comments: percent signs % in Matlab and hashtags # in Lumerical
3 %Text Strings: single quotes ' in Matlab and double quotes " in
   Lumerical
4
5 i=62;          %Lattice Angle. Used only for tracking the file.
6
7 % get Field matrix data from the simulation
8 mname='field 0';      % Electric Field monitor name
9 x=getdata(mname,'x');    % position vectors associated with Ex
   fields
10 y=getdata(mname,'y');   % position vectors associated with Ex
   fields

```

```
11 Ex=getdata(mname, 'Ex');      % Ex fields at monitor
12 Ey=getdata(mname, 'Ey');      % Ey fields at monitor
13 Ez=getdata(mname, 'Ez');      % Ez fields at monitor
14 %T=transmission(mname);      % Power transmission through monitor
15
16 % save matrix variables x, y, E(x,y,z), and T to a data file
17
18 filename='Fields0'; % set filename.
19 matlabsave(filename, x,y,Ex,Ey,Ez,i);
20
21 % get Charge matrix data from the simulation
22 mname2='divergencecurrent';    % Charge monitor name
23 rhom=getresult(mname2, 'rho'); % position vectors associated
    with Charge Values
24 rho=rhom.rho;                 % Charge
25 rhox=rhom.x;                  % x values
26 rhox=rhom.y;                  % y values
27 rhoz=rhom.z;                  % z values
28
29 % save matrix variables for charge and position vectors to a data
    file
30
31 filename='charge'; % set filename.
32 matlabsave(filename, rhox,rhox,rhoz,rho,i);
```

Listing A.2. Matlab script for calculating and plotting electric field intensity and electric field phase using Lumerical output of field monitors, and charge density maps using Lumerical output of charge monitors.

```

1 % Instructions for use:
2 % 1) Open field files and charge files
3 % 2) Set mode polarization angle for phase
4 % 3) Rename figure titles according to lattice angle
5
6 %%
7 %Squeeze: eliminate singleton dimensions
8 %Ex
9 Ex1=squeeze(Ex(:,:, :, 2)); %Blue wavelength Ex
10 Ex2=squeeze(Ex(:,:, :, 1)); %Red wavelength Ex
11
12 Ex1Re=real(Ex1); %Real of Ex, Blue wavelength
13 Ex1Im=imag(Ex1); %Imaginary of Ex, Blue wavelength
14
15 Ex2Re=real(Ex2); %Real of Ex, Red wavelength
16 Ex2Im=imag(Ex2); %Imaginary of Ex, Red wavelength
17
18 %Ey
19 Ey1=squeeze(Ey(:,:, :, 2)); %Blue wavelength Ey
20 Ey2=squeeze(Ey(:,:, :, 1)); %Red wavelength Ey
21
22 Ey1Re=real(Ey1); %Real of Ey, Blue wavelength
23 Ey1Im=imag(Ey1); %Imaginary of Ey, Blue wavelength

```

```

24
25 Ey2Re=real(Ey2); %Real of Ey, Red wavelength
26 Ey2Im=imag(Ey2); %Imaginary of Ey, Red wavelength
27
28 %Ez
29 Ez1=squeeze(Ez(:,:, :, 2)); %Blue wavelength Ey
30 Ez2=squeeze(Ez(:,:, :, 1)); %Red wavelength Ey
31
32 Ez1Re=real(Ez1); %Real of Ey, Blue wavelength
33 Ez1Im=imag(Ez1); %Imaginary of Ey, Blue wavelength
34
35 Ez2Re=real(Ez2); %Real of Ey, Red wavelength
36 Ez2Im=imag(Ez2); %Imaginary of Ey, Red wavelength
37
38 %xyz
39 xs=10^9*squeeze(x);
40 ys=10^9*squeeze(y);
41
42 %%
43 %E^2 Calculations
44 %close all
45
46 %Blue Mode E^2
47 E1=Ex1.*conj(Ex1)+Ey1.*conj(Ey1)+Ez1.*conj(Ez1);
48 figure;
49 surf(xs, ys, E1, 'EdgeColor', 'None', 'facecolor', 'interp');

```

```
50 view(2);
51 colormap jet;
52 title('|E|^2 for \lambda_1');
53 xlabel('x (mm)');
54 ylabel('y (mm)');
55 colorbar
56 box on
57 grid off
58 fig=gcf;
59 fig.Color = [1 1 1];
60
61 %Red Mode E^2
62 E2=Ex2.*conj(Ex2)+Ey2.*conj(Ey2)+Ez2.*conj(Ez2);
63 figure;
64 surf(xs, ys, E2', 'EdgeColor', 'None', 'facecolor', 'interp');
65 view(2);
66 colormap jet;
67 title('|E|^2 for \lambda_2');
68 xlabel('x (mm)');
69 ylabel('y (mm)');
70 colorbar
71 box on
72 grid off
73 fig=gcf;
74 fig.Color = [1 1 1];
75
```

```
76 %%
77 %Phase Calculations
78
79 %Blue Mode
80 theta1=0 %For Blue Mode (1,1)->0
81 RealE1=cos(theta1)*Ex1Re+sin(theta1)*Ey1Re;
82 ImagE1=cos(theta1)*Ex1Im+sin(theta1)*Ey1Im;
83 phase1=atan(ImagE1./RealE1);
84 phase1(RealE1<0) = phase1(RealE1<0) + pi();
85 phase1(phase1> pi()) = phase1(phase1> pi()) - 2*pi();
86
87 %Phase Plot Blue
88 figure;
89 surf(xs, ys, phase1, 'EdgeColor', 'None');
90 view(2);
91 colormap hsv;
92 caxis([-3.14, 3.14])
93 title('Phase for \lambda-1');
94 xlabel('x (mm)');
95 ylabel('y (mm)');
96 colorbar
97 box on
98 grid off
99 fig=gcf;
100 fig.Color = [1 1 1];
101
```

```
102 %%
103 %Red Mode
104 theta2=(90-67/2)*pi/180; %For Red Mode (0,1)-> 90-Lattice Angle/2
105 RealE2=cos(theta2)*Ex2Re+sin(theta2)*Ey2Re;
106 ImagE2=cos(theta2)*Ex2Im+sin(theta2)*Ey2Im;
107 phase2=atan(ImagE2./RealE2);
108 phase2(RealE2<0) = phase2(RealE2<0) + pi();
109 phase2(phase2> pi()) = phase2(phase2> pi()) - 2*pi();
110
111
112 %Phase Plot Red
113 figure;
114 surf(xs, ys, phase2, 'EdgeColor', 'None');
115 view(2);
116 colormap hsv;
117 caxis([-3.14, 3.14])
118 title('Phase for \lambda_2');
119 xlabel('x (mm)');
120 ylabel('y (mm)');
121 colorbar
122 box on
123 grid off
124 fig=gcf;
125 fig.Color = [1 1 1];
126
127
```

```
128 %%
129 %Charge Calculations
130 close all
131
132 %Blue Charge
133 charge1=real(rho(:,:,10,2));
134 figure;
135 surf(rhox*10^9, rhoy*10^9, charge1','EdgeColor','None','
      facecolor','interp');
136 view(2);
137 colormap jet;
138 title('Charge for \lambda_1');
139 xlabel('x (mm)');
140 ylabel('y (mm)');
141 colorbar
142 box on
143 grid off
144 fig=gcf;
145 fig.Color = [1 1 1];
146
147 %Red Charge
148 charge2=real(rho(:,:,10,1));
149 figure;
150 surf(rhox*10^9, rhoy*10^9, charge2','EdgeColor','None','
      facecolor','interp');
151 view(2);
```

```
152 colormap jet;  
153 title('Charge for \lambda_2');  
154 xlabel('x (mm)');  
155 ylabel('y (mm)');  
156 colorbar  
157 box on  
158 grid off  
159 fig=(gcf);  
160 fig.Color = [1 1 1];
```

APPENDIX B

Vita

EDUCATION

-
- Northwestern University – McCormick School of Engineering: Evanston, IL* 2018
- PhD Candidate: Materials Science and Engineering
 - Thesis topic: Nanofabrication techniques for engineering photonic device responses
- Northwestern University – Kellogg School of Management: Evanston, IL* 2017
- Certificate: Management for Scientists and Engineers
 - Intensive course including intellectual property, marketing, strategy, and entrepreneurship
- Carleton College: Northfield, MN* 2011
- Bachelor of Arts: Physics and Mathematics
 - Honors: *Phi Beta Kappa, magna cum laude*, Dean's List 2009-2010 and 2007-2008

TECHNICAL SKILLS

-
- Fabrication:* Clean room operation, photolithography, nanopatterning, thin film coating, physical vapor deposition (evaporation and sputtering), atomic layer deposition (ALD), plasma processing (RIE), surface chemistry modification
- Characterization:* Optics and lasers, ellipsometry, UV-vis spectroscopy, fluorescence spectroscopy, scanning electron microscopy (SEM), atomic force microscopy (AFM)
- Design & Analysis:* MATLAB, Lumerical FDTD (optical device simulator), ImageJ, Mathematica, R, LaTeX, Microsoft Office, Adobe Illustrator, Blender (3D animator)

RESEARCH EXPERIENCE

-
- Graduate Research Assistantship: Northwestern University* 2012-Present
- Designed, constructed, and characterized optical devices to study tunable optical modes and lasing properties in nano-structured plasmonic cavities
 - Developed creative and scalable nanofabrication techniques to pattern cm-scale areas with feature periodicities down to 100 nm for ultraviolet photonic devices
 - Collaborated with interdisciplinary research groups at Argonne National Laboratory to fabricate and test laser devices (4 annual proposals selected)
 - Managed clean room facilities to support lithography capabilities and UV-vis spectroscopy equipment to assist with characterization of optical devices
 - Oversaw a 25-person lab as safety designate to promote a safe work environment
 - Learned new topics and techniques to solve problems independently
- Fulbright Fellowship: Norwegian University of Science and Technology* 2011-2012
- Created spatial mappings of chemical impurities and optoelectronic properties for silicon boules
 - Connected crystallization process with distribution of impurities affecting solar cell performance
- Student Airborne Research Program: NASA Earth Science Division* 2010
- Collected aerial remote sensing spectroscopic data aboard the DC-8 Airborne Science Laboratory from Armstrong Flight Research Center and on-site calibration data for orchards
 - Modeled evapo-transpiration mappings using remote sensing for informed irrigation

PUBLICATIONS

- **M.P. Knudson**, R. Li, W. Wang, R. Schaller, and T.W. Odom, "Polarization dependent lasing behavior in low-symmetry nanocavity arrays." [In Preparation]
- D. Wang, M.R. Bourgeois, W.K. Lee, R. Li, D. Trivedi, **M.P. Knudson**, W. Wang, G.C. Schatz, and T.W. Odom, "Stretchable plasmon nanolasers." [In Preparation]
- J. Hu, D. Wang, D. Bhowmik, **M.P. Knudson**, X. Ao, T. Liu, and T.W. Odom, "Reconfigurable plasmonic metasurfaces on strongly-coupled nanoparticle arrays." [In Preparation]
- D. Wang, W. Wang, **M.P. Knudson**, G.C. Schatz, and T.W. Odom, "Structural engineering in plasmonic nanolasers." *Chemical Reviews*. DOI: 10.1021/acs.chemrev.7b00424 [Accepted]
- **M.P. Knudson**, A.J. Hryn, M.D. Huntington, and T.W. Odom, "Sequential feature-density doubling for ultraviolet plasmonics." *ACS Applied Materials and Interfaces* 9, 33554-33558 (2017). **Awarded ACS Editors' Choice.**
- A. Yang, Z. Li, **M.P. Knudson**, A.J. Hryn, W. Wang, K. Aydin, and T.W. Odom, "Unidirectional lasing from template-stripped two-dimensional plasmonic crystals." *ACS Nano* 9, 11582-11588 (2015). **Awarded ACS Editors' Choice.**
- **M.P. Knudson**, M. Juel, E.J. Øvrelid, and M. Di Sabatino, "Effects of impurities in mono-crystalline silicon for solar cells." *TMS Annual Meeting*, 219-226 (2013).

FELLOWSHIPS

<i>National Defense Science and Engineering Graduate (NDSEG) Fellowship: US DoD</i>	2014-2017
<i>National Science Foundation (NSF) Graduate Fellowship – Honorable Mention: US NSF</i>	2014
<i>Hierarchical Materials Cluster Program Fellowship: Northwestern University</i>	2014
<i>Fulbright Fellowship – Trondheim, Norway: US-Norway Fulbright Foundation</i>	2011-2012

LEADERSHIP AND OUTREACH ACTIVITIES

<i>REU Program: Materials Research Center, Northwestern University</i>	2016 & 2017
<ul style="list-style-type: none"> • Mentored one undergraduate each summer to complete a 9-week original research project • Advised students on communicating their findings, including a conference poster at SACNAS 	
<i>Nano Scout Day: International Institute for Nanotechnology, Northwestern University</i>	2015 & 2016
<ul style="list-style-type: none"> • Organized micro-contacting printing demonstration for >60 local Boy Scouts and Girl Scouts 	
<i>Northwestern Triathlon Team: Northwestern Club Sports</i>	2014-2015
<ul style="list-style-type: none"> • Planned and led team travel to 10 races with average of 12 athletes as vice president • Won team championship for Mideast Collegiate Triathlon Conference Series 	
<i>Materials Science Student Association: Northwestern University</i>	2013-2014
<ul style="list-style-type: none"> • Facilitated quarterly faculty panels with >20 students each as Student-Faculty Representative • Identified relevant topics including working at national labs and careers in industry 	
<i>Science in the Classroom: Northwestern University</i>	2013-2014
<ul style="list-style-type: none"> • Taught monthly interactive science demonstrations for 3rd grade class at Hayt Elementary School 	